

國立交通大學

材料科學與工程學系

博士論文

探討奈米粒子對 PS-*b*-P4VP 雙塊式高分子之
影響與 PS-*b*-P4VP 雙塊式高分子薄膜應用於
記憶體元件

**The Effect of Sequestered Nanoparticles on the
Morphologies of Poly(styrene-*b*-4-vinylpyridine) and
a Poly(styrene-*b*-4-vinylpyridine) Thin Film Based
Memory Device**

研究生：黃清茂

指導教授：韋光華 博士

中華民國 九十七年十二月

探討奈米粒子對 PS-*b*-P4VP 雙塊式高分子之影響與
PS-*b*-P4VP 雙塊式高分子薄膜應用於記憶體元件
The Effect of Sequestered Nanoparticles on the Morphologies of
Poly(styrene-*b*-4-vinylpyridine) and a Poly(styrene-*b*-4-
vinylpyridine) Thin Film Based Memory Device

研究生：黃清茂

Student: Ching-Mao Huang

指導教授：韋光華 博士

Advisor: Dr. Kung-Hwa Wei

國立交通大學

材料科學與工程研究所

博士論文

A Thesis

Submitted to Department of Material Science and Engineering

College of Engineering

National Chiao-Tung University

in Partial Fulfillment of the Requirements

for the Degree of

Doctor of Engineering

in

Material Science and Engineering

December 2008

Hsinchu, Taiwan, Republic of China

中華民國 九十七 年 十二 月

Abstract

In this dissertation, we used in situ annealing small-angle X-ray scattering (SAXS) to monitor the structural evolution of a spherical poly(styrene-*b*-4-vinylpyridine) diblock copolymer (PS-*b*-P4VP)/2-phenylethanethiol-coated Au nanoparticle (NP) mixture in the solid state during its thermal annealing. We found that the Au NPs that existed initially in a random state with some cluster packing in the PS domain diffused to the interface of the amphiphilic PS-*b*-P4VP diblock copolymer within 4 h at 170 °C under vacuum to form NP-filled shell-like assemblies, as evidenced from transmission electron microscopy and anomalous SAXS. The Au NP nano-shell assemblies were stable even after redissolving in toluene.

Furthermore, we found that two kinds of NPs—hydrophilic pyridine-coated CdSe NPs and hydrophobic dodecanethiol-coated Au NPs—collectively self-assemble in the PS and P4VP blocks, respectively, of a lamellar PS-*b*-P4VP diblock copolymer to form a pseudo-tetragonal single-crystalline structure as evidenced from SAXS. The formation of a tetragonal-like single crystal results from micelle structures possessing strong hydrophilic P4VP/CdSe cores and hydrophobic PS/Au coronas that prevented the cores from forming the randomly oriented lamellar domains. Instead, the composite microphase separated into a long-range-ordered structure.

Finally, we reported the performance of a nonvolatile memory device based on a solution-processed PS-*b*-P4VP thin film. The Al/PS-*b*-P4VP/ITO memory device featuring metal-coordinated 30-nm-diameter P4VP cores exhibited an ON/OFF ratio of 2×10^5 , an erase voltage of 0.75 V, a write voltage of -0.5 V, and a retention time of 10^4 s. The device exhibited metallic behavior in the ON state, suggesting the formation of metallic filaments through the migration of Al atoms into the P4VP domain during writing. Such nanostructured diblock copolymer thin films open up new avenues for fabricating organic memory devices using simple procedures.

摘要

此論文主旨為利用小角度散射技術來偵測球狀 PS-*b*-P4VP 雙塊式共聚高分子/苯乙基硫醇-Au 奈米粒子複合材料於熱處理期間的結構演進。研究結果發現 Au 奈米粒子起初以具部分團簇隨機地分佈在 PS 相中，經過 170°C 真空下熱處理 4 小時後，由電子顯微鏡與 anomalous 小角度散射觀察得知，Au 遷移至 PS 與 P4VP 的界面，進而形成一層包覆在 P4VP 球外的 Au 殼排列。此結構更被證實是可以穩定的以 PS-Au-P4VP 微胞結構保存於甲苯中。

接著，本論文進一步探討分別將親水性的 CdSe 奈米粒子與疏水性的 Au 奈米粒子先後操控置入 P4VP 與 PS 相中。利用 2-D SAXS 鑑定發現在含有適當的 CdSe 與 Au 體積分率的 PS-*b*-P4VP/CdSe/Au 三元複合材料，會使原本為層狀結構之 PS-*b*-P4VP 轉變為擬四方體單晶結構。此一相轉變乃由於 CdSe 與 Au 奈米粒子分別置入 P4VP 與 PS 後造成內聚更強的 P4VP/CdSe 核與較鬆散的 PS/Au 殼，導致溶劑移除後 PS-*b*-P4VP/CdSe/Au 能以穩定的微包結構取代融合回層狀而存在於固相中，並以溶劑退火(solvent annealing)後堆疊成擬四方體單晶結構。

最後，本論文利用柱狀 PS-*b*-P4VP 雙塊式共聚高分子製備可靠的(reliable)有機非揮發性記憶體。Al/PS-*b*-P4VP/ITO 元件乃由溶液製程在 ITO 基材上旋轉塗佈 30 奈米厚且具六方堆積(hexagonal)奈米結構之 PS-*b*-P4VP 薄膜，並蒸鍍 Al 為上電極。此一新穎的有機非揮發性記憶體 on/off ratio 可以達到 2×10^5 ，寫入和抹除的時間可達到微秒(us)的狀態，且有超過 10^4 秒的資料保存時間(retention time)與推估可使用長達 10 年以上。根據 Al/PS-*b*-P4VP/ITO 元件於 On-state 下的變溫 I-V 曲線特性分析，元件之電流隨溫度下降而上升，代表導電行為似金屬特性。因此，判定所屬的記憶機制應為金屬導線(metallic filament)。利用此具奈米結構的雙塊式共聚高分子薄膜，經由簡單的溶液製程製備有機記憶體元件，將提供一條新的有機非揮發性記憶體製程途徑。

誌謝

感謝上天，感謝交大校門前的土地公，終於到可以寫誌謝的時候了。回首過去博班一千多個日子裡，往事歷歷在目。這一路走來，有笑、有淚，但更多時候卻是笑中含淚、淚中帶笑的。時至今日，雖然完成了這部論文，但人生的挑戰卻正要開始。此時此刻，僅以本篇表達我的誠摯謝意。

首先要先感謝的是指導教授韋光華老師提供舒適的研究環境，並且在溝通上猶如父親般的包容、在生活上配予優厚的薪水、在研究上給予適時叮嚀與指導。才讓我得以汲取到豐富歷練，對往後的人生更有信心。也感謝在論文研究過程中給予我極大幫助的鄭有舜博士，正是他讓我的所做出來的材料，在小角度散射的光芒下點石成金。另外，也感謝陳信龍教授、許鈺宗教授、何榮銘教授、陳貞夙教授百忙之中挪空擔任口試委員，並在口試期間提供許多寶貴的建議。這些師長的鼓勵，是我對研究繼續充滿著熱情的主要動力。

實驗室畢業的學長家充、帥帥、良祐、Mickey、小豬、孝蔚、中斌、老周，感謝你們讓我看到畢業後美好，讓我能夠持續朝著這個目標來邁進。還有實驗室的夥伴們：初為人父的振嘉學長、堅毅不拔卻為人親切的耀德、善於分析且為國道小霸王的旭生、認真負責的長跑健將茂源、老大不小仍體垂不減稚氣的冠宇、純真自然卻有公路殺手稱號的碩麟、認份執著又善良可愛的阿川、~~XXX~~很扁卻又~~壯~~子很凸的果子吟、好人一枚並努力不懈的阿閔、宅男代表會主席的明鑫、陽光男孩協會理事長的璨丞、~~台妹代表~~暱稱鞭炮串阿鬼的璽夷、寒冰掌高手的俠女秉萱、無聲無息碩二男雙的小藍與宗諭、熱心又負責忽寬忽細的助理克瑜、以及新進成員阿川二代—昌隆、建銘&柏宇賢伉儷、比我還捲的曜璿、小扁阿鬼傳人—慧妮&毓倩。正因為這群可愛又可惡的污水，讓我這股清流也跟著一起淪陷，時時刻刻快樂樂的聊八卦、討論news-paper。感謝這群夥伴，沒有你們的一路相陪，我也就沒辦法有機會生出這篇誌謝。

最後，僅以本論文獻給我最親愛的母親、父親、岳母、妻子芝佑、女兒靖芸以及十二位哥哥嫂嫂姊姊姐夫，感謝他們在我求學的期間給予精神上及生活上的協助與支持，使我無後顧之憂得以順利完成學業。

黃清茂 2008.12.12

Table of Contents

Abstract	I
摘要.....	II
誌謝.....	III
Chapter 1: Introduction	
1-1 Block Copolymers	1
1-2 Nanoparticles.....	13
1-3 Block Copolymer/Nanoparticle Mixtures.....	16
1-4 Organic Electrical Bistable Memory Device	24
1-5 Motivation and Scope of Dissertation	26
Chapter 2: Structural Evolution of Poly(styrene-<i>b</i>-4-vinylpyridine) Diblock Copolymer/Gold Nanoparticle Mixtures from Solution to Solid State	
2-1 Introduction.....	52
2-2 Methods and Analysis.....	53
2-3 Results and Discussions.....	56
2-4 Conclusions	65
Chapter 3: Pseudo-Single-Crystalline Self-Assembled Structure Formed from Hydrophilic CdSe and Hydrophobic Au Nanoparticles in the Poly(4-vinylpyridine) and Polystyrene Blocks, Respectively, of a Polystyrene-<i>b</i>-Poly(4-vinylpyridine) Diblock Copolymer	
3-1 Introduction	78
3-2 Methods and Analysis	79
3-3 Results and Discussions	83
3-4 Conclusions	88
Chapter 4: Electrical Bistable Memory Device Based on a Poly(styrene-<i>b</i>-4- vinylpyridine) Nanostructured Diblock Copolymer Thin Film	
4-1 Introduction	101
4-2 Methods and Analysis	102
4-3 Results and Discussions	103
4-4 Conclusions	105
Chapter 5: Conclusions	110

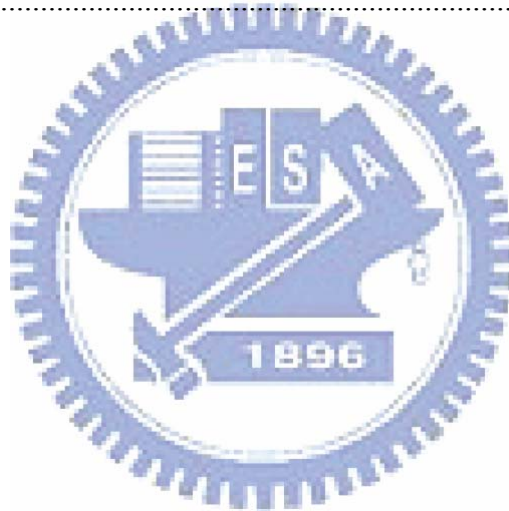
Chapter 6: Future Work.....112

References.....113

Appendix 1: Quantitative calculations of Au NPs at the surface of a single P4VP domain.....124

Appendix 2: Distance between the CdSe particles in a single P4VP domain
.....125

Publication List.....126



List of Figures

Chapter 1: Introduction

- Figure 1-1** Schematic phase diagram illustrating the various “classical” block copolymer morphologies adopted by linear diblock copolymers28
- Figure 1-2** Schematic representation of the morphologies of linear ABC triblock copolymers. The combination of the block sequence (ABC, ACB, BAC), composition, and block molecular weights provides an enormous parameter space for the creation of new morphologies29
- Figure 1-3** Well-established structures of block copolymers in the melt, solution, or solid state30
- Figure 1-4** Phase diagram of a self-assembled diblock copolymer. S: spherical; C: cylindrical; G: gyroidal; L: lamellar; S_{cp}: closed-packed spherical structure31
- Figure 1-5** Possible configurations of lamellae in block copolymer films. (a) Confined at one surface. (b) Confined at both surfaces.....32
- Figure 1-6** Thin film morphology of an asymmetric block copolymer that forms hexagonal morphologies in the bulk.....33
- Figure 1-7** Schematic representation of various applications of block copolymers in nanotechnology.....34
- Figure 1-8** Schematic representation of the production process of a metal nanodot array using block copolymer lithography35
- Figure 1-9** SEM image of a polystyrene-*b*-polyferrocenyldimethylsilane mask after removal of the polystyrene through O₂ RIE36
- Figure 1-10** Schematic representation of selectively distributed TiO₂ NPs in a PS-*b*-PMMA diblock copolymer37
- Figure 1-11** (a) Assembly of Au NPs (core: 3.9 ± 1.0 nm; shell: PS; core + shell = 7.7 nm) into PS-*b*-P4VP. (b) Assembly of Au NPs (core: 3.9 ± 1.0 nm; shell: PS and P2VP; core + shell = 7.7 nm) into PS-*b*-P4VP. (c, d) Respective

histograms of particle locations for the samples displayed in (a) and (b)	38
Figure 1-12 (a) Schematic of synthesis of needle-like TiO ₂ nanostructures with ordered patterns. (b) The cross-section SEM image of needle-like TiO ₂	39
Figure 1-13 SEM image of an etched polystyrene- <i>b</i> -polyisoprene diblock, revealing a fracture surface. The polystyrene network channels remaining after removal of polyisoprene are clearly visible.....	40
Figure 1-14 Density functional theory calculations of large (case 1) and small NPs (case 2). The NPs are either located at the center of the A phase (case 1) or driven closer to the A–B interface (case 2).....	41
Figure 1-15 Cross-sectional transmission electron micrograph displaying Au NPs patterned within the P4VP lamellae formed by a PS- <i>b</i> -P4VP diblock copolymer	42
Figure 1-16 TEM image of an array of Fe ₂ O ₃ NPs and 1-dodecanethiol-coated Au NPs in a PS- <i>b</i> -P4VP matrix after removal of the polymer matrix through O ₂ plasma treatment. The inset displays an enlarged view of Au NPs at the PS–PVP interface; the iron oxide NPs are centered in the former PVP phase	43
Figure 1-17 (a) NPs (CdSe–TOPO; R = 5 nm) deposited into a block copolymer template [PS–PMMA (70:30)] through withdrawal of the template from solution. (b) TEM image of the resulting film; the NPs are located inside the (black) holes.....	44
Figure 1-18 Deposition of Au NPs (R = 2.5 nm) via directed hydrogen bonding interactions onto a film consisting of a block copolymer	45
Figure 1-19 Morphological transformation from a hexagonally packed cylinder structure of pure PS- <i>b</i> -P4VP diblock copolymers to lamellar (CdS/P4VP)- <i>b</i> -PS composites	46
Figure 1-20 TEM micrograph of a ternary blend of PS- <i>b</i> -PEP, AuR ₁ , and SiO ₂ R ₂	

with an inorganic filling fraction (f) of 0:02, recorded after micro-sectioning normal to the layer direction (no stain).....47

Figure 1-21 (a) TEM image of a PS-PEP/AuSC₁₂H₂₅ composite after micro-sectioning normal to the layer direction, revealing particle deposition at the PS-PEP interface and (b) TEM image of a PS-PEP/AuSPS composite. PEP domains appear as brighter regions in the micrograph. (c) Absorbance spectra of PS-PEP/Au composite materials possessing an interfacial segregated morphology (dotted line) and a selective-layer uniform morphology (continuous line). Inset: Absorbance spectra of dilute nanocrystal solutions [AuSC₁₂H₂₅ (dotted line) and AuSPS (continuous line)].....48

Figure 1-22 Scaling behavior of the $I-V$ curves of 48% (Au NPs/P4VP)-*b*-PS and Au NPs/homo-P4VP at 78 K.....49

Figure 1-23 (a) Molecular structure of the PS-*b*-P4VP copolymer and a schematic representation of the micellation process with in situ synthesis of Au NPs in PS-*b*-P4VP. (b) AFM topographic image of the surface of a spin-coated PS-*b*-P4VP film along with a schematic illustration of a self-assembled PS-*b*-P4VP (with Au NPs) micellar film on a substrate. (c) Capacitance-voltage ($C-V$) measurements at 100 kHz on a metal-insulator-silicon structure with a PS-*b*-(P4VP/Au) film.....50

Figure 1-24 Typical $I-V$ curves for PVK films. The inset presents the plot of ON- and OFF-state resistances after reading at 1 V per 100 s. The retention time of the ON and OFF states is more than a time period of 105 s for the PVK films51

Chapter 2: Structural Evolution of Poly(styrene-*b*-4-vinylpyridine) Diblock Copolymer/Gold Nanoparticle Mixtures from Solution to Solid State Basic Electron Transport Theory

Figure 2-1 (a) HR-TEM image of AuSC₂Ph cast from a toluene solution. (b) The SAXS profile measured for the 0.5 wt % AuSC₂Ph NPs in toluene is fitted

(dashed curve) using polydisperse spheres of the Schultz distribution (in radius r) shown.	68
Figure 2-2 Solution SAXS profiles of the as-prepared PS- <i>b</i> -P4VP _{Sph} , AuSC ₂ Ph, and the PS- <i>b</i> -P4VP _{Sph} /AuSC ₂ Ph mixture in toluene	69
Figure 2-3 (a) In situ thermal annealing SAXS profiles of the as-prepared PS- <i>b</i> -P4VP _{Sph} /AuSC ₂ Ph mixture. (b) The SAXS profile of the annealed PS- <i>b</i> -P4VP _{Sph}	70
Figure 2-4 (a) Anomalous SAXS data for the PS- <i>b</i> -P4VP _{Sph} /AuSC ₂ Ph film before the thermal annealing, and (b) Anomalous SAXS data for the thermal annealed PS- <i>b</i> -P4VP _{Sph} /AuSC ₂ Ph film at two beam energies of 11.910 and 11.200 keV (near L ₃ -edge absorption of Au).....	71
Figure 2-5 (a) TEM image for the as-prepared PS- <i>b</i> -P4VP _{Sph} /AuSC ₂ Ph mixture, with abundant NP clusters. (b) TEM micrograph of the PS- <i>b</i> -P4VP _{Sph} /AuSC ₂ Ph mixture that had been subjected to two-step annealing, 48 h of solvent annealing at 30 °C and 72 h for thermal annealing at 170 °C. Inset: HR-TEM image of a single P4VP _{Sph} /AuSC ₂ Ph core/shell assembly.....	72
Figure 2-6 (a) The TGA result of the PS- <i>b</i> -P4VP _{Sph} /AuSC ₂ Ph mixture before and after 72 h thermal annealing at 170 °C under vacuum. (b) The weight loss (%) vs. the annealing time of the PS- <i>b</i> -P4VP _{Sph} /AuSC ₂ Ph mixture during the 170 °C isothermal annealing under a N ₂ atmosphere.	73
Figure 2-7 (a) Solution state SAXS profiles of the PS- <i>b</i> -P4VP _{Sph} , PS- <i>b</i> -P4VP _{Sph} /AuPy, and PS- <i>b</i> -P4VP _{Sph} /AuSC ₂ Ph systems after they had been subjected to annealing and redissolving in toluene. All schematic micellar structures of PS- <i>b</i> -P4VP _{Sph} -Au NP mixtures appear near the corresponding curves. (b) Three corresponding profiles fitted using the Guinier approximation....	74
Figure 2-8 (a) TEM image of a recast thin film of the PS- <i>b</i> -P4VP _{Sph} /AuSC ₂ Ph mixture that had been subjected to annealing. (b) HR-TEM image of a single P4VP _{Sph} /AuSC ₂ Ph core/shell assembly.....	75
Figure 2-9 Survey scanning XPS spectra of the pure P4VP (a), the annealed	

P4VP/AuSC₂Ph composites (b), the annealed lamellar PS-*b*-P4VP/AuSC₂Ph composites (c),^a and the as-prepared AuSC₂Ph NPs (d).....76

Figure 2-10 N 1s XPS spectra of the pure P4VP (a), the annealed P4VP/AuSC₂Ph composites (b), and the annealed lamellar PS-*b*-P4VP/AuSC₂Ph composites (c).....77

Chapter 3: Pseudo-Single-Crystalline Self-Assembled Structure Formed from Hydrophilic CdSe and Hydrophobic Au Nanoparticles in the Poly(4-vinylpyridine) and Polystyrene Blocks, Respectively, of a Poly(styrene-*b*-4-vinylpyridine) Diblock Copolymer

Figure 3-1 (a) SAXS profiles of PS-*b*-P4VP, PS-*b*-P4VP/CdSe NPs (3.3 vol%), and PS-*b*-P4VP/Au NPs (5.3 vol%). (b-d) Cartoon representations of the structures of the PS-*b*-P4VP/NP binary composites representing the SAXS profiles in (a).....93

Figure 3-2 TEM images of the (a) PS-*b*-P4VP/3.3 vol% CdSe NPs and (b) PS-*b*-P4VP/5.3 vol% Au NPs binary composites. The insets to (a) and (b) display enlarged partial images.....94

Figure 3-3 2D SAXS patterns in the low-*Q* range ($q = 0.06 - 0.2 \text{ nm}^{-1}$) for PS-*b*-P4VP/CdSe/Au ternary composites possessing various NP loadings. The contrast for each pattern is independent.95

Figure 3-4 2D SAXS patterns in low-*Q* range ($q = 0.06 - 0.2 \text{ nm}^{-1}$) for the PS-*b*-P4VP/CdSe/Au composite containing 1.7 vol% CdSe NPs and 5.3 vol% Au NPs. (a, b) The Miller indices are marked according to a tetragonal cell, used to index the diffraction patterns of the *ab* plane (white), superimposed over the tilted *ac* (orange) and *bc* (red) planes. (c) TEM images of PS-*b*-P4VP/1.7 vol% CdSe NPs/5.3 vol% Au NPs ternary composites revealing the [110] and [001] cell directions of the tetragonal cell. The upper-right-hand inset displays an enlarged image. (d) Corresponding orientation for the TEM images.96

Figure 3-5 (a) TEM image of the PS-*b*-P4VP/1.7 vol% CdSe NP/5.3 vol% Au NP composite. The inset displays the FFT of (a). (b) Reconstructed image (inverse FFT image) from the FFT image taken by the two pairs of FFT spots highlighted in the inset. (c, d) Reconstructed images taken by the single pairs of FFT spots highlighted in the respective insets.97

Figure 3-6 (a) TEM image of the PS-*b*-P4VP/1.7 vol% CdSe NP/5.3 vol% Au NP composite. EDX spectra recorded from the (b) PS/Au and (c) P4VP/CdSe phases marked by red dashed circles in the enlarged TEM image98

Figure 3-7 (a) Azimuthal scanning profile of the image in Figure 3-4b ($Q = 0.161 \text{ nm}^{-1}$); the (100), (0-1-1), (-101), (-10-1), (0-1-1), (-100), (01-1), (01-1), (10-1), (101), and (011) reflections are found at values of θ of 0° , 36° , 65° , 113° , 143° , 180° , 216° , 244° , 293° , and 323° , respectively. (b) SAXS profile obtained along the (101) spot in Figure 3-4b99

Figure 3-8 SAXS data for a control experiment employing PS-*b*-P4VP/CdSe/Au composites in solution. The PS-*b*-P4VP/NP composites incorporating 1.7 vol% CdSe NPs and/or 5.3 vol% Au NPs100

Chapter 4: Electrical Bistable Memory Device Based on a Poly(styrene-*b*-4-vinylpyridine) Nanostructured Diblock Copolymer Thin Film

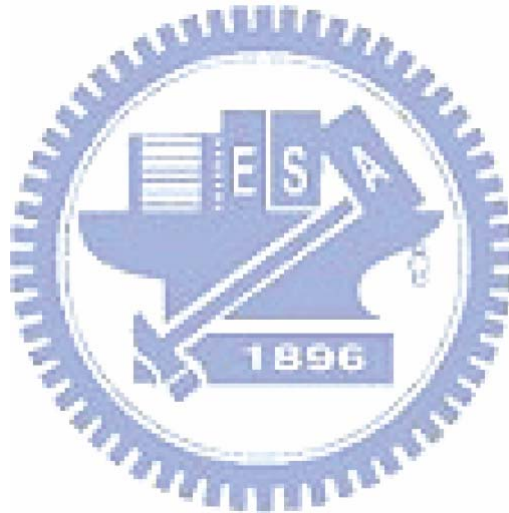
Figure 4-1 (a) Morphology of a cylindrical PS-*b*-P4VP diblock copolymer in the bulk state. (b) Micellar structure of a cylindrical PS-*b*-P4VP diblock copolymer in a selective solvent. (c) Nonvolatile memory device comprising an active PS-*b*-P4VP diblock copolymer film and Al and ITO electrodes. (d) SEM image of the cross-section of the memory device in (c).106

Figure 4-2 $I-V$ characteristics of PS (\blacklozenge), P4VP (\blacksquare), and PS-*b*-P4VP (\blacktriangle). The turn-on compliance current was restricted to 10^{-3} A. The inset displays an AFM topographic image of the PS-*b*-P4VP thin film prior to evaporating the Al electrode.107

Figure 4-3 Logarithmic $I-V$ plots measured at various temperatures for the ON state

at potentials ranging from 0.01 to 0.2 V. The inset displays the resistance of the ON state plotted with respect to the temperature.....108

Figure 4-4 (a) Write/read/erase test of the ITO/PS-*b*-P4VP/Al organic memory device. The bottom and top curves represent the applied voltage pulse and the corresponding current response, respectively. (b) Retention times of the ON and OFF states of the ITO/PS-*b*-P4VP/Al organic memory device probed in terms of the device current after stressing109



List of Schemes & Tables

Chapter 2: Structural Evolution of Poly(styrene-*b*-4-vinylpyridine) Diblock Copolymer/Gold Nanoparticle Mixtures from Solution to Solid State Basic Electron Transport Theory

Scheme 2-1 Fabrication of the Self-Assembled PS-*b*-P4VP/AuSC₂Ph Bulk Film 66

Scheme 2-2 Schematic Representation of the Structural Evolution of the PS-*b*-P4VP_{Sph}/ AuSC₂Ph Mixture at Various Annealing Times. 67

Chapter 3: Pseudo-Single-Crystalline Self-Assembled Structure Formed from Hydrophilic CdSe and Hydrophobic Au Nanoparticles in the Polystyrene and Poly(4-vinylpyridine) Blocks, Respectively, of a Poly(styrene-*b*-4-vinylpyridine) Diblock Copolymer

Scheme 3-1 Schematic Representation of the Method of Preparation of the PS-*b*-P4VP/ CdSe/Au Ternary Composites.....90

Scheme 3-2 Formation of Tetragonal Crystals from PS-*b*-P4VP/CdSe/Au Ternary Composites.....91

Table 3-1 Average center-to-center (*D*) and edge-to-edge (*d*) interparticle distances. The schematic representation of the cubic lattice model for the free volume per CdSe dot in a single P4VP domain92

Chapter 1

Introduction

1-1 Block Copolymers

Block copolymers are polymers composed of blocks of two or more different homopolymers joined together by covalent bonds in a variety of architectures. The most important characteristics for defining block copolymers are the

(1) weight- (M_w) and number-average (M_n) molecular weights of the block copolymer and its block components;

(2) *polydispersity index* (PDI), namely the molar mass distribution represented by M_w/M_n ;

(3) *volume fractions of blocks* (f), which characterizes the block copolymer composition; and

(4) *Flory–Huggins interaction parameter* (χ),^[1–3] a measure of the strength of interaction between the blocks.

Block copolymers are versatile platform materials because, at suitable compositions and under appropriate conditions, they can self-assemble into a variety of nanostructures, having period thicknesses between 10 and 100 nm, as a result of microphase separation between incompatible blocks. Block copolymer microphase separation can be described accurately in terms of two competing processes: *repulsion of dissimilar monomers* and *stretching of polymer chains*.^[4] Incompatibility of blocks drives them to separate into a microdomain structure where the block junctions form microdomain interfaces. Thermodynamically, this process is parameterized by the enthalpy of demixing of polymer blocks (ΔH_p). The surface-to-volume ratio—and, thus, the interfacial free energy—of the block copolymer system decreases as the microdomains increase in size. Because microdomain growth creates a density deficiency toward the microdomain's center, the block copolymer

chains are stretched beyond the undisturbed Gaussian gyration radius (R_g) to fill the space. This process, which is accompanied by a reduction of the configurational entropy ($\Delta S_{p,\text{conf}}$), opposes the block separation. The additional loss in entropy $\Delta S_{p,\text{int}}$ arises from confining the block junctions in the interfacial region. The sign of the change in Gibbs free energy (Eq. 1-1):

$$\Delta G_p = \Delta H_p - \Delta S_{p,\text{int}}T - \Delta S_{p,\text{conf}}T \quad (1-1)$$

indicates whether the transition from a phase possessing homogeneously mixed blocks (disordered state) to an ordered structure is favorable. The transition occurs when the enthalpic part dominates, i.e., $\Delta G_p > 0$. The demixing enthalpy (ΔH_p) is proportional to the dimensionless Flory–Huggins segmental interaction parameter χ , which exhibits the following temperature dependence (Eq. 1-2):

$$\chi = a/T + b \quad (1-2)$$

where a and b are experimentally obtained constants for a given composition of a particular blend pair. Experimentally, χ can be controlled through changes in temperature. The entropy penalty ΔS_p is inversely proportional to the total degree of polymerization (N), defined (for A-B diblock copolymers) as Eq. 1-3:

$$N = N_A + N_B \quad (1-3)$$

where N_A and N_B are the average number of monomeric units in blocks A and B, respectively. Unlike macrophase separation in blends, the connectivity of the blocks in block copolymers prevents complete separation; instead, the diblock copolymer chains organize to place the A and B portions on opposite sides of an interface. The equilibrium nanodomain structure must minimize unfavorable A–B contact without over-stretching the blocks.^[1] The product χN expresses the enthalpic/entropic balance—in other words, the degree of microphase separation. The values of χN and the block volume fraction f completely determine the symmetry and dimensions of the microphase-separated structure; they are used for to construct the block copolymer's

phase diagram. For the simplest class of A-B diblock copolymers, the following structures are known to be stable, as confirmed theoretically^[5] and experimentally^[2,6]: lamellar, hexagonal-packed cylinder, body-centered cubic, close-packed spherical (which may exhibit only liquid-like ordering), and bicontinuous cubic gyroid structures (Figure 1-1). For ABC triblocks, the combination of two independent composition variables (e.g., the volume fractions f_A , f_B and f_C , where $f_A + f_B + f_C = 1$) and three χ parameters (χ_{AB} , χ_{AC} , and χ_{BC}) leads to the much wider range of possible morphologies presented in Figure 1-2, many of which have been observed, although others await discovery.^[7] Theoretical studies have provided guidelines for rationalizing the observed morphologies; in future, they might also be used to predict structures.^[8]

1-1-1 Structures of Block Copolymer Melts, Solids, Solutions, and Thin Films

A remarkable property of block copolymers is their ability to self-assemble in the melt into a variety of ordered structures exhibiting nanoscale periodicities. These structures can be controlled by varying the composition of the block copolymer or the segregation between blocks (via the temperature or the degree of polymerization). Figure 1-3 displays the well-established structures of block copolymers in the melt, solution, and solid states.^[9]

1-1-2-1 Block Copolymer Melts

Interest in the phase behavior of block copolymer melts stems from the microphase separation of their blocks, leading to nanoscale-ordered morphologies. Two competing effects govern the thermodynamics of block copolymer melts. At high temperatures, the chains are mixed homogeneously, as in any polymer melt. As the temperature is reduced, the tendency for the blocks to segregate is enhanced, i.e.,

the enthalpic process of demixing is favored. This process is, however, necessarily accompanied by a reduction in entropy as the chain configuration becomes more constrained. The extent of segregation of the copolymer may then be expressed using the reduced parameter χN . Here N is the copolymer degree of polymerization, reflecting the N -dependent translational and configuration entropy.

The segment–segment interaction parameter (Flory–Huggins) describes the free energy cost per monomer of contacts between the A and B monomeric units; it is given by (Eq. 1-4):

$$\chi_{AB} = \left(\frac{Z}{\kappa_B T} \right) [\varepsilon_{AB} - (\varepsilon_{AA} + \varepsilon_{BB}) / 2] \quad (1-4)$$

where ε_{AB} is the interaction energy per monomer unit between the A and B monomers and Z is the number of nearest neighbor monomers to a copolymer configuration cell. Thus, a positive value of χ_{AB} (which occurs in the vast majority of cases) represents repulsion between the A and B monomers, whereas a negative value signifies mixing of unlike monomers. Moreover, the value of χ_{AB} usually varies inversely with the temperature. The second parameter that strongly influences the block copolymer behavior is the total degree of polymerization, N . For a large value of N , the loss of translational and configurational entropy leads to a reduction of the A-B monomer contacts and, thus, to local ordering. Because the entropic and enthalpic contributions to the free energy scale with respect to N^{-1} and χ , respectively, the value of the product χN is the most important factor when determining the block copolymer's phase state.

Figure 1-4 displays a good phase diagram computed using self-consistent mean field theory.^[10,11] It reveals the generic sequence of phases accessed just below the order–disorder transition temperature for diblock copolymers of various compositions. The features of the phase diagrams for particular systems differ in detail, but

qualitatively they are similar and are well accounted for by self-consistent field (SCF) theory.

1-1-2-2 Block Copolymer Solids

The structures of block copolymer melts are usually trapped upon vitrification. The mechanism underlying the glass transition is similar to those of the constituent homopolymers. Thus, there are few distinct physical factors associated with the formation of solid phases from glassy block copolymers.

In contrast, crystallization of one or both components of a block copolymer is accompanied by profound structural and dynamic changes. The fundamental process in crystallization of chains in a crystallizable block copolymer is the change in block conformation, i.e., the adoption of an extended or folded structure rather than the coiled configuration found in the melt or in solution. Crystallization from the melt often leads to a distinct (usually lamellar) structure having periodicity differing from that in the melt. Crystallization from solution can lead to non-lamellar crystalline structures, although they often possess trapped non-equilibrium morphologies. In addition to the formation of extended or folded chains, crystallization may also lead to gross orientational changes in the structures of the chains.

1-1-2-3 Block Copolymer Solutions

In a solvent, block copolymer phase behavior is controlled by the interaction between the segments of the polymers and the solvent molecules, as well as the interactions between the segments of the two blocks.^[12] If the solvent is unfavorable for one block, micelle formation can occur in dilute solution. The phase behavior of concentrated solutions can be mapped onto that of the block copolymer melts (Figure 1-3).^[9] There are two basic processes that characterize the phase behavior of block copolymers in solution: micellization and gelation. Micellization occurs when block

copolymer chains associate into (often spherical) micelles in dilute solution in a selective solvent. The core of the micelle is formed by the insoluble or poorly solvated block, whilst the corona contains the selectively solvated block. At a fixed temperature, micellization occurs upon increasing concentration to the critical micelle concentration (CMC). The CMC is usually determined from the sharp decrease in the surface tension as a function of concentration, although other properties, such as viscosity, also exhibit pronounced changes.

In concentrated solutions, micelles can become ordered into gels. Soft and hard gels are distinguished from each other and from micellar solutions by their flow properties—with gels being characterized by a finite yield stress. Hard gels seem to be associated with the formation of cubic phases of spherical micelles, whereas soft gels are usually lamellar or hexagonally packed rod micellar phases. The phase behavior of these materials has only recently begun to be elucidated using small angle scattering. It promises to be even richer than that of block copolymer melts—at least if results for analogous conventional surfactants are any guide. The flow behavior of these gels forms the basis for many of their applications; studies of the rheology and behavior of these materials under shear will enhance the fundamental understanding underpinning future developments.

1-1-2-4 Block Copolymer Thin Films

Microphase separation by block copolymers in thin films has been investigated from several perspectives. First, the physics of self-assembly in confined soft materials can be studied using model block copolymer materials for which reliable mean-field statistical mechanical theories have been developed.^[13–16] Second, interest has expanded as a result of the potentially exciting applications that exploit self-organization to (i) fabricate high-density data storage media,^[17,18] (ii) lithographically pattern semiconductors exhibiting ultra-small feature sizes,^[19,20] and

(iii) prepare ultra-fine filters or membranes.^[21] Although research in this field is growing at a rapid pace, the field has not been reviewed since 1998,^[2,22] even though many new developments have occurred.

Block copolymer films can be prepared using spin-coating techniques, where drops of a solution of the polymer in a volatile organic solvent are deposited on a spinning solid substrate (silicon wafers are often used because of their uniform flatness). The polymer film spreads as a result of centrifugal forces and the volatile solvent is rapidly driven off. With care, the method can provide films exhibiting low surface roughnesses over areas of several square millimeters. The film thickness can be controlled through modification of the spin speed, the concentration of the block copolymer solution, and the volatility of the solvent, which also influences the surface roughness.^[23] Dip coating is another reliable method for fabricating uniform thin films.^[24] Whichever deposition technique is used, if the surface energy of the block copolymer is much greater than that of the substrate, dewetting will occur. The mechanism of dewetting has been investigated in some depth.^[25-27]

In thin films, the lamellae formed by symmetric block copolymers can be oriented either parallel or perpendicular to the substrate. A number of possible arrangements of the lamellae are possible (Figure 1-5), depending on the surface energies of the blocks and the substrate and whether the film is confined at one or both surfaces. In the case that a different block preferentially wets the interface with the substrate or air, wetting is asymmetric and a uniform film has a thickness $(n + 1/2)d$. If the initial film thickness is not equal to $(n + 1/2)d$, then islands or holes (quantized steps of height d) form to conserve volume.^[28] As well as leading to distinct orientations, confinement of block copolymers can change the thermodynamics of ordering; in particular, surface-induced ordering persists above the bulk order-disorder transition.^[29]

Asymmetric block copolymers that form hexagonal or cubic-packed spherical morphologies in the bulk, form stripe or circular domain patterns in two dimensions, as illustrated in Figure 1-6. The stripe pattern results from cylinders lying parallel to the substrate; a circular domain surface pattern occurs when cylinders are oriented perpendicular to the substrate or when spheres are present at the surface. Because bicontinuous structures cannot exist in two dimensions, the gyroid phase is suppressed in thin films. Nanostructures in block copolymer films can be oriented using electric fields (if the difference in dielectric permittivity is sufficient)—an important property for applications in which parallel stripes^[30] or perpendicular cylinder configurations^[31] are desired.

1-1-3 Applications

Until recently, most block copolymers have been applied industrially as adhesives or for their mechanical properties (e.g., as thermoplastic elastomers). Only in the past 10 years have researchers taken block copolymers into the area of “high technology,” particularly into the realm of the so-called “nanotechnologies”. Many attempts have been made to use block copolymers in nanotechnology. Self-assembled block copolymer microstructures having dimensions ranging from 10 to 100 nm are useful as nanometer-scale membranes, templates for the fabrication of nano-objects (e.g., metal or ceramic nanodots and wires), as 1-, 2-, and 3D photonic crystals, and as nanopattern masks for the fabrication of high density information storage media. The majority of applications proposed to date rely on the use of thin film structures; this feature is a major focus of the current review, although bulk nanoporous materials and photonic crystals are also considered. Figure 1-7 summarizes the applications of various block copolymer-enabled nanotechnologies.^[32]

1-1-3-1 Nanolithography with Self-Assembled Block Copolymer Patterns

Although photolithography has played a dominant role in producing feature sizes smaller than 100 nm, feature sizes of less than 50 nm are not readily obtained using conventional lithography techniques. The minimum size that can be achieved through photolithography is determined by the wavelength of light used in the exposure. Electron beam lithography is commonly used to access feature sizes between 30 and 150 nm. Nevertheless, sizes less than 30 nm are not easy to obtain using standard lithography. One way to overcome this problem is through the use of self-assembled block copolymers.

In a pioneering paper, Park et al. demonstrated the use of block copolymer films as masks to transfer dotted and striped patterns into semiconductors.^[33] They achieved a feature density of holes of ca. 10^{11} cm^{-2} . The method they developed relies on the selective ozonation of polyisoprene (PI) or polybutadiene (PB) in block copolymers with polystyrene (PS) as the other (majority) component. Ozone cleaves the olefinic bonds in unsaturated polymers, such that they can be etched away. This process leaves holes or stripes in the PS matrix. This pattern is then transferred from the block copolymer into silicon nitride through reactive ion etching (RIE) using CF_4 or CF_4/O_2 gases. The quality of the pattern transfer is excellent, producing nanoscale arrays of pits or channels. Park et al. also described how to prepare nanoscale arrays of posts by using an “inverse” mask, relative to that employed to produce the array of pits. If the PI is fixed by staining with osmium tetroxide, then etching of the matrix will occur preferentially. The regions under the PI domains will be left as an array of posts. Details of the ozone etching method for preparing block copolymer film masks were elaborated on in a subsequent paper,^[21] which also contains data illustrating pattern transfer into other semiconductors, including silicon and germanium. A patent was awarded for this technology in 1999.^[34] In a further

extension of the technique, arrays of nano-sized metal posts have been fabricated using the modified method illustrated in Figure 1-8.^[35] A lithographic procedure in which the ozone etching step can be omitted has also been developed;^[36] here, the reactive ion etch rate is sufficiently different between the two blocks in the PS-*b*-PFS (PFS = polyferrocenyldimethylsilane) diblock copolymer, allowing selective etching of PS to occur directly. The technology has been applied to the development of a self-assembly route to produce a high-density magnetic storage medium (in this case, cobalt nanodots). Oxygen plasma RIE leaves PFS spheres; the pattern is then transferred into silicon oxide (which improves pattern transfer) and then into tungsten through RIE. The multiplayer structure is necessary because magnetic materials, such as cobalt, nickel, and iron, are not amenable to RIE. In the next step, the polymer and silica are removed. Finally, the pattern is transferred from the tungsten hard mask into the magnetic cobalt layer using ion-beam etching. The result is the array of cobalt nanospots illustrated in Figure 1-9.^[36] Ultrahigh-density metal nano-column arrays can be fabricated using block copolymer templates.

1-1-3-2 Nanoparticle Templates

Block copolymers have been utilized not only as surfactants to inhibit coalescence and aid in the dispersion of nanoscale particles (e.g., metals, metal oxides, inorganic nanostructures, molecular chromophores, and quantum dots) but also to spatially pattern them. Our group has previously reported^[37] the formation (Figure 1-10) of ordered clusters of surfactant-modified TiO₂ nanoparticles (NPs) in the selective block of lamellar assemblies of the diblock copolymer poly(styrene-*b*-methyl methacrylate) (PS-*b*-PMMA). Instead of using a water or alcohol phase, TiCl₄ or titanium tetraisopropoxide precursors were used to synthesize the TiO₂ NPs in tetrahydrofuran, which is a good solvent for block copolymers. 3-(Methacryloyloxypropyl)trimethoxy silane and cetyltrimethylammonium chloride

amphiphilic surfactants were used to modify the TiO₂ NPs. This process provides a new approach toward the selective dispersal of quantum-confined NP clusters in a PS-*b*-PMMA diblock copolymer exhibiting an ordered lamellar phase. 3D and 2D nanostructure of CdS clusters have been prepared in the bulk and as thin films, respectively, by selectively dispersing pre-synthesized CdS NPs, containing hydroxyl groups on their surfaces, in the PEO block of templating poly(styrene-*b*-ethylene oxide) (PS-*b*-PEO) diblock copolymers.^[38–42] Russell et al. reported that mixtures of diblock copolymers and either cadmium selenide- or ferritin-based NPs exhibit cooperative, coupled self-assembly on the nanoscale.^[43] In thin films, the copolymers assemble into cylindrical domains, which dictate the spatial distribution of the NPs; segregation of the particles to the interfaces mediates interfacial interactions and orients the copolymer domains normal to the surface, even when one of the blocks is strongly attracted to the substrate. Figure 1-11 presents a cross-sectional TEM image of 100% PS thiol-coated Au NPs dispersed on a symmetric poly(styrene-*b*-2-vinylpyridine) (PS-*b*-P2VP) block copolymer.^[44] We observe that the PS-coated Au NPs were located near the center of the PS block phase of the lamellar structure, whereas P2VP-coated Au NPs were located in the P2VP domain, as expected. Particles coated with a homopolymer similar to one of those in the copolymer can result in lower enthalpy when segregating into the corresponding domain of the block copolymer. Positioning the particle near the center of the corresponding polymer domain leads to better embedding of the NP because the polymer chains can accommodate particles by moving apart, rather than by stretching. Particles coated with a mixture of PS and P2VP thiols become localized exactly at the interface between the PS and P2VP block phases (Figure 1-11b).

1-1-3-3 Nanoreactors for Nanostructure Production

Block copolymer domains can be used as “nanoreactors” for the synthesis of

inorganic NPs. Reviews of the subject are available.^[45,46] Two basic approaches have been developed. The first involves the binding of inorganic species to the monomer prior to polymerization or to one of the blocks of the copolymer prior to micellization (which may be induced by the ion binding event).^[45] The second, more-important approach, however, involves the loading of preformed micelles, whether in solution or in bulk.

Bronstein and coworkers employed various types of block copolymers to prepare micellar nanoreactors for the fabrication of metallic NPs. In many cases, they took advantage of the fact that the N atoms of poly(vinylpyridine), P2VP, and P4VP allow their copolymers to form complexes with metal salts.^[47,48] For example, they produced palladium clusters through the reduction of Pd(CH₃COO)₂ coordinated to the P4VP micellar cores formed from poly(styrene-*b*-4-vinylpyridine) (PS-*b*-P4VP) diblocks in toluene.^[47,49] Other metal nanoclusters, including cobalt,^[50] Au,^[47-49] rhodium,^[47] and platinum,^[47] have been prepared in a similar manner. The catalytic hydrogenation properties of these nanoclusters have been evaluated.^[47,49] TiO₂ NPs have several interesting applications in such areas as catalysis, water purification, and UV blocking. In a previous study, our group synthesized arrayed needle-like TiO₂ nanostructures using a PS-*b*-P4VP diblock copolymer as the template.^[51] These nanostructures, which exhibited the rutile phase of crystalline TiO₂, were grown on a Si substrate presenting TiO₂ seeds prepared using a thin layer of PS-*b*-P4VP. This approach allowed the needle-like rutile TiO₂ nanostructures to be fabricated with variable spatial locations and densities. For example, the distance between two TiO₂ needle bunches could be controlled from 120 to 160 nm when using block copolymer templates of different molecular weights (Figure 1-12).

1-1-3-4 Photonic Crystals

Photonic crystals are attracting a huge amount of attention because they can be used to control and confine light. Materials with a complete bandgap reflect light (incident from any direction) within the wavelength range of the gap. Block copolymers are interesting materials with which to construct photonic crystals because they can self-assemble into periodic structures in one, two, and three dimensions. The inherently low dielectric contrast between the polymeric domains can be overcome through selective doping and/or removal of one component.

Theoretical predictions have revealed the possibility of photonic bandgaps existing in single- and double-network bicontinuous cubic structures.^[52] These calculations have indicated, however, that (for the parameter space explored) no complete bandgaps exist for bicontinuous double primitive, double gyroid (body-centered cubic), or double diamond (face-centered cubic) structures. Bandgaps are anticipated for the single-network analogues, with the best candidate being single-diamond structures exhibiting dielectric contrast as low as 3.6. The optical reflectivity characteristics of an experimentally realized large-domain double-gyroid structure have been assessed.^[40] The initial material selected was a PS-*b*-PI diblock of high molar mass, leading to a cubic lattice parameter a of 258 nm. The optical properties were measured for a bulk film and for a sample in which the PI block was removed through UV/ozone treatment (Figure 1-13), creating an interpenetrating PS network structure. As anticipated theoretically, a complete bandgap was not observed, although a wavelength range with high reflectivity was identified. This range shifted to lower wavelength in the etched structure.

1-2 Nanoparticles

Colloidal nanocrystals are sometimes referred to as “artificial atoms” because the density of their electronic states—which controls many of their physical

properties—can be widely and easily tuned by adjusting the crystal’s composition, size, and shape. The combination of size- and shape-dependent physical properties and ease of fabrication and processing makes nanocrystals promising building blocks for materials possessing designed functions.^[53,54] The ability to control the uniformity of the size, shape, composition, crystal structure, and surface properties of nanocrystals is not only of technological interest: access to defined nanoscale structures is essential to uncovering their intrinsic properties, unaffected by sample heterogeneity. A rigorous understanding of the properties of individual nanocrystals will enable us to exploit them, making it possible to design and build novel electronic, magnetic, and photonic devices—and other functional materials based on these nanostructures.

1-2-1 Semiconductor Nanoparticles

Semiconductor NPs possess inorganic cores that are stabilized by a layer of surface surfactants. NPs featuring semiconductors as the inorganic material—so-called quantum dots—exhibit size-tunable band gaps. Quantum dots exhibit two defining characteristics: the *surface area effect* and the *quantum confinement effect*. The surface area effect exist for particles in a small size regime, where a large percentage of the atoms are located on or near the surface; for example, 99% of the atoms are positioned on the surface for a 1-nm-sized particle.^[55] Such a vast interface between the NPs and the surrounding medium can have a profound effect on the particles’ properties; for example, the imperfect surface of the NPs may act as electron and/or hole traps upon optical excitation. Thus, the presence of these trapped electrons and holes can, in turn, modify the optical properties of the particles. In the quantum confinement effect, “confinement” and “quantization” have two closely related definitions: if a particle is “confined,” then its energy is “quantized,” and vice versa. According to the dictionary, to “confine” mean to “restrict within

limits” to “enclose”, and even to “imprison”. Quantum confinement not only causes an increase in the energy gap (a blue shift of the absorption edge) and splitting of the electronic states but also changes the densities of state and the exciton oscillator strength.^[56] Many of the differences that exist in the electronic behavior of bulk and quantum-confined low-dimensional semiconductors are due to differences in their densities of state.

1-2-1-1 CdSe Nanoparticles

In 1993, Murray, Norris, and Bawendi described the preparation of nearly monodisperse CdS, CdSe, and CdTe semiconductor NPs.^[57] CdSe NPs are potential building blocks for new electronic and optical nanodevices, such as light-emitting diodes, solar cells, lasers, and biological labels.

1-2-2 Metal Nanoparticles

Physicists predicted that metal NPs in the diameter range 1–10 nm (intermediate between the sizes of small molecules and bulk metals) would display electronic structures that reflect their electronic band structures, owing to quantum-mechanical rules.^[58] The resulting physical properties are those of neither the bulk metal nor molecular compounds; instead, they depend strongly on the NP’s size, shape, interparticle distance, and nature of the protecting organic shell.^[59] The few “last metallic electrons” are used for tunneling processes between neighboring particles—an effect that can be detected through impedance measurements that distinguish intra- and intermolecular processes.

1-2-2-1 Au Nanoparticles

Au NPs are the most stable metal NPs. They are fascinating materials for applications in several fields; for example, materials science (because of their multiple modes of assembly), physics [because of the behavior of individual particles and their size-related electronic, magnetic, and optical properties (quantum size effect)],

catalysis, and biology. The bottom-up approach exploited in nanotechnology is making them key materials and building blocks for the 21st century.

As mentioned above, the few “last metallic electrons” of Au NPs are used for tunneling processes between neighboring particles. The *quantum size effect* is involved when the de Broglie wavelength of the valence electrons is of the same order as the size of the particle itself. In such a system, the particles function electronically as zero-dimensional quantum dots (or quantum boxes) that behave according to quantum-mechanical rules. Freely mobile electrons are trapped in such metal boxes and display a characteristic collective oscillation frequency of the plasma resonance, giving rise to the so-called plasmon resonance band (PRB) observed near 530 nm in the 5–20-nm-diameter range. Au NPs are potential building blocks for memory cells,^[60] single-electron transistors,^[61,62] biological sensors,^[63] and catalysts.^[64]

1-3 Block Copolymer/Nanoparticle Mixtures

Diblock copolymer/NP nanocomposites have attracted much attention because the microphase separation of the copolymer can direct the spatial distribution of NPs and, thereby, tailor the properties of the composite. In recent years the preparation of various types of block copolymer/NP composite materials has progressed dramatically, placing the polymer–NP interface in the limelight of assembly processes.^[65–68] Composite structures on the nanometer length scale promise to be candidates for next-generation materials, with many applications expected for nanocomposite-based devices.^[69] An important aspect of this endeavor is the incorporation of non-polymeric properties into a polymeric matrix; this process can be achieved only as a result of the unique properties of nanoparticulate structures. Understanding the basic principles determining the optical, electronic, and magnetic

properties of the resulting composites will allow the construction of ordered arrays of NPs within polymer matrices to become an important means of tuning the properties of nanocomposites.

1-3-1 Controlled Arrangement of NP Arrays in Block Copolymer Domains

Nanoscience is at present searching for simple methods to arrange nanosized objects by means of bottom-up processes. Self-assembly processes are the method of choice to achieve this goal, focusing on the tailoring of supramolecular and interfacial forces and interactions. Thus, nanostructured diblock copolymer open up new avenues for fabricating ordered NP arrays using simple solution procedures.

1-3-1-1 Theory and Simulation

Theoretical and computer simulation investigations of NP–polymer composites have revealed the detailed mechanisms responsible for the development of their structures and physical properties. Huh et al. performed lattice Monte Carlo simulations to examine the phase behavior of NPs in melted-block copolymer domains.^[70] Thompson et al. studied A–B block copolymer–NP composites using a combination of self-consistent field theory (SCFT) for the block copolymer and density functional theory (DFT) for the NPs (Figure 1-14).^[71] To simplify the effect between the block chains and the NPs, they set the enthalpic interaction Flory–Huggins parameter of a particle P to a value of χ_{AP} of 0, thereby treating the particles as identical to the A-block phase (enthalpic interaction Flory–Huggins parameter $\chi_{AP} = 0$) and repelling it by the B-block phase ($\chi_{BP} = \chi_{AB} = \chi_{BA}$), causing the particles to localize preferentially in the A domains. They found that larger NPs were located at the center of the preferred copolymer domain; smaller NPs were driven nearer to the A–B interface as a result of the domination of the translational energy of the NPs in relation to the reduced chain stretching of the A chains. The specific morphology of the nanocomposite depended not only on the block

copolymer's architecture but also on parameters such as the size and volume fraction of the particles. Diblock copolymer melts in the lamellar phase featuring spherical NPs that have an affinity for one particular block were predicted to have lower tensile moduli than those of the corresponding pure diblock-copolymer systems^[72] because of swelling of the lamellar domain by the NPs and the displacement of macromolecules by the elastic inert fillers (NPs). Lee et al. used SCFT to study nanocomposites confined between walls, concluding that perpendicular or parallel orientations of the lamellae were preferred depending on the NP concentration and size and the strength of their interactions with the copolymers or walls.^[73] Schultz et al. performed discontinuous molecular dynamics (DMD) simulations of block copolymer–NP composites,^[74] revealing that NPs that do not interact with either blocks A or B tend to localize at the A–B interface, whereas NPs that repel block A tend to localize in domain B. The specificity of the localization increased with the NP size for neutral and strongly interacting NPs, but decreased for moderately interacting NPs. Small NPs have the largest effect on the periodic spacing, increasing the periodic spacing as a function of NP interaction strength. In general, the effect of the NPs on the periodic spacing decreases as the size of the NPs increases.

1-3-1-2 Methods to Control the Spatial Distribution of NPs in a Block Copolymer

1-3-1-2-1 In Situ Method

Metal NPs can be incorporated into the block copolymer domain by using in situ preparation methods, i.e., reduction of metal ions in one of the block domains.^[75] Sohn et al. fabricated a multilayered nanostructure of alternating pure polymeric lamellae and Au NP-containing lamellae by using thin films of symmetric PS-*b*-P4VP and in situ preparation at room temperature.^[76] First, multilayers of lamellae aligned parallel to the substrate were prepared on silicon wafers or mica substrates. After annealing, the thin films of PS-*b*-P4VP were immersed into ethanol solutions of

HAuCl₄. The thin films loaded with HAuCl₄ were then dipped into a NaBH₄ solution to reduce the precursors to Au NPs selectively in the parallel lamellae of the P4VP block.^[77] In this process, tetrachloroaurate ions [AuCl₄]⁻ (from the gold precursor) become coordinated to the pyridine units of the P4VP block by protonation and, thus, are located selectively in the P4VP layers. The loaded precursors are the reduced by the aqueous NaBH₄ solution to form Au NPs within the P4VP layers. The precursors and reducing agents diffuse readily through each PS layer because ethanol and water can swell only the P4VP block.^[78] Figure 1-15 displays a multilayered structure of alternating PS layers and Au NP-containing P4VP layers.

1-3-1-2-2 Ex Situ Method

One of the first composite materials containing metal NPs and diblock copolymers was reported by Hamdoun et al.^[79] Maghemite (Fe₂O₃) was prepared with desired features and then coated with a compound that could “dissolve” in a melt of one of the block phases but not in that of the other. A grafted short chain of polystyrene was used to cover the maghemite NPs to facilitate their dissolving in one part of the two blocks of a symmetric polystyrene-*b*-poly(butyl methacrylate) (PS-*b*-PBMA) lamellar structure. Indeed, a high concentration of NPs was distributed homogeneously within the PS microdomains. For semiconductor NPs, selective sequestration has been demonstrated for pre-synthesized surface-modified TiO₂ and CdS NPs into single blocks of PS-*b*-PMMA^[37] and PS-*b*-PEO,^[38] respectively. After the preparation of the NPs, the particle core size is the most significant parameter affecting the localization of particles along the interface between the two blocks or at the center of the respective polymer domain. The self-assembly of two kinds of NPs simultaneously directed on a monolayer film of diblock copolymer micelles, reported by Sohn et al., was also considered with respect to the size of each particle.^[80] Dodecanethiol-protected Au NPs (R = 5.4 nm)

immersed in PS-*b*-P4VP spherical micelles resulted in the Au NPs being decorated around the hexagonally ordered micelles; they were not, however, located in the entire PS corona because they were much smaller than the PS-*b*-P4VP micelles. When surface-modified Au NPs were added to PS-*b*-P4VP micelles containing FeCl₃ (R = 16 nm), the Au NPs surrounded the hexagonally ordered iron oxide NPs (Figure 1-16). Larger-sized iron oxide NPs were located in the centers of the P4VP domains; the ordering was preserved after plasma etching of the polymeric matrix.

1-3-1-2-3 Methods Using External Fields

UV-light irradiation has often been used to prepare templates or holes for NP arrangement. Exposure of a thin film of PS-*b*-PMMA to UV irradiation decomposes the PMMA phase and induces crosslinking of the PS phase, thereby producing an ideal template wherein NPs could be sequestered.^[31,81] A spin-coated thin film of PS-*b*-PMMA that was exposed to UV light under vacuum and immersed in glacial acetic acid led to selective removal of the degraded PMMA phase from the PS matrix.^[82] The resulting hexagonally ordered cylindrical pores acted as templates when dipped into a solution containing NPs, leading to the efficient sequestration of NPs into the pores. There are two parameters that are critical to the success of this procedure: the diameter of NPs should be smaller than that of the nanopores and the ligands stabilizing the NPs should not exert a strong affinity toward the PS matrix. Figure 1-17 presents the TEM image of a template featuring 17-nm-diameter pores filled with 10-nm-diameter CdSe NPs.

1-3-1-2-4 Directed Chemical-Binding Methods

The direct chemical binding of NPs onto block copolymer surfaces is also an important method in generating ordered particle arrays.^[83,84] The critical points affecting the direct binding between NPs and block copolymers are (a) the chemical nature of the block copolymer domain to which the NPs will be bound, (b) the

chemical structure of the shell around the NPs, and (c) the interaction between the surface of the block copolymers and the NPs. The deposition of layered NPs on the polymer surface, mediated by covalent bonds, has been described; it relies mainly on supramolecular interactions^[85] (e.g., the molecular printboards of Reinhoudt and co-workers),^[86] hydrogen bonding systems,^[87] and purely electrostatic assembly^[65,88] at appropriately structured surfaces. In another approach, our group used strong hydrogen bonding interactions to bind Au NPs onto microphase-separated block copolymer films deposited on surfaces (Figure 1-18).^[89] Au NPs (diameter: 5 nm) were coated with ligands featuring barbituric acid moieties. Block copolymers were prepared bearing the matching receptor (i.e., the so-called Hamilton receptor) in one of the blocks and a fluorinated side chain in the other block to enhance the degree of microphase separation. The binding of Au NPs onto the block copolymer surface was mediated by the strong interactions existing between the barbituric acid and Hamilton receptor units.

1-3-2 Interests to Block Copolymer/NP Nanocomposites

1-3-2-1 NP-Induced Phase Transformation

In a previous study, our group reported the morphological transformation of a PS-*b*-P4VP diblock copolymer—from a hexagonally packed cylinder structure to a lamellar structure—that occurred upon sequestering CdS NPs in the P4VP block.^[90] The surface of the CdS NPs was stabilized with mercaptoacetic acid as a surfactant, rendering each CdS NP hydrophilic. Whereas pure PS-*b*-P4VP possessed a hexagonally packed cylindrical structure, the composite transformed into a lamellar structure in the presence of 7 wt% of the CdS NPs (Figure 1-19). This morphological transformation, from a cylindrical to lamellar structure, was mediated by strong interaction forces, such as hydrogen bonds, between the carboxylic acid units of the CdS NPs and the P4VP chains. Such an NP-induced phase

transformation was also reported by Kramer's group; they used polymer-coated Au NPs to induce phase transformations that were affected by the choice of solvent or the depth of the bulk film.^[91]

1-3-2-2 Interfacial Interactions

Interfacial interactions significantly affect the spatial distribution of NPs within homopolymers and block copolymers and the global structure of the particle-filled systems. Bockstaller et al.^[92] observed that the localization of particles along the interface or at the center of the respective polymer domains was also affected by the particles' core sizes. In a system consisting of symmetric polystyrene-*b*-ethylene propylene (PS-*b*-PEP), large silica NPs ($d = 21.5$ nm; $d/L = \text{ca. } 0.26$; d : particle diameter; L : respective domain dimension of the block copolymer) were located at the center of the PEP domain. Smaller Au NPs ($d = 3.5$ nm; $d/L = \text{ca. } 0.06$) segregated at the interface between two block phases (Figure 1-20) in accordance with theoretical simulations.^[71] Interfacial segregation of NPs is expected to occur for particle sizes at which d/L is less than 0.2; localization of NPs at the center of the lamellar phase is expected for values of d/L that are greater than 0.3.

1-3-2-3 Proximity Effects in Block Copolymer/NP Composites

Dependent on the surface chemistry of Au nanocrystals of equal metal core size, two morphological types of self-organized block copolymer-particle blends are observed (Figure 1-21).^[93] (1) segregation of nanocrystals to the interfacial areas and (2) preferential uniform distribution within one of the respective polymer domains. Confinement of the nanocrystals to the narrow interfacial regions of the microstructure in the first type of blend results in high local particle filling fractions and gives rise to electromagnetic coupling upon light irradiation, accompanied by a pronounced increase in absorbance.

1-3-2-4 Enhanced Collective Electron Transport

In a previous study, our group reported the collective electron transport behavior of Au NPs confined within a single P4VP nanodomain and within homo-P4VP.^[94] Figure 1-22 displays representative current–voltage scaling data obtained for these two samples at 78 K. The accessible current-conducting pathways are described^[95–99] by Eq. (1-5):

$$I \propto \left(\frac{V}{V_T} - 1 \right)^\zeta \quad (1-5)$$

(for $V > V_T$), where I is the current, V is the voltage, ζ is a scaling exponent, and V_T is the threshold voltage. The scaling exponent ζ can be regarded as the dimensionality for collective electron transport for arrays of dots, as modeled in a previous study.^[99] We obtained power-law scalings (ζ) of 1.31 for the nanodomain-confined sample and 2.84 for the randomly distributed sample. These results indicate that quasi-one-dimensional collective electron transport occurs for the nanodomain-confined Au NPs and that quasi-three-dimensional collective electron transport occurs for the randomly distributed Au NPs.

1-3-2-5 Memory Device Applications

Leong et al. demonstrated the versatility of combining self-assembled block copolymers with in situ room-temperature synthesis of Au NPs in the copolymer matrix as an effective approach toward polymer memory fabrication (Figure 1-23).^[100] Their proof-of-concept experiment revealed the vast potential of these fascinating nanoscaled arrays of NPs. Moreover, they demonstrated the ability to tune the memory behavior by controlling the loading of Au NPs. A memory structure featuring pentacene as the organic semiconductor exhibited a clockwise $C-V$ hysteresis, indicating a net hole trapping effect. This novel structure displayed a large memory window of 2.1 V after writing and erasing modes and a long charge retention ability of ca. 92% over 60,000 s. This approach, by virtue of its simplicity

in design and processing, can realize integrated memory devices and circuits for low-cost plastic electronics applications.

1-4 Organic Electrical Bistable Memory Device

Organic materials have attracted much attention for the construction of large-area, mechanically flexible electronic devices.^[101] Organic light-emitting diodes for flat-panel displays are ready for mass production,^[102] and significant progress has also been made in organic thin-film transistors^[103] and organic solar cells.^[104] There is a strong desire to develop new advanced materials that can overcome the potentially limiting scaling difficulties present in the semiconductor industry. Development of future information technology could come from data storage incorporating these advanced materials. Many methods have been reported for achieving inorganic nonvolatile memory, such as implementing phase-change memory,^[105] programmable metallization cells,^[106] mechanical switches,^[107] quantized atomic switches,^[108] quantum dots,^[109] and nanocrystal memory.^[110] Organic materials are promising candidates for electronic devices in new information technologies.^[111] The devices can be fabricated either through bottom-up methods or by forming composite active layers; they can easily be addressed by x - y cross-wires, i.e., two-terminal structures that sandwich the active layer. The use of organic materials provides a simplified manufacturing process yielding low-cost, flexible, light-weight devices that have an active device area approaching the nanoscale.

1-4-1 Typical I - V Behavior of an Organic Memory Device Organic

In general, the memory effect observed in these organic devices is related to charge storage (including charge trapping, charge separation, and charge transfer) within active components in the organic layer.^[112,113] The critical material requirement for the memory effect is the existence of an energy barrier preventing the

positive and negative charges from recombining, even after the electric bias has been removed. After the materials have been polarized, the device exhibits a conductance change, where a low-conductance (OFF) state switches to a high-conductance (ON) state, resulting in so-called electrically bistable devices. The states are stable for prolonged periods of time, allowing them to be used in nonvolatile memory device applications, such as flash memory and random access memory. In addition to memory applications, organic electronic devices have also demonstrated the potential to be used as switches to drive organic light-emitting diodes for electronic display applications.^[114]

Figure 1-24 displays a typical $I-V$ curve for an Al/PVK/Al memory device.^[115] When the negative bias with respect to the bottom electrode was swept from 0 to -10 V, the leakage current increased abruptly by four orders of magnitude and switched the PVK films to a low-resistance state at -8 V. When sweeping a positive bias from 0 to 5 V, a sudden decrease of the leakage current occurred and the resistance of the oxide was restored to its initial value at 4 V. Consequently, the switching behavior leads to a pronounced hysteretic $I-V$ characteristic with two different resistance states. This behavior reveals the potential for nonvolatile memory in PVK films.

1-4-2 Bistability Mechanisms of an Organic Memory Device Organic

Organic materials have attracted much interest for the fabrication of memory devices that are capable of reversibly switching between two states, often referred to as “0” and “1.” The two states can be controlled by the voltage or current for organic materials exhibiting high and low resistance states. The two distinct resistance states for an organic memory material may be driven through the trapping/detrapping of charges by nanoclusters in the insulator,^[116,117] the rupture and formation of conductive filaments,^[118,119] reduction/oxidation processes,^[120] or

intramolecular conformational changes.^[121]

1-4-3 Reliability of an Organic Memory Device Organic

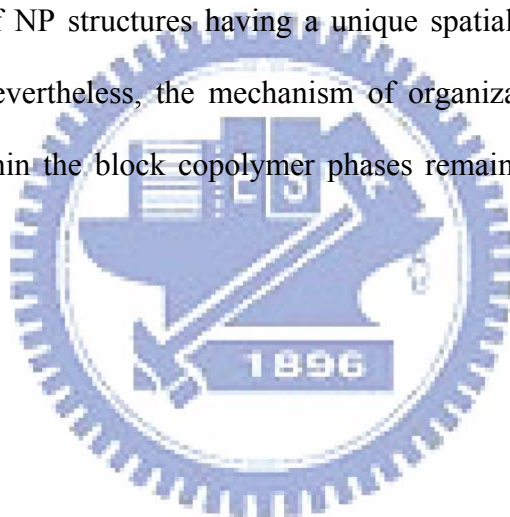
Organic memory devices and organic logic circuits are often characterized by their reliability. The nonvolatile performance criteria that must be satisfied for a device to be considered reliable are data retention for at least 10 years, low power consumption, and at least 10^6 operation cycles. These criteria are comparable to those provided by flash memory. In this Dissertation, we introduce several organic materials and device structures that show promise for memory applications, while also analyzing their bistability mechanisms, retention times, cycling tests, and overall operation. Nevertheless, the technology at this stage has not yet matured, so hopefully we can encourage and provide motivation for further research in this area to provide future technology for memory applications.

1-5 Motivation and Scope of Dissertation

Block copolymers are versatile platform materials because they can self-assemble—if they have appropriate compositions and are subjected to suitable conditions—into various nanostructures having period thicknesses between 10 and 100 nm through microphase separation of incompatible blocks. Nanostructured block copolymers can be used as templates for selectively controlling the spatial position of nanostructured materials within one of the blocks.

Zero-dimensional nanostructures, such as quantum dots and NPs, have diameters in the range 1–10 nm and are the subject of much current research because of their optical, electronic, and chemical properties. Those properties can be controlled through the immobilization and assembly of NPs on an appropriate substrate or in a suitable medium. The important factor in determining the stable incorporation of the NPs within a block copolymer matrix lies mainly in the compatibility of the NPs with

the block copolymer's microstructures, which in turn can be controlled by considering the symmetry of both the included guest and the block copolymer host matrix. Thus, surface modification of the NPs is necessary to stabilize them against aggregation within the block copolymer matrix; this process normally tends to attract the NPs to one of the blocks of a block copolymer and repel it from the other. The resulting materials can, therefore, result in the NPs accumulating into one microphase of a block copolymer, reflecting the pattern that it has formed. If NPs can be incorporated or arranged only into one domain of a microphase-separated block copolymer, it is possible to transfer the microphase separation of the block copolymer into ordered arrays of NP structures having a unique spatial distribution within the matrix polymers. Nevertheless, the mechanism of organization and the degree of order of the NPs within the block copolymer phases remain to be investigated and established.



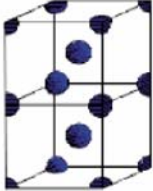

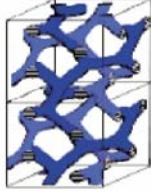
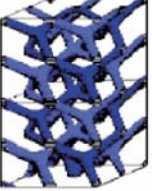

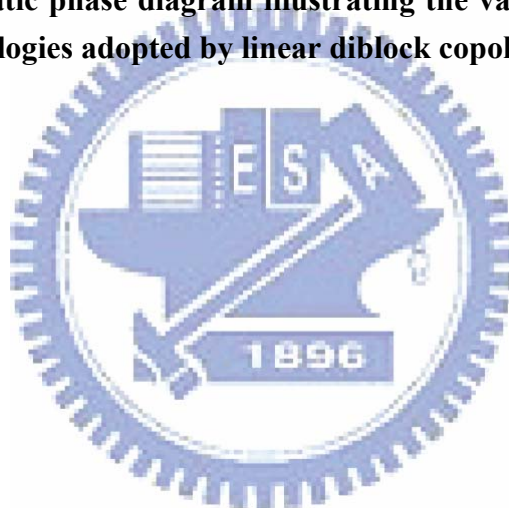
Nature of patterns	Spheres (SPH) (3D)	Cylinders (CYL) (2D)	Double gyroid (DG) (3D)	Double diamond (DD) (3D)	Lamellae (LAM) (1D)
Space group	$Im\bar{3}m$	$p6mm$	$Ia\bar{3}d$	$Pn\bar{3}m$	pm
Blue domains: A block					
Volume fraction of A block	0-21%	21-33%	33-37%		37-50%

Figure 1-1. Schematic phase diagram illustrating the various “classical” block copolymer morphologies adopted by linear diblock copolymers. ^[7]



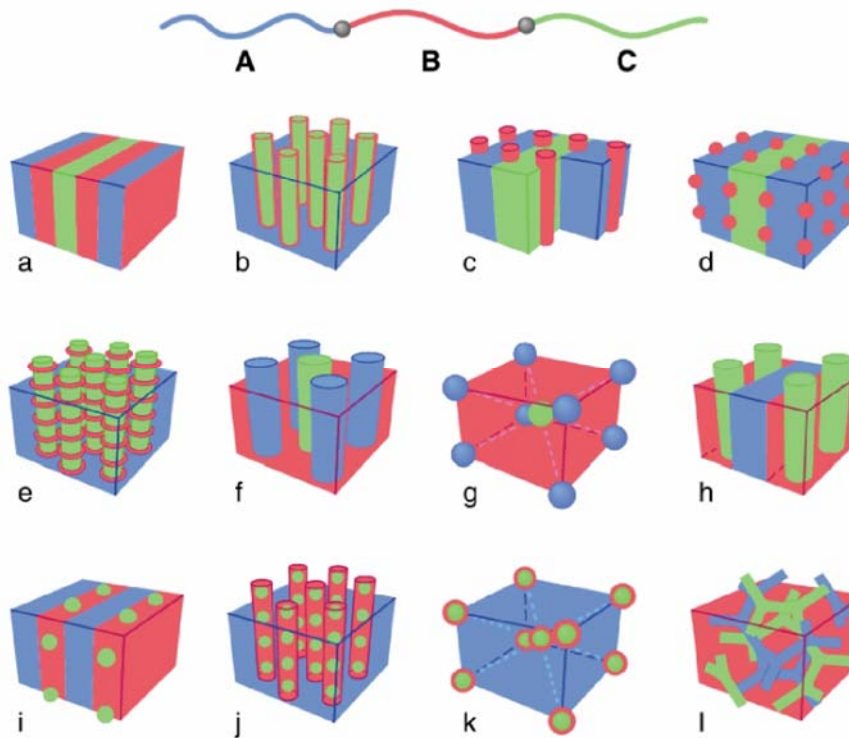


Figure 1-2 Schematic representation of the morphologies of linear ABC triblock copolymers. The combination of the block sequence (ABC, ACB, BAC), composition, and block molecular weights provides an enormous parameter space for the creation of new morphologies.^[7]

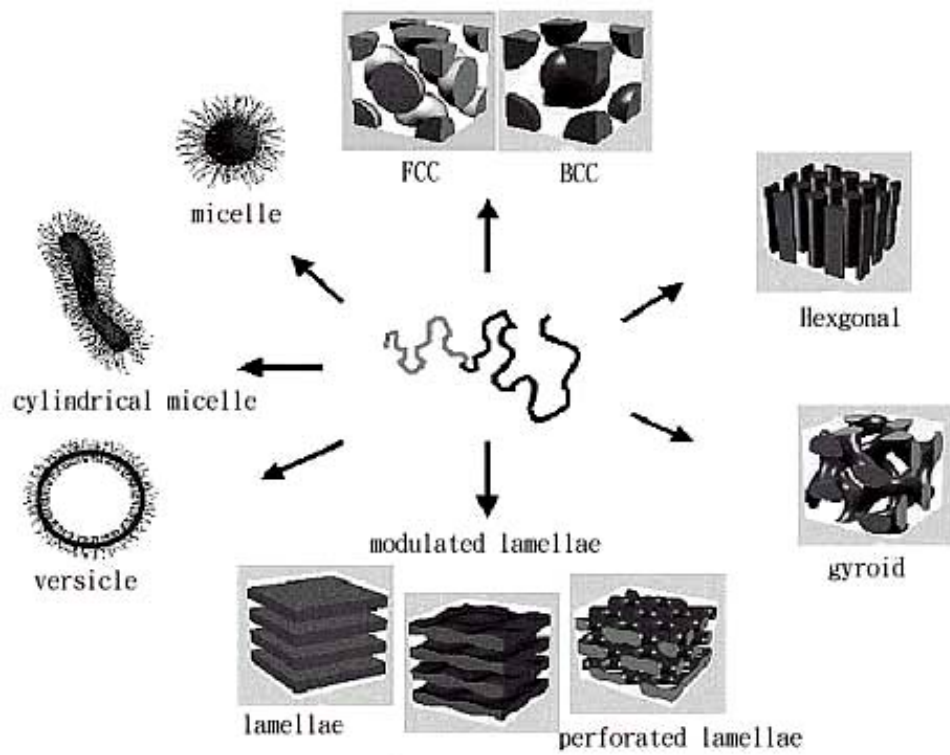
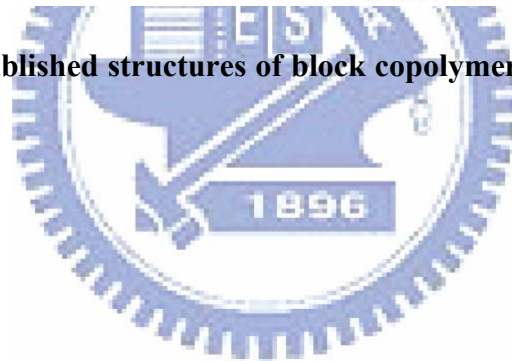


Figure 1-3. Well-established structures of block copolymers in the melt, solution, or solid state. ^[9]



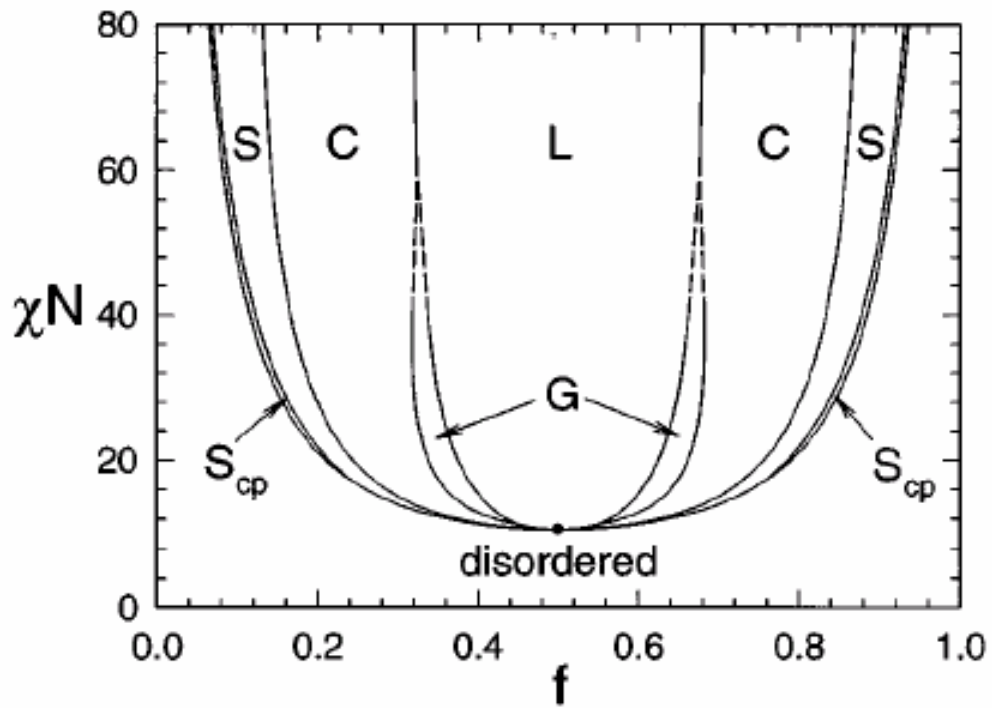
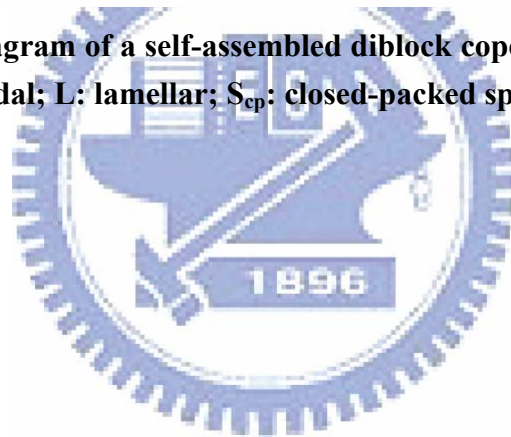


Figure 1-4. Phase diagram of a self-assembled diblock copolymer. S: spherical; C: cylindrical; G: gyroidal; L: lamellar; S_{cp} : closed-packed spherical structure. ^[11]



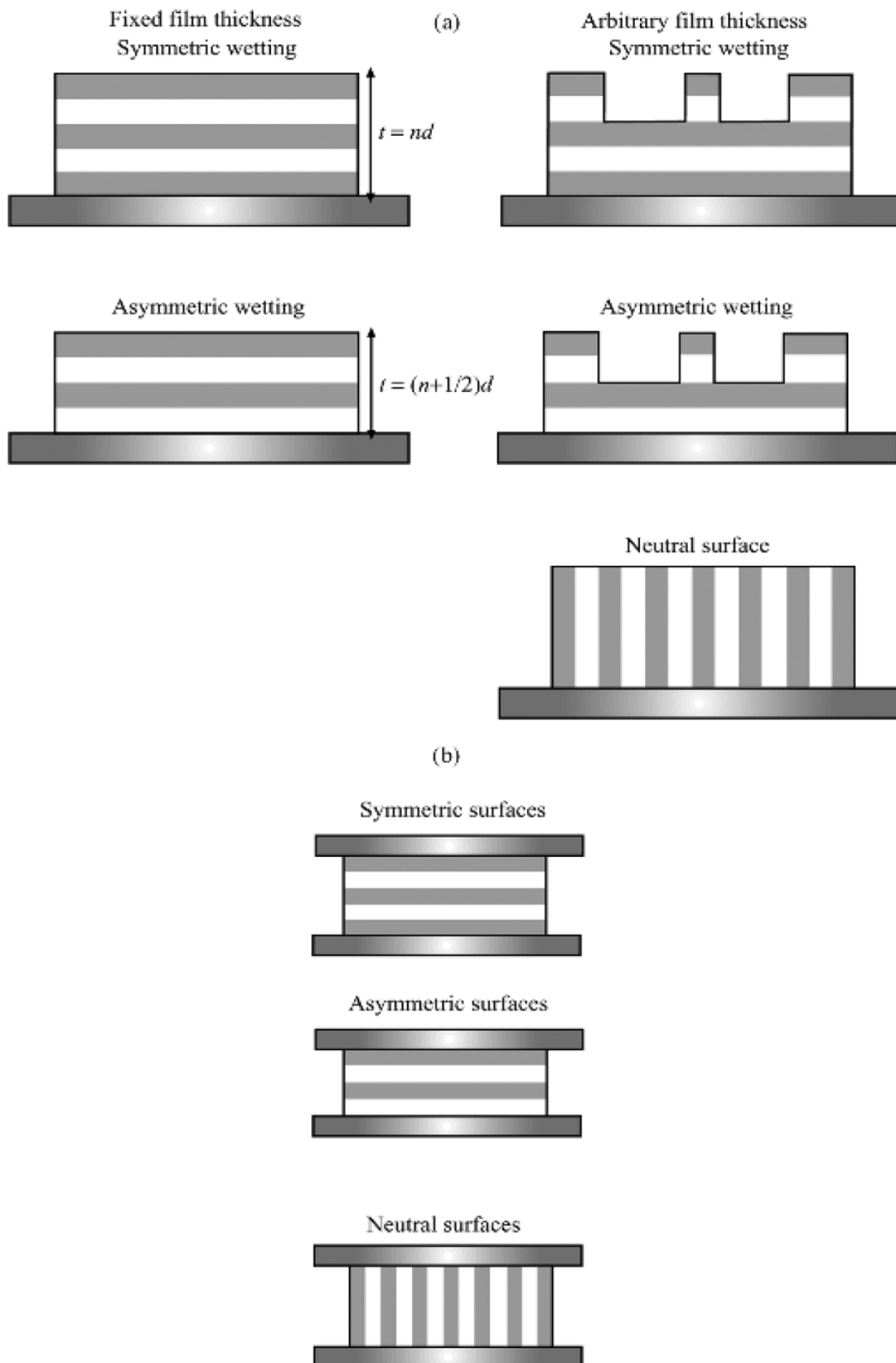


Figure 1-5. Possible configurations of lamellae in block copolymer films. (a) Confined at one surface. (b) Confined at both surfaces.^[28]

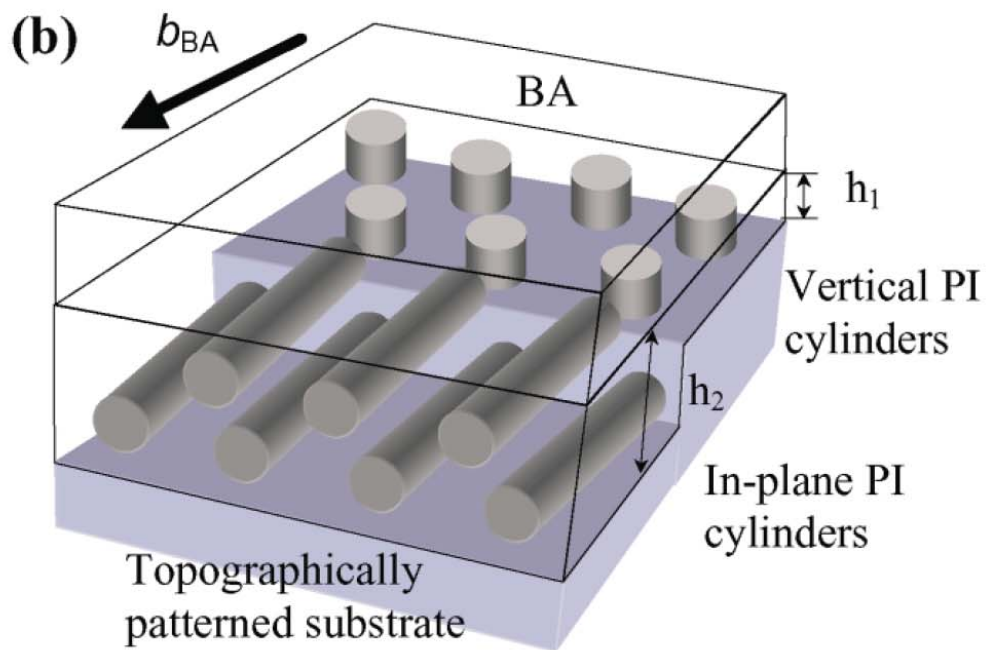
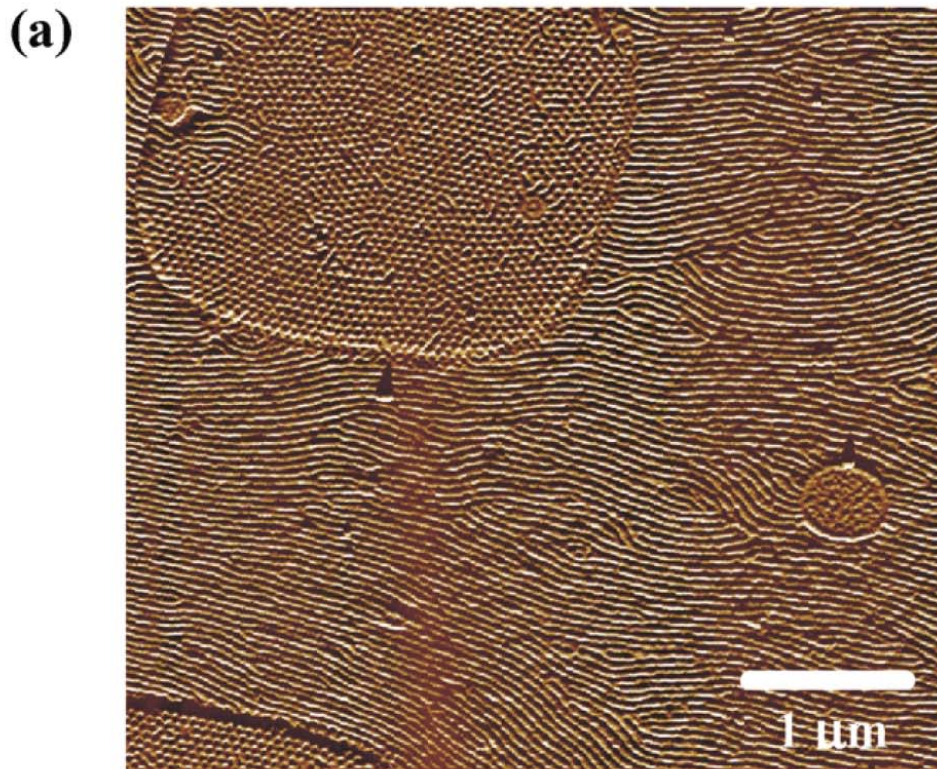


Figure 1-6. Thin film morphology of an asymmetric block copolymer that forms hexagonal morphologies in the bulk. ^[30]

Block Copolymer Nanotechnology

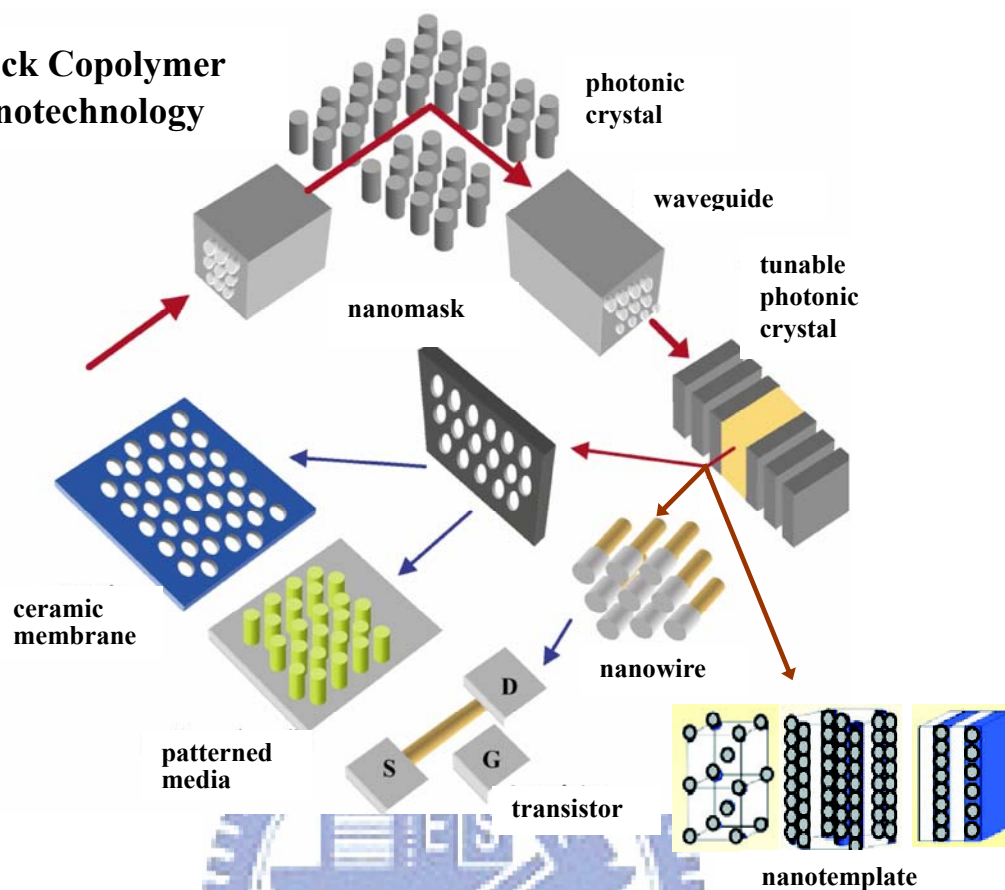


Figure 1-7. Schematic representation of various applications of block copolymers in nanotechnology.^[32]

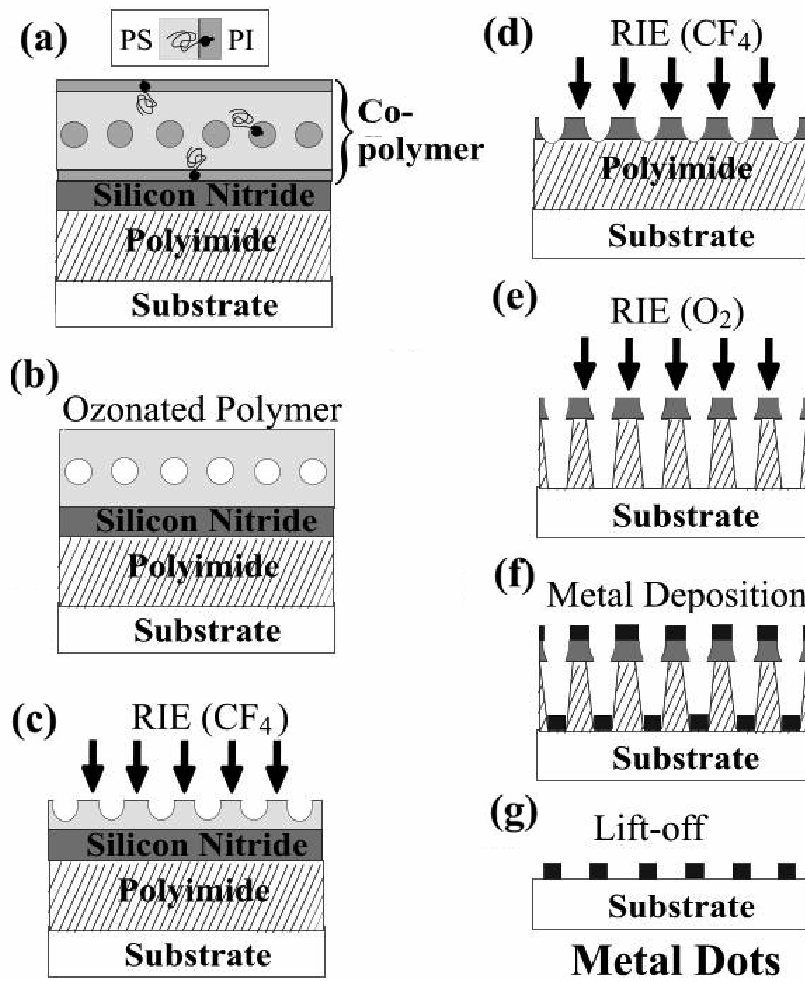


Figure 1-8. Schematic representation of the production process of a metal nanodot array using block copolymer lithography. ^[35]

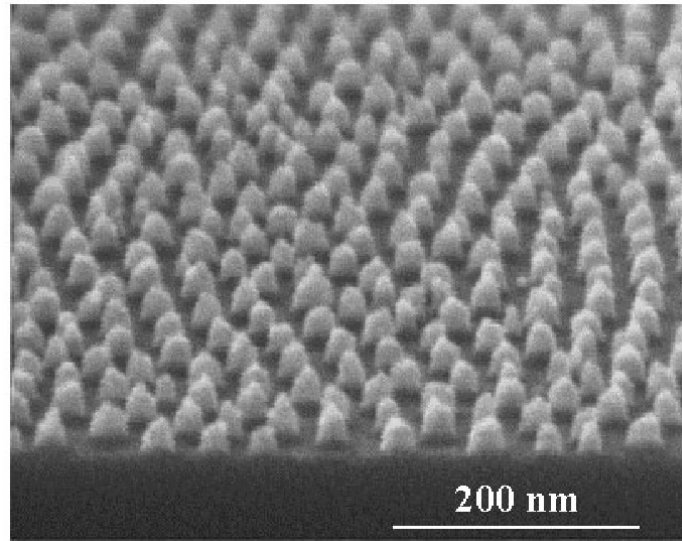
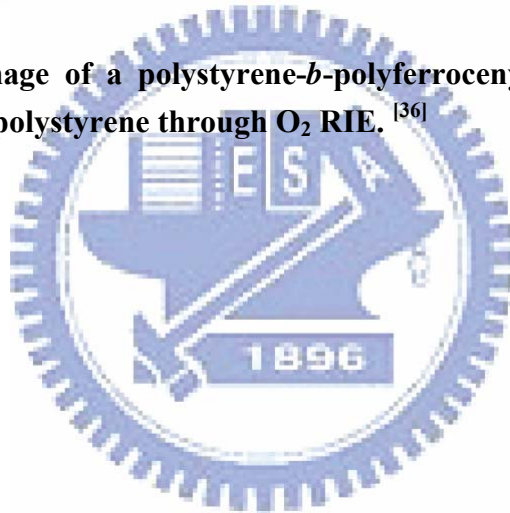


Figure 1-9. SEM image of a polystyrene-*b*-polyferrocenyldimethylsilane mask after removal of the polystyrene through O₂ RIE. ^[36]



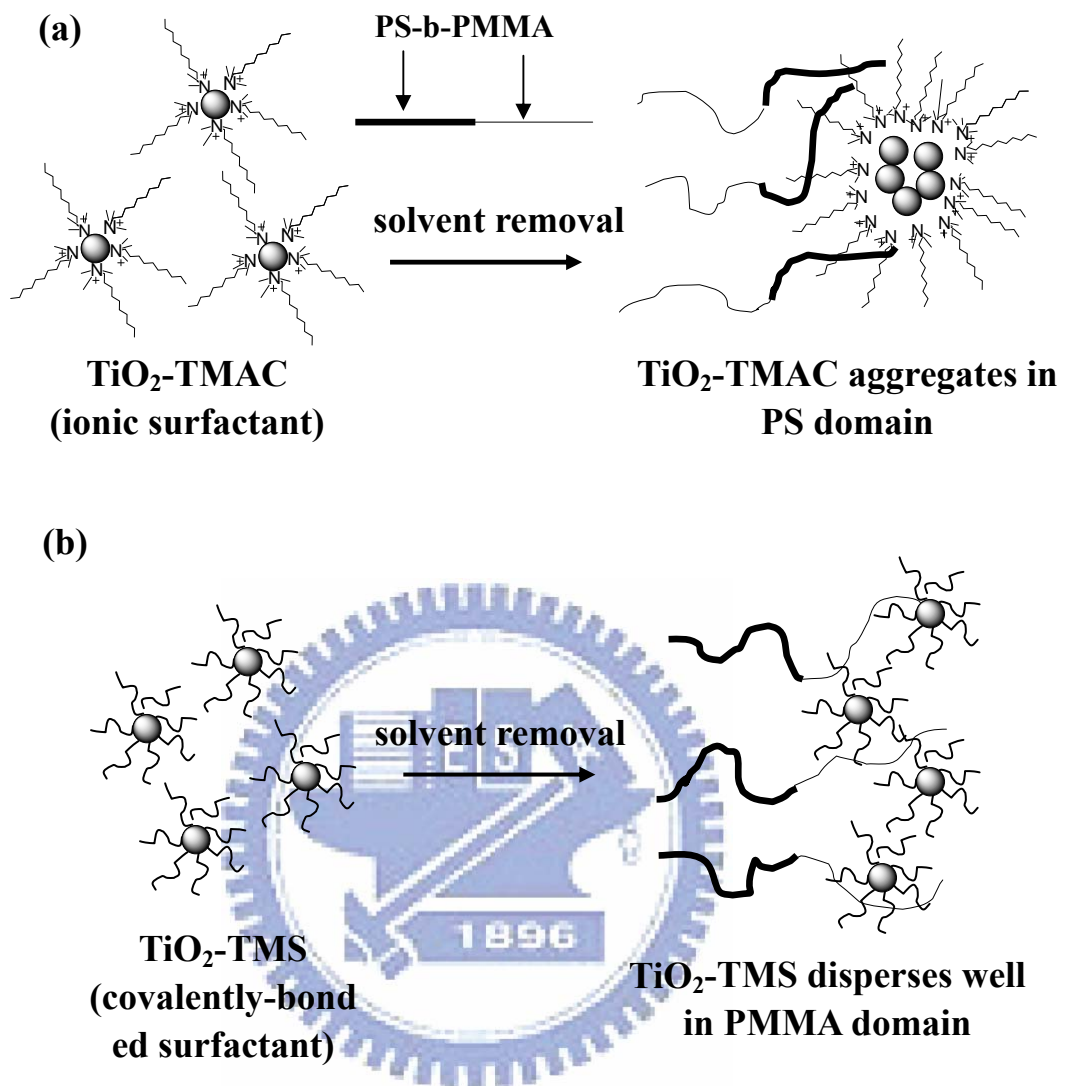


Figure 1-10. Schematic representation of selectively distributed TiO₂ NPs in a PS-*b*-PMMA diblock copolymer.^[37]

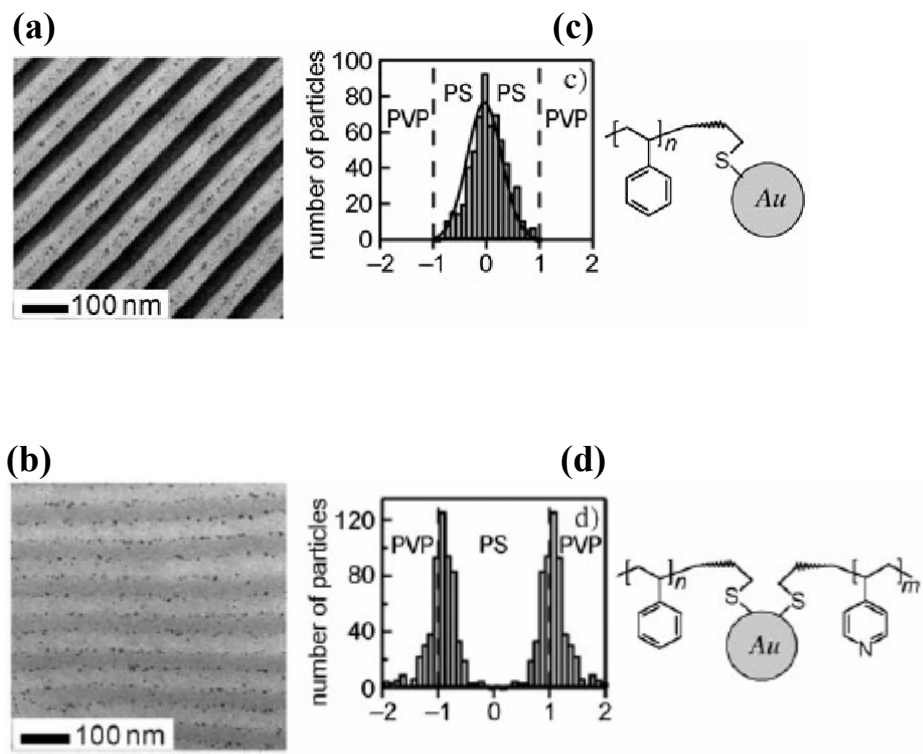


Figure 1-11. (a) Assembly of Au NPs (core: 3.9 ± 1.0 nm; shell: PS; core + shell = 7.7 nm) into PS-*b*-P4VP. (b) Assembly of Au NPs (core: 3.9 ± 1.0 nm; shell: PS and P2VP; core + shell = 7.7 nm) into PS-*b*-P4VP. (c, d) Respective histograms of particle locations for the samples displayed in (a) and (b).^[44]

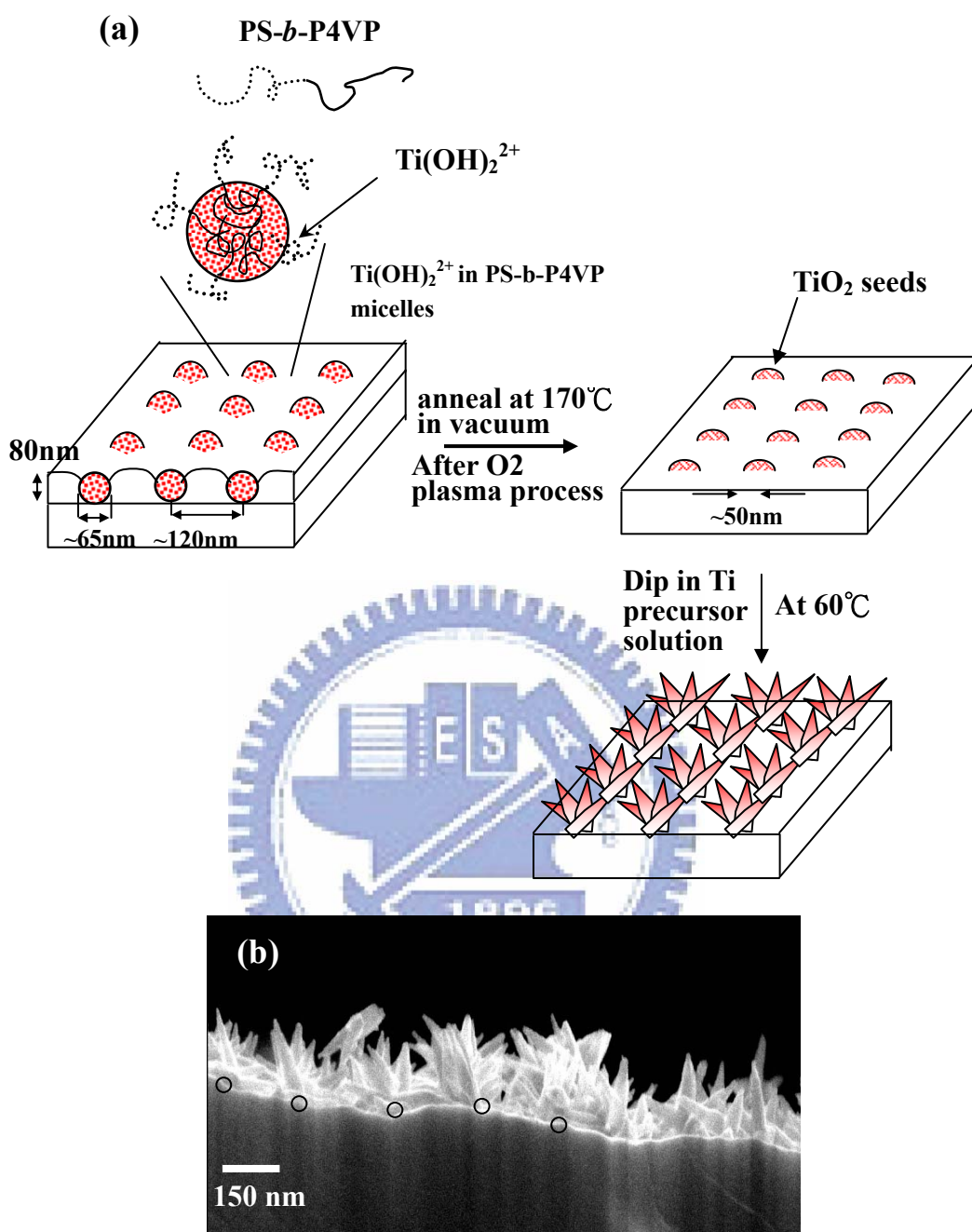


Figure 1-12 (a) Schematic of synthesis of needle-like TiO₂ nanostructures with ordered patterns. (b) The cross-section SEM image of needle-like TiO₂ nanostructures.^[51]

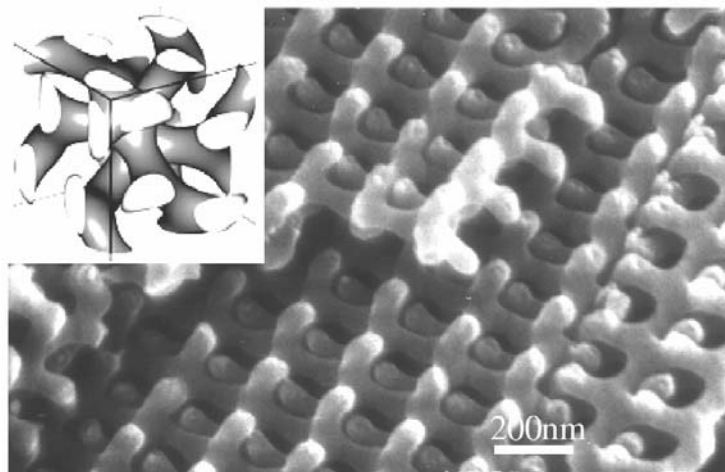
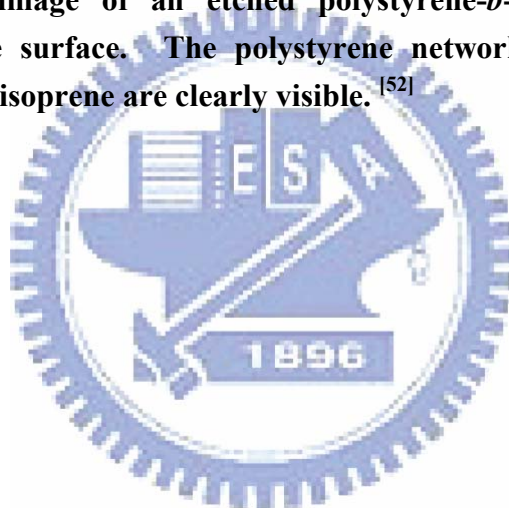


Figure 1-13 SEM image of an etched polystyrene-*b*-polyisoprene diblock, revealing a fracture surface. The polystyrene network channels remaining after removal of polyisoprene are clearly visible. ^[52]



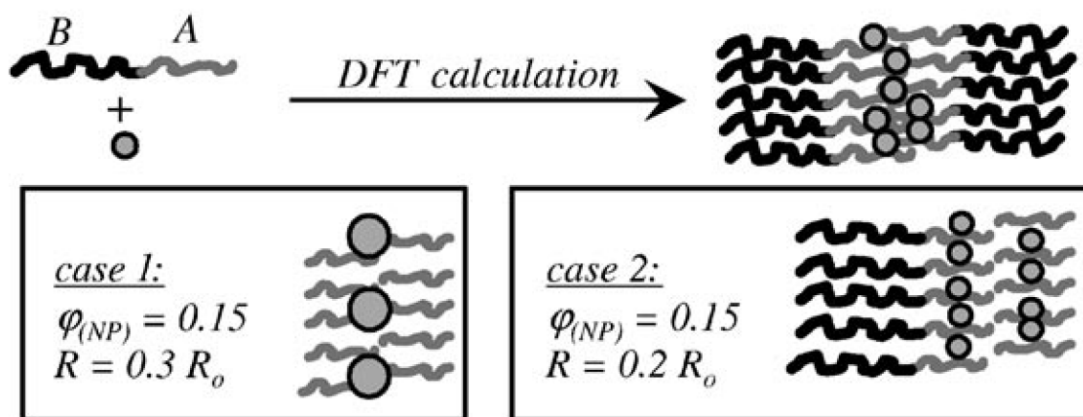
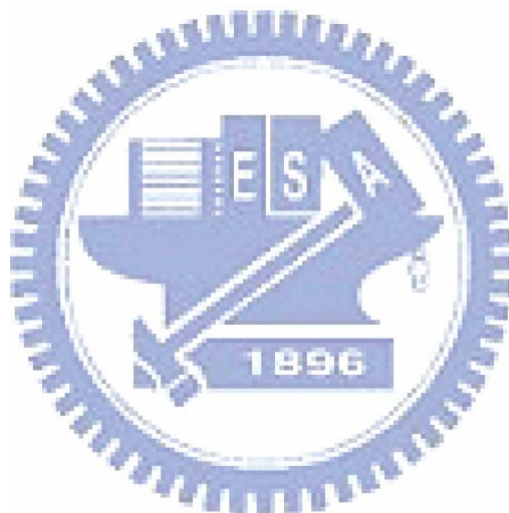


Figure 1-14. Density functional theory calculations of large (case 1) and small NPs (case 2). The NPs are either located at the center of the A phase (case 1) or driven closer to the A–B interface (case 2).^[68, 71]



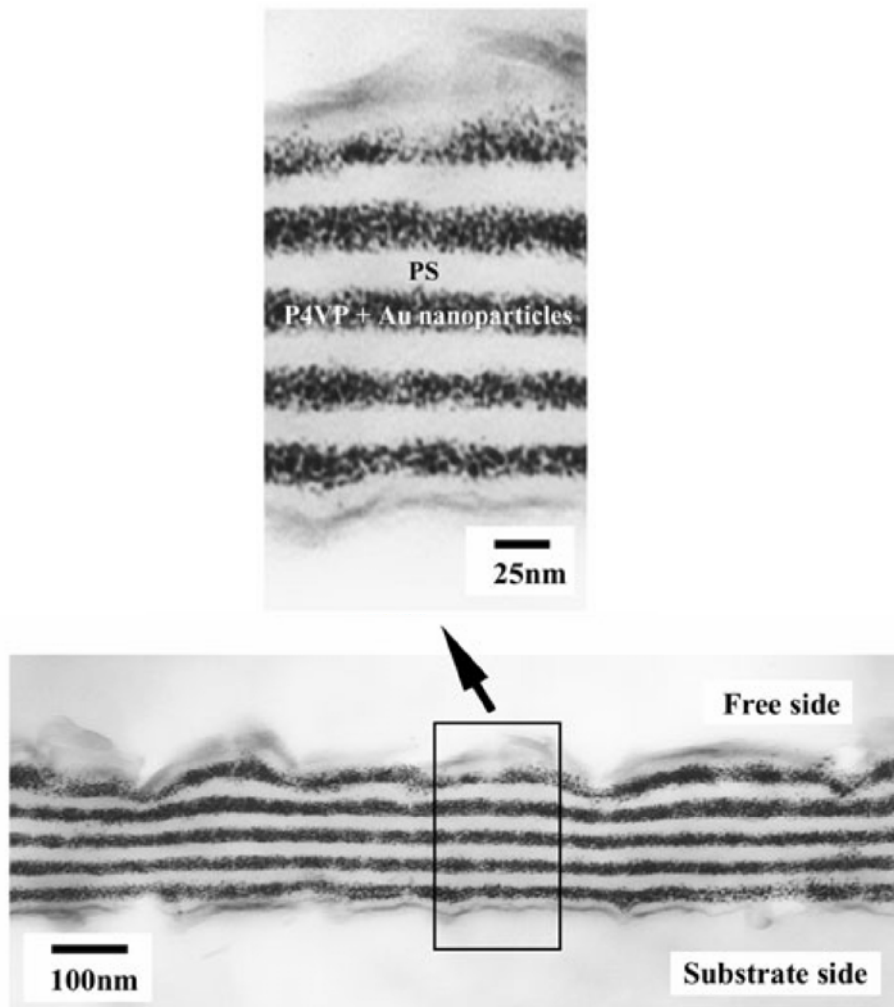


Figure 1-15. Cross-sectional transmission electron micrograph displaying Au NPs patterned within the P4VP lamellae formed by a PS-*b*-P4VP diblock copolymer.^[78]

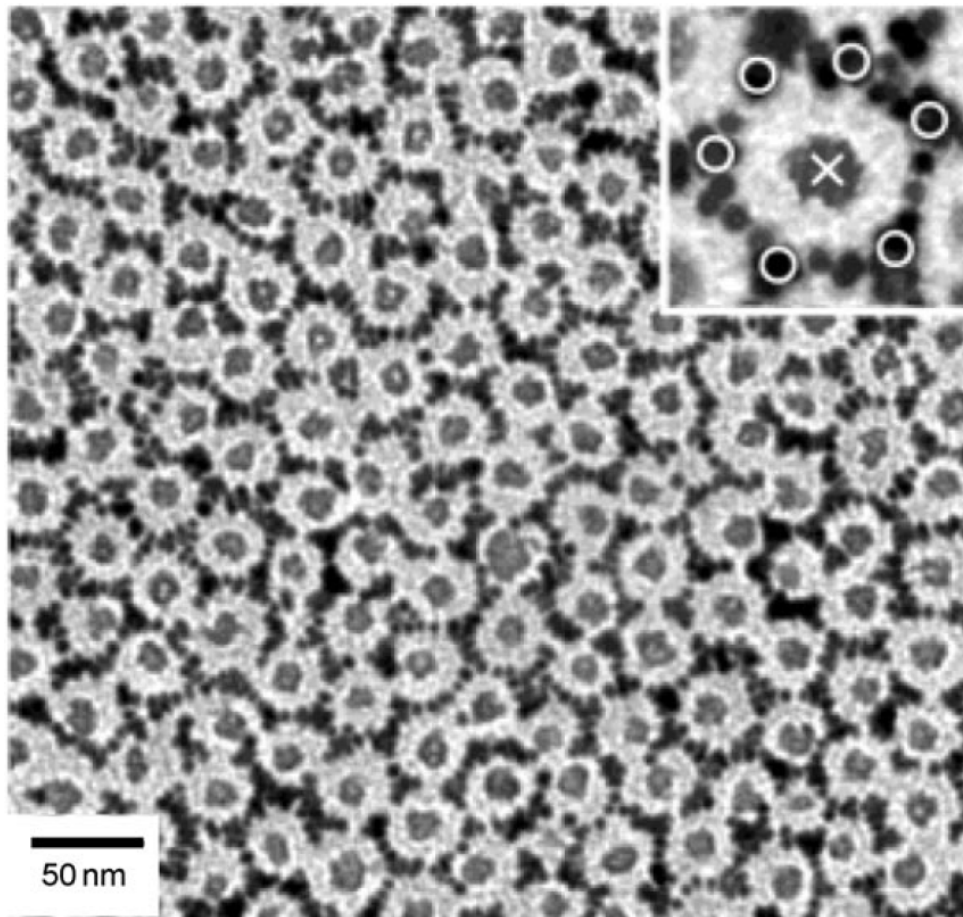


Figure 1-16. TEM image of an array of Fe_2O_3 NPs and 1-dodecanethiol-coated Au NPs in a PS-*b*-P4VP matrix after removal of the polymer matrix through O_2 plasma treatment. The inset displays an enlarged view of Au NPs at the PS-PVP interface; the iron oxide NPs are centered in the former PVP phase. ^[80]

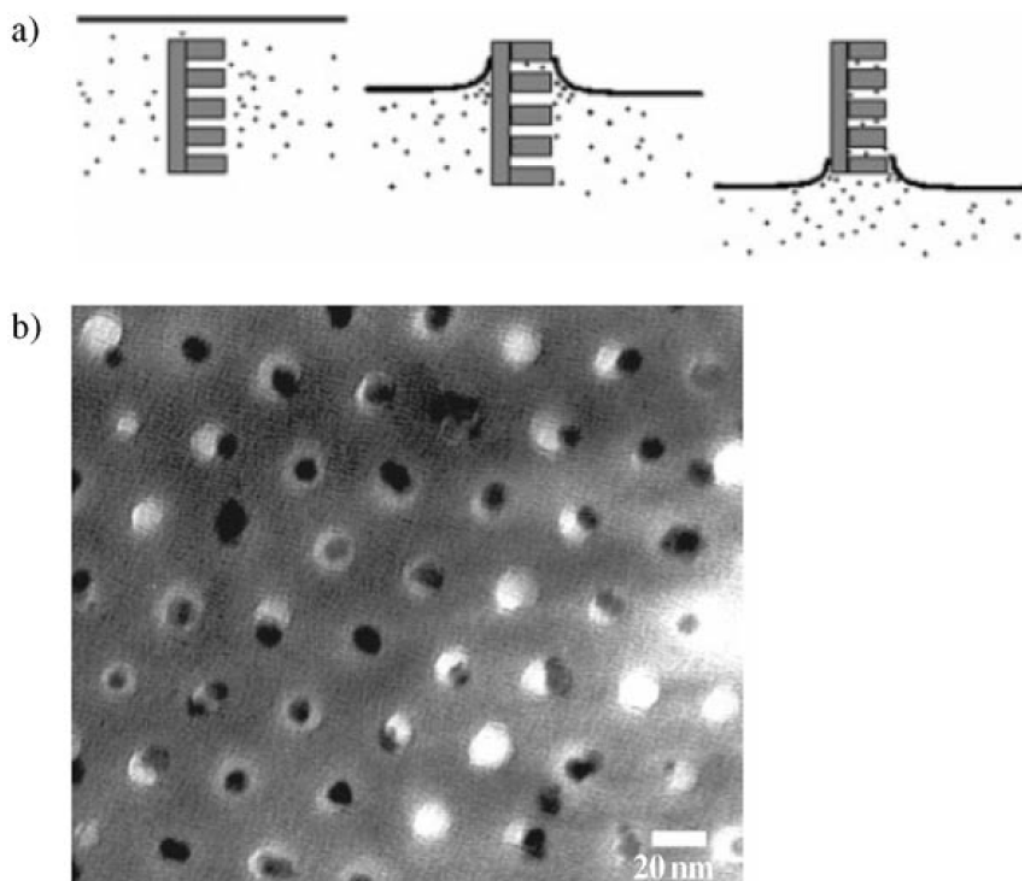


Figure 1-17. (a) NPs (CdSe–TOPO; $R = 5$ nm) deposited into a block copolymer template [PS–PMMA (70:30)] through withdrawal of the template from solution. (b) TEM image of the resulting film; the NPs are located inside the (black) holes.^[82]

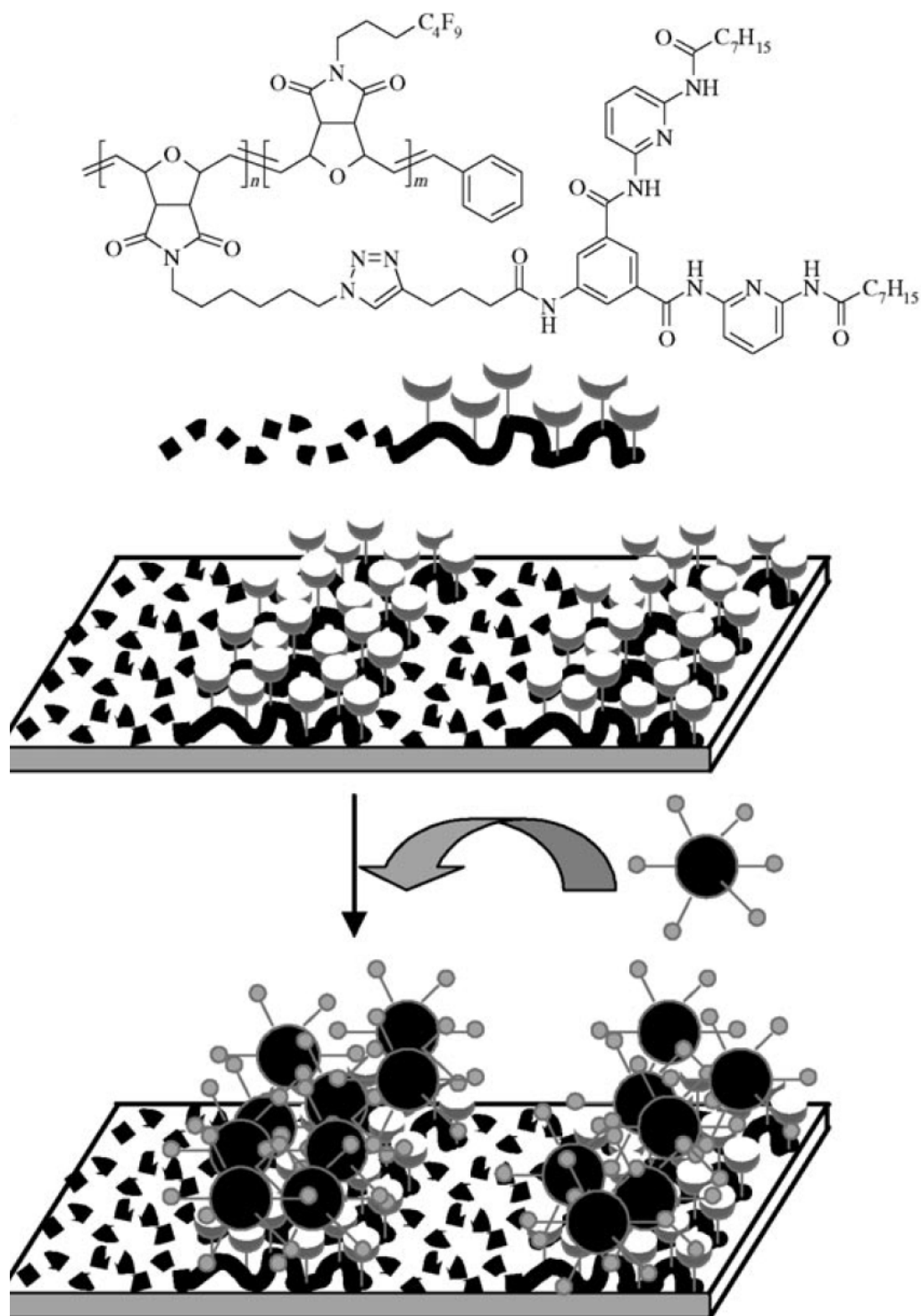


Figure 1-18. Deposition of Au NPs ($R = 2.5$ nm) via directed hydrogen bonding interactions onto a film consisting of a block copolymer. ^[89]

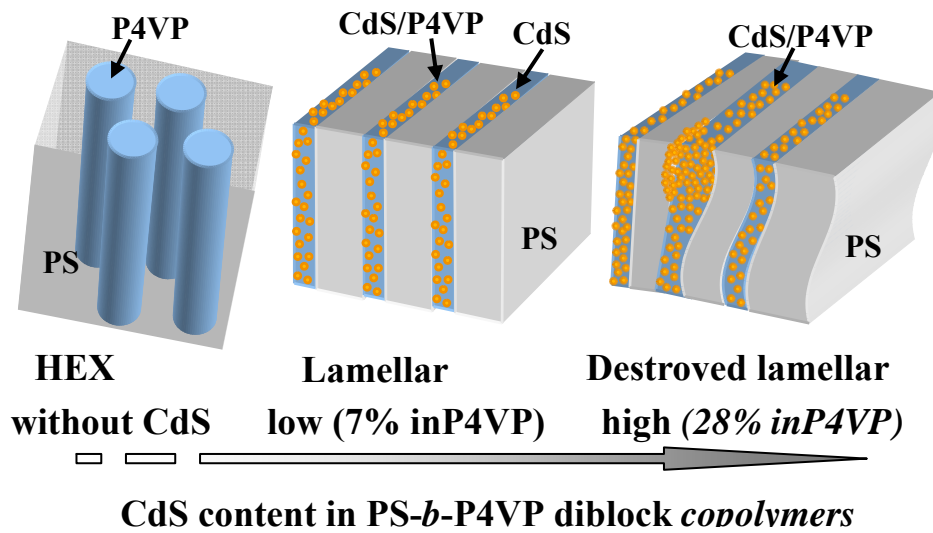
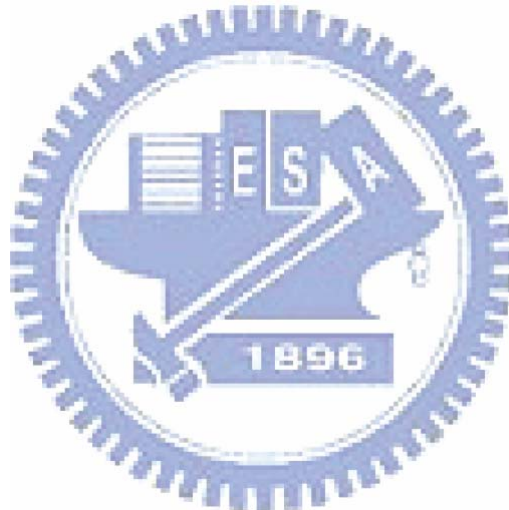


Figure 1-19. Morphological transformation from a hexagonally packed cylinder structure of pure PS-*b*-P4VP diblock copolymers to lamellar (CdS/P4VP)-*b*-PS composites. ^[90]



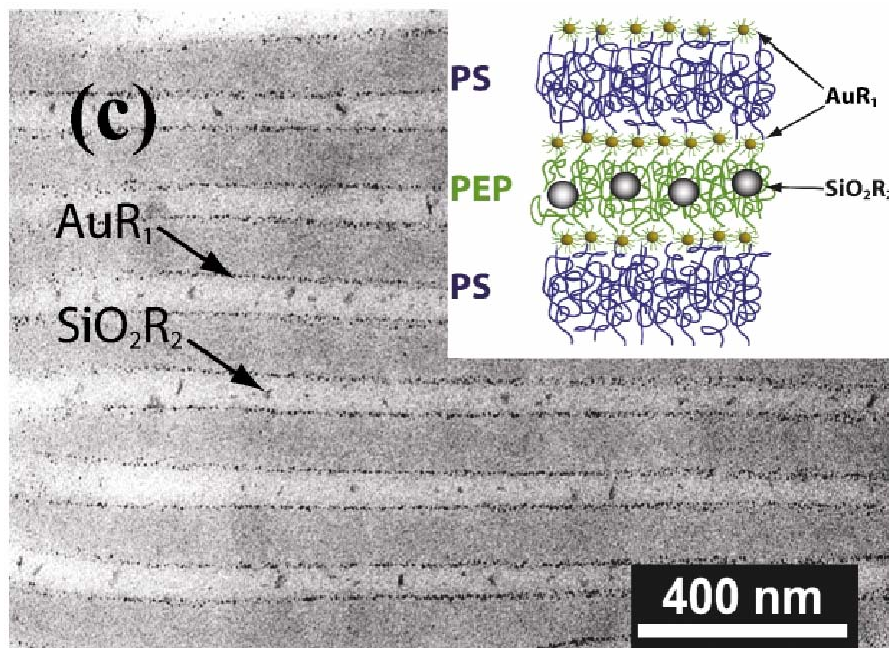
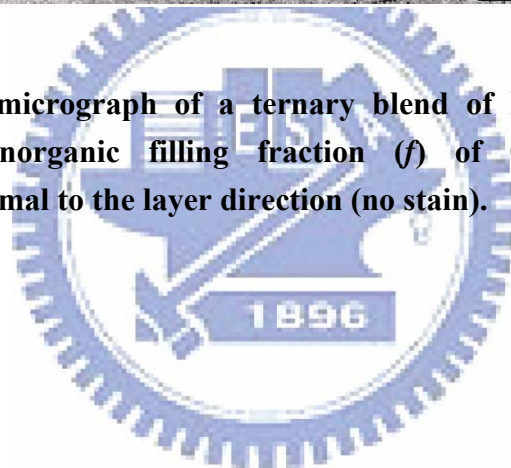


Figure 1-20. TEM micrograph of a ternary blend of PS-*b*-PEP, AuR_1 , and SiO_2R_2 with an inorganic filling fraction (f) of 0:02, recorded after micro-sectioning normal to the layer direction (no stain).



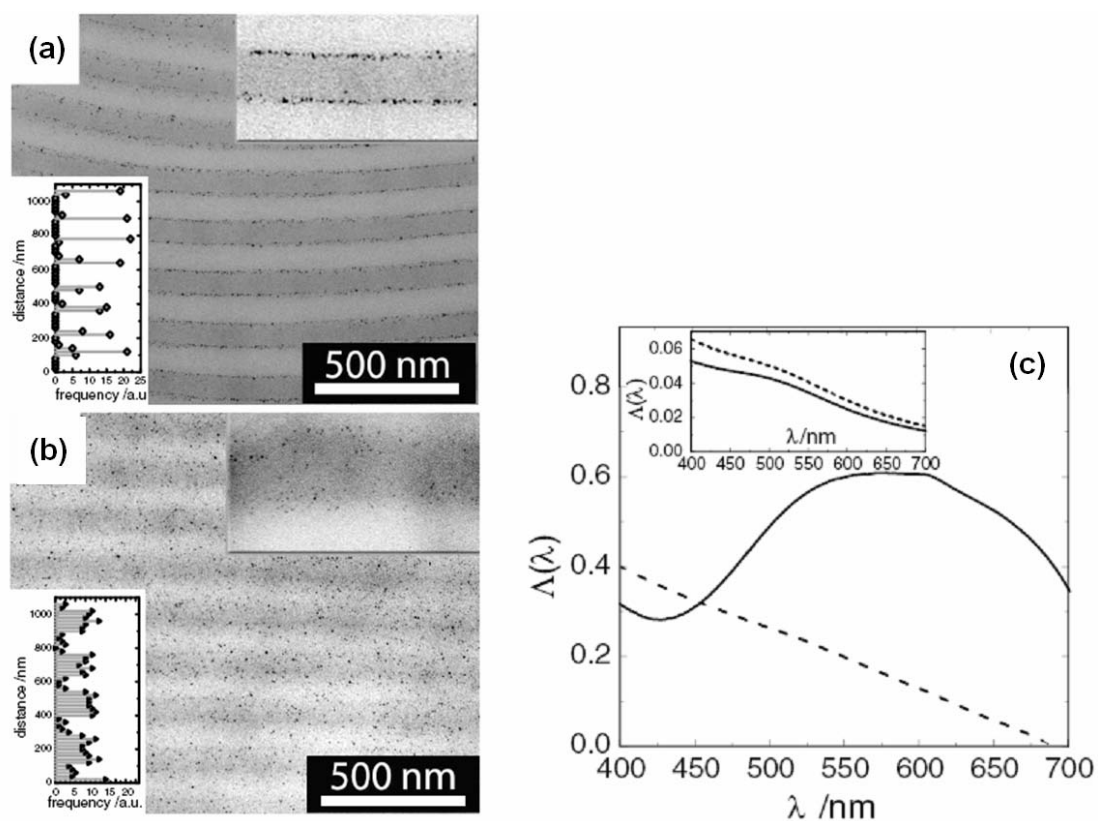


Figure 1-21. (a) TEM image of a PS-PEP/AuSC₁₂H₂₅ composite after micro-sectioning normal to the layer direction, revealing particle deposition at the PS-PEP interface and (b) TEM image of a PS-PEP/AuSPS composite. PEP domains appear as brighter regions in the micrograph. (c) Absorbance spectra of PS-PEP/Au composite materials possessing an interfacial segregated morphology (dotted line) and a selective-layer uniform morphology (continuous line). Inset: Absorbance spectra of dilute nanocrystal solutions [AuSC₁₂H₂₅ (dotted line) and AuSPS (continuous line)].^[93]

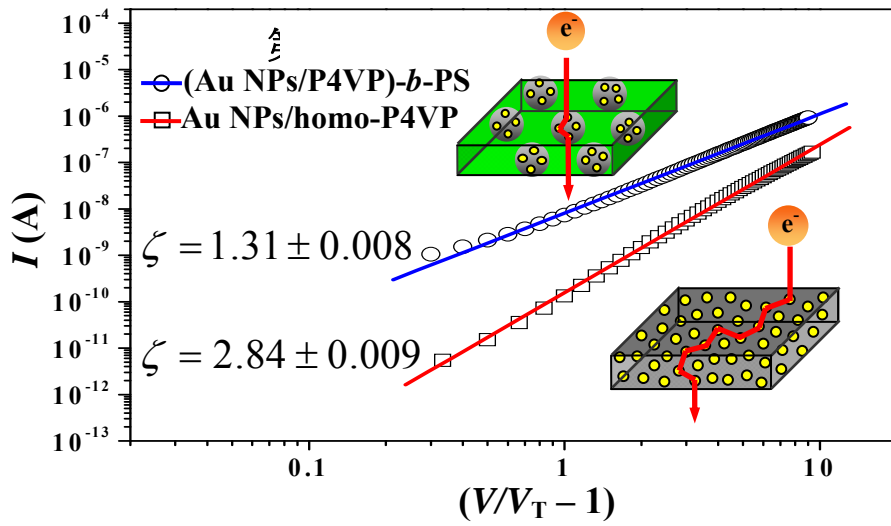
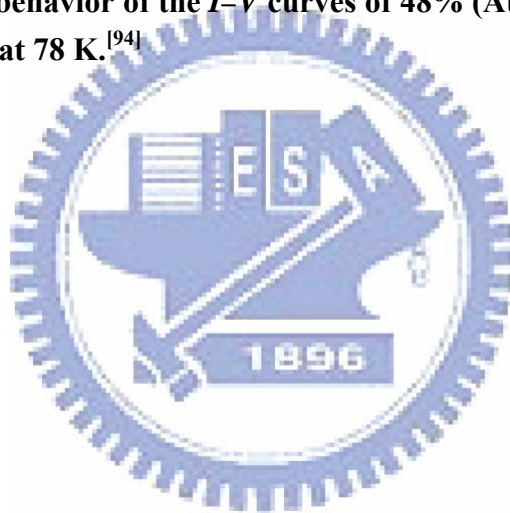


Figure 1-22. Scaling behavior of the I - V curves of 48% (Au NPs/P4VP)-*b*-PS and Au NPs/homo-P4VP at 78 K.^[94]



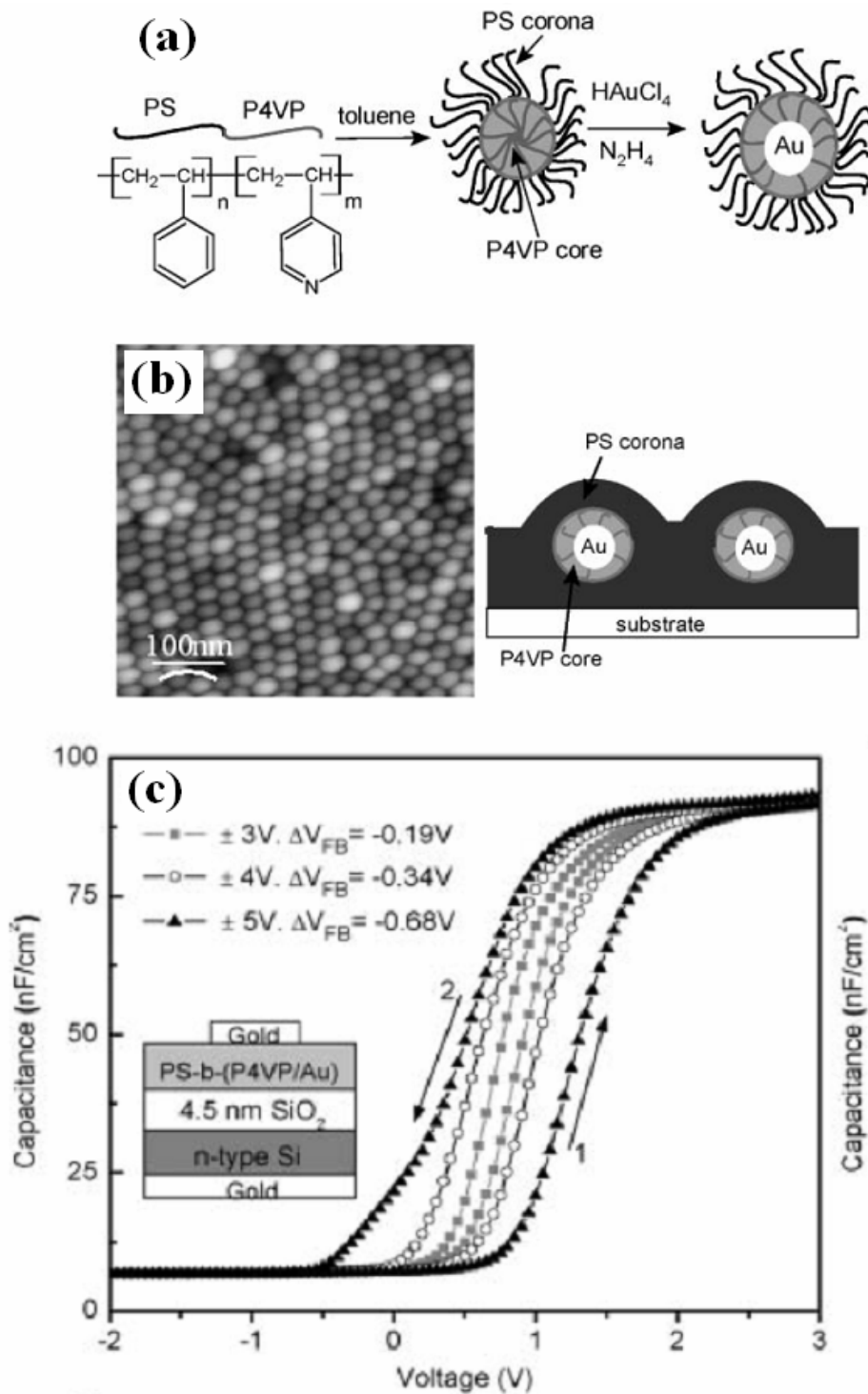


Figure 1-23. (a) Molecular structure of the PS-*b*-P4VP copolymer and a schematic representation of the micellation process with in situ synthesis of Au NPs in PS-*b*-P4VP. (b) AFM topographic image of the surface of a spin-coated PS-*b*-P4VP film along with a schematic illustration of a self-assembled PS-*b*-P4VP (with Au NPs) micellar film on a substrate. (c) Capacitance–voltage (C – V) measurements at 100 kHz on a metal–insulator–silicon structure with a PS-*b*-(P4VP/Au) film.

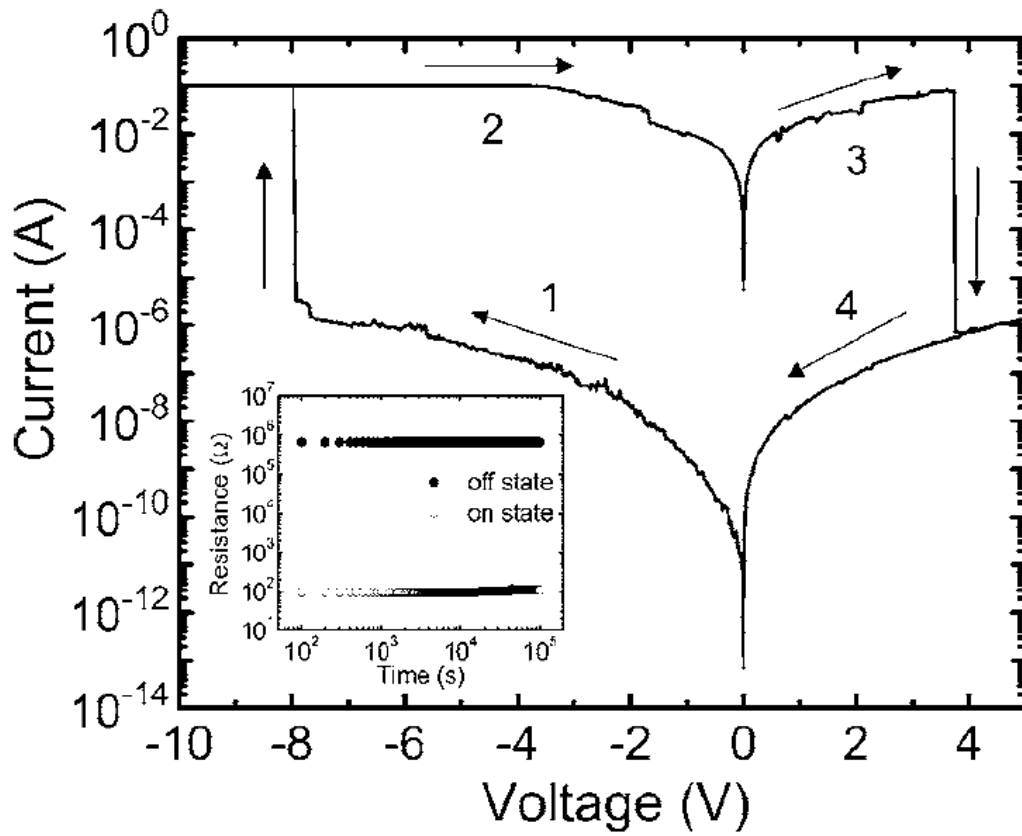


Figure 1-24. Typical I - V curves for PVK films. The inset presents the plot of ON- and OFF-state resistances after reading at 1 V per 100 s. The retention time of the ON and OFF states is more than a time period of 105 s for the PVK films. ^[115]

Chapter 2

Structural Evolution of Poly(styrene-*b*-4-vinylpyridine) Diblock Copolymer/Gold Nanoparticle Mixtures from Solution to Solid State

2-1 Introduction

Diblock copolymer/nanoparticle (NP) mixtures have attracted much attention recently because their dimensions are comparable; for example, diblock copolymers can have ordered structures with periodic thicknesses between 10 and 100 nm, while NPs having sizes between 1 and 10 nm have the most interesting optical, electrical, and magnetic properties.^[66-68, 122-125] Hence, using diblock copolymers as templates to control the spatial positions of NPs is a natural approach to producing hierarchically ordered structures for various applications.^[18, 80, 91, 126-128] In this regard, the location of NPs in block copolymers, which critically affects their resulting properties, has been the focus of a number of theoretical and experimental studies.^[71, 129-138] For instance, Balazs et al. used self-consistent-field and density functional theories to predict the locations of NPs; they found that NPs can reside either along the interface of two blocks or in the center of one particular block, depending on the ratio of the size of the NPs to the periodic thickness of the diblock copolymer.^[71, 130-133] Nevertheless, only a few experimental studies have confirmed Balazs' prediction.^[18, 134-138] To gain a fundamental understanding of the structures of the diblock copolymer/NP mixtures, we monitored the structural evolution of a particular systems poly(styrene-*b*-4-vinylpyridine)/gold NP(PS-*b*-P4VP/Au) assemblies from solution to the solid state to the solid state experiencing annealing. In this present study, we used small-angle X-ray scattering to follow the diffusion of hydrophobic Au NPs from continuous hydrophobic PS domains to the interfaces between the hydrophilic P4VP and hydrophobic PS. We also analyzed the hierarchical NP-filled shell structures that resulted from thermal annealing under vacuum. The structures of

the redissolved PS-*b*-P4VP_{Sph}/Au NP systems that had experienced annealing in the bulk were also examined.

2-2 Methods and Analysis

2-2-1 Materials. The spherical PS-*b*-P4VP diblock copolymer (volume fraction of P4VP domain: 0.12), having a molecular weight (*M_n*) of 557KPS/75KP4VP with a polydispersity index (*M_w*/*M_n*) of 1.07, was purchased from Polymer Source, Inc. Hydrogen tetrachloroaurate(III) trihydrate (HAuCl₄·3H₂O), tri-*n*-octylammonium bromide (TOAB, 99%), and sodium borohydride (NaBH₄, 99%) were obtained from Acros. 2-Phenylethanethiol (HSC₂Ph, 98%) was purchased from Aldrich. Toluene (99%), acetone (99%), dichloromethane (99%), and ethanol (99%) were purchased from TEDIA. Ultrapure deionized water was produced using a DirectQ3 system equipped with a pump from Millipore, Inc.

2-2-2 Synthesis of 2-Phenylethanethiolate-Coated and Pyridine-Coated Au NPs.

2-Phenylethanethiolate-coated Au NPs (AuSC₂Ph) were synthesized using the two-phase method described by Brust et al.^[139,140] A typical procedure for producing the AuSC₂Ph NPs is described as follows: An aqueous solution (3 mL) of HAuCl₄ (100 mg, 0.24 mmol) was mixed with a solution of tri-*n*-octylammonium bromide (332 mg, 0.60 mmol) in toluene (12 mL). The mixture was vigorously stirred until all of the HAuCl₄ had transferred into the organic layer. The organic phase was isolated when it had become dark brown in color. Subsequently, 2-phenylethanethiol (68 μL, 0.48 mmol) was added to the organic phase; after stirring for 20 min, the solution became colorless for a while. Next, a freshly prepared chilled aqueous solution (10 mL) of sodium borohydride (91 mg, 2.4 mmol) was added slowly with vigorous stirring over 30 min. Finally, after stirring for a further 24 h, the organic phase was separated, concentrated (rotary evaporator) to a volume of 1 mL, and then washed

three times with ethanol and acetone to remove any excess thiol or other agents. Before dissolving in toluene, the sample was dried under vacuum at room temperature for 3 h and then weighed. The inorganic content of AuSC₂Ph was 80%, as determined through the thermal gravimetric analyzer (TGA). Moreover, the pyridine-coated Au NPs (AuPy) prepared to study the case of NP distribution throughout the P4VP domain were synthesized using a previously described method,^[31,128] the volume loading of Au in the PS-*b*-P4VP_{Sph}/AuPy mixture was 1.4%.

2-2-3 Preparation of Block Copolymer/Au NP Mixtures

To study the edge-filled assembly, PS-*b*-P4VP/AuSC₂Ph was prepared as outlined in Scheme 2-1. PS-*b*-P4VP (30 mg) was added to toluene (1 mL). AuSC₂Ph NPs, having a volume fraction of Au of 1.4% in the PS-*b*-P4VP/AuSC₂Ph mixtures, were added to the micellar solution; to obtain a final solid concentration of 2 wt %, additional toluene was added. After stirring for 48 h, the toluene was evaporated slowly under vacuum at room temperature, and then the PS-*b*-P4VP/AuSC₂Ph solid film was dissolved in dichloromethane. The composites were mixed for 48 h and dried under a nitrogen flow until a saturated solution had formed. Subsequently, the mixtures were treated to a two-step annealing process involving annealing in saturated dichloromethane solution at 30 °C for 48 h, and drying slowly, followed by thermal annealing at 170 °C for 72 h to obtain the bulk PS-*b*-P4VP/AuSC₂Ph composites. The thin film PS-*b*-P4VP/AuSC₂Ph was formed from a dilute micellar solution (0.5 wt %) that was prepared by dissolving annealed PS-*b*-P4VP/AuSC₂Ph in toluene. The PS-*b*-P4VP/AuPy composite, in which Au NPs were confined in P4VP spheres, were prepared as described previously.^[31,128]

2-2-4 Characterization. Transmission electron microscopy was performed using a Hitachi H-600 instrument operated at 100 kV (for higher-contrast images) and a JEOL-2010 TEM operated at 200 kV (for higher-resolution and lattice images). For

TEM studies, ultrathin slices of the bulk films of the PS-*b*-P4VP/AuSC₂Ph mixtures were microtomed using a Leica Ultracut Uct apparatus equipped with a diamond knife and then deposited onto copper grids. In the case of thin films, a 0.5 wt % PS-*b*-P4VP/AuSC₂Ph composite solution was mixed in toluene for 3 days, dropped directly onto the carbon-coated copper grids, and dried of its additional solvent using absorbent paper.

Small-angle X-ray scattering (SAXS) measurements were performed at the SWAXS endstation of the BL17B3 beamline of the National Synchrotron Radiation Research Center (NSRRC). The flexible instrument was reported in details previously.^[141,142] With a 0.5 mm diameter beam of a wavelength λ of 1.24 Å and a sample-to-detector distance of 2.4 m, we collected SAXS data in the Q range from 0.006 to 0.25 Å⁻¹, which Q range covered the scattering characteristics of Au NP and the large Au-copolymer complex. Here the wave vector transfer $Q = 4\pi\sin(\theta/2)/\lambda$ was defined by the scattering angle θ and wavelength λ of X-rays. Sample solutions in toluene were sealed (airtight) in a cell with thin Kapton windows and a sample thickness of 5.2 mm. All the SAXS data collected with an area detector were corrected for sample transmission, background, and the detector sensitivity, and the Q value was calibrated by a commonly used silver behenate. For SAXS sample preparation, the bulk films were ca. 20 μm in thickness; the composite solution was mixed for 3 days with a solid content of 0.5 wt % in toluene.

X-ray photoelectron spectroscopy (XPS) experiments were performed using the wide-range spherical grating monochromator (WR-SGM) beamline at the BL24A1 beamline of the NSRRC and a mu-metal chamber equipped with a VG CLAM2 triple-channeltron energy analyzer (energy resolution was estimated to be better than 0.3 eV) and a sample transfer mechanism. The electron takeoff angle is 90°, and the incidence angle is 42°. All XPS samples that had been annealed and redissolved in

dichloromethane were prepared by spin-coating onto low-resistance ITO substrates (ca. $10 \Omega/\square$) followed by removal of the residual solvent under vacuum overnight.

2-3 Results and Discussions

Figure 2-1a displays the TEM micrograph of AuSC₂Ph NPs having a relatively uniform and narrow size distribution (diameter: 2.4 nm). Figure 2-1b indicates that the number-averaged particle diameter was 2.4 (± 0.1 nm, with a polydispersity of 15%, as deduced from the fitting of the SAXS data with a spherical form factor and a Schultz size distribution.^[90] The TEM and SAXS results correspond quite well. Because the ligands on the as-prepared AuSC₂Ph NPs were hydrophobic (i.e., then presented phenyl groups), the AuSC₂Ph NPs had more affinity to the PS block than to the P4VP block after the solvent being removed.

Figure 2-2 indicates that the SAXS curve of pure PS-*b*-P4VP_{Sph} in toluene can be fitted to a core/corona-like structure that consists of a P4VP domain as the core (diameter: 18 nm) and a PS domain as the corona (overall diameter: 36 nm). The polydispersity of the core/corona structure was 25%, due to the polydispersity of the molecular weight (PDI) 1.07) of PS-*b*-P4VP_{Sph}. The SAXS curve of the as-prepared mixture in toluene was approximated by the sum of the individual SAXS curves of PS-*b*-P4VP_{Sph} in toluene and AuSC₂Ph in toluene, indicating that there were no interactions (no interference scattering) between PS-*b*-P4VP_{Sph} and AuSC₂Ph in toluene, even after they had been mixed for 3 days. Presumably, AuSC₂Ph NPs prefer to stay in the toluene phase rather than adsorb to the PS corona or the P4VP core in the solution state.

Figure 2-3a displays the SAXS curves of the in situ annealed bulk PS-*b*-P4VP_{Sph}/AuSC₂Ph mixture that had previously experienced solvent annealing. The SAXS curves display two distinct changes: the absolute intensity underwent a

dramatic increase in the low- Q range (between 0.03 and 0.08 \AA^{-1}) and a large decrease in the high- Q range (ca. 0.18 \AA^{-1}). The increase of the scattering intensity can be divided into two stages: the early and later stages of the annealing process. In the early stage, the increase of intensity is attributed to the formation of stronger correlations between the Au NPs in the PS-*b*-P4VP. During this time, the Au NPs diffuse to the interfaces between the PS and P4VP, forming the Au NP-filled shell, which in turn results in a stronger scattering intensity and more-ordered scattering peaks (the scattering peaks appear in the Q range between 0.03 and 0.08 \AA^{-1}). It appears that the ordering of PS-*b*-P4VP_{Sph} improved after simply raising the temperature to 170 °C. Figure 2-3b indicates, however, that the annealed pure PS-*b*-P4VP_{Sph} displayed different oscillations and a low absolute scattering intensity after annealing for 72 h. The morphology of pure PS-*b*-P4VP_{Sph} bulk film was composed of disordered micelles because the scattering profile of the bulk film (Figure 2-3b), after scaled down in intensity, can overlap well with that for the micelles (Figure 2-2). From a comparison of the SAXS curves in Figure 2-3a, b, we deduce that the stronger oscillations of the mixture were dominated by the spatial distribution of Au NPs; namely, the coherent or constructive interference of the P4VP/Au complex contributes to the much higher intensity than that of the random dispersion or aggregation of Au NPs. In the second stage (annealing time: >1 h), the Au NPs appeared to accumulate in the interfacial area between the two blocks. A certain degree of overlapping or aggregation of the Au NPs occurred at PS/P4VP interfaces, which deteriorated the shell structure and the corresponding ordering of the peaks. Moreover, the scattering peak of the composite at a value of Q of ca. 0.18 \AA^{-1} suggests a liquidlike ordering of the Au NPs in the PS phase after the solvent had evaporated. It seems likely that, protected by their attached ligands (see the inset of Figure 2-3a), the Au NPs did not aggregate but instead packed into a liquidlike

ordering phase (possibly because of the nature of the ligand of the soft chains) with a mean spacing ($2\pi/Q$) of 3.5 nm, corresponding quite well to the diameter of the Au NPs (2.2 nm) plus twice the length of the 2-phenylethanethiol ligand ($2 \times 0.7 \text{ nm} = 1.4 \text{ nm}$). As a consequence, the correlated hierarchical structure increases the scattering intensity of the composite, at a cost of the phase-separated Au NP clusters (i.e., decreased intensity of the 0.18 \AA^{-1} peak). The peak of the Au NP clusters at 0.18 \AA^{-1} disappeared completely after 4 h of annealing and remained so even after increasing the annealing time, indicating that the structure transformation of the composite, closely associated with the Au NPs, did not change furthermore after the complete disruption of the Au NPs clusters in the first 4 h of the thermal annealing. Scheme 2-2 displays the schematic drawing of the structural evolution of PS-*b*-P4VP_{Sph}/AuSC₂Ph mixture during the thermal annealing. In Scheme 2-2, in the early stage of thermal annealing, the structure of the mixture is represented by Scheme 2-2a-c, whereas in the later stage, Scheme 2-2d stands for its structure.

In fact, the much higher scattering intensity in low- Q range after thermal annealing is a result of the complex formation of the copolymer and Au NPs. Namely, the formation of NP-filled complex or the adsorption of Au NPs to the copolymer. We also provided more evidence on the structural evolution of PS-*b*-P4VP_{Sph}/AuSC₂Ph mixture by using anomalous SAXS and TEM. Anomalous SAXS is used to discern the scattering contribution of Au NPs as shown in Figure 2-4.^[141] To identify the scattering peak at $Q \approx 0.18 \text{ \AA}^{-1}$, the anomalous SAXS result for the PS-*b*-P4VP_{Sph}/AuSC₂Ph film was displayed in Figure 2-4a before the thermal annealing. With the X-ray energy tuned closed to the L₃-absorption edge of Au (11.919 keV), the SAXS profile is expected to be sensitive only to the distribution of Au NPs in the composite film due to the resonant absorption. The two SAXS profiles in Figure 2-4a was obtained with 11.200 and 11.910 keV (away and near the

L_3 -absorption edge of Au) photons. The two profiles overlap well in the low- Q region (insensitive to the energy change, see also the inset), indicating that the high scattering intensity in this region does not involve Au NPs and should be mainly dominated by the P4VP spheres of the copolymer. On the other hand, in the high- Q region (see also the inset), the scattering peak at $Q = 0.18 \text{ \AA}^{-1}$ decreases obviously when the photon energy is changed from 11.200 to 11.910 keV. This result indicates clearly that the Au NPs, forming ordered clusters, are responsible for the ordering peak at $Q = 0.18 \text{ \AA}^{-1}$. Furthermore, the overall scattering SAXS profile for the mixture film after thermal annealing in Figure 2-4b is sensitive to the beam energy close to the L_3 -edge absorption of Au. This illustrates that the overall scattering profile including the low- Q region dominated by the pure PS-*b*-P4VP_{Sph} before thermal annealing closely associates with Au NPs after the thermal annealing. From anomalous SAXS data of PS-*b*-P4VP_{Sph}/AuSC₂Ph mixtures before and after thermal annealing, it is clear that Au NPs adsorb to the PS/P4VP interface only after thermal annealing.

Figure 2-5 shows TEM images of PS-*b*-P4VP_{Sph}/AuSC₂Ph mixtures before and after thermal annealing. Figure 2-5a displays TEM image of the as-prepared PS-*b*-P4VP_{Sph}/AuSC₂Ph mixture. We can observe few Au NP clusters, which agree with the in situ SAXS result in Figure 2-3a and the drawing in Scheme 2-2a. Figure 2-5b displays the TEM image of PS-*b*-P4VP_{Sph}/AuSC₂Ph mixture that experienced the two-step solvent and thermal annealing. Because of the slice thickness of the bulk spherical diblock copolymer, overlapped spheres are visible in this TEM image. In the inset in Figure 2-5b, an HR-TEM cross-sectional image of a single P4VP/AuSC₂Ph core-shell sphere, we observe the formation of an Au NP-filled shell, quite consistent with the SAXS results of the in situ bulk thermal annealing. Hence, the evidence from these TEM images supports the conclusion from in situ SAXS results. From all the evidence mentioned above, we are confident on the conclusion given in Scheme 2-2

for the structural evolution of PS-*b*-P4VP_{Sph}/AuSC₂Ph mixtures during thermal annealing process.

Since the thermal annealing process will result in a loss of thiol ligands on the surface of Au NPs, we quantified the loss of 2-phenylethanethiol by TGA. Figure 2-6a shows the weight loss curve of the PS-*b*-P4VP_{Sph}/AuSC₂Ph during the thermal annealing. The additional weight loss of the PS-*b*-P4VP_{Sph}/ AuSC₂Ph mixture between before and after thermal annealing is 1.2 wt % at 230 °C (2-phenylethanethiol ligands of AuSC₂Ph will evaporate off at 230 °C), which is equal to a 68.6% loss of 2-phenylethanethiol ligands (1.75 wt %, initially). The partial loss of the hydrophobic thiol ligands on Au NPs' surfaces was compensated by having been surrounded by the pyridine groups of P4VP chains when Au NPs diffused to the PS/P4VP interface. To monitor the weight loss of thiol ligands, the PS-*b*-P4VP/AuSC₂Ph mixture was annealed in TGA furnace at 170 °C under a N₂ atmosphere. Figure 2-6b shows the weight loss vs. the annealing time with a deep loss of thiol ligands in the first hour of thermal annealing. The weight loss of 0.7 wt % of the composite corresponds to a 40% loss of the thiol ligands. The TGA results provide the evidence that some of the 2-phenylethanethiol ligands have evaporated during the thermal annealing, leading to a decrease in the hydrophobicity and the thiol grafting density of AuSC₂Ph NPs.

Figure 2-7 displays the results of SAXS for the annealed PS-*b*-P4VP_{Sph}/Au NP mixture redissolved in toluene. In Figure 2-7a, the SAXS curve for the solution of PS-*b*-P4VP_{Sph}/AuSC₂Ph exhibits stronger oscillation characteristics, reflecting a higher hierarchical structural order for the mixture, than that for pure PS-*b*-P4VP_{Sph}, in toluene solution. The higher electron density at the interface can be used to fit the curves (dashed curve), implying that the Au NPs reside at the interface between the PS and P4VP blocks. Additionally, the Au NPs remained well dispersed at the

interface, as evidenced from the high- Q region of the same transition feature, which is the same as that of the pure Au NPs having a diameter of 2.2 nm. In contrast, in the case of the PS-*b*-P4VP_{Sph}/AuPy solution,^[31,128] the SAXS scattering characteristics revealed that the Au NPs were incorporated within the P4VP domain, forming aggregates having an average diameter of 5 nm. In Figure 2-7b, the three plots of the $\ln I(Q)$ vs. Q^2 data were fitted using the corresponding Guinier approximations (dashed lines) in the low- Q range of 0.006-0.012 \AA^{-1} , as represented by Eq. 2-1:

$$I(Q) = I(0) \exp\left(-\frac{Q^2 R_g^2}{3}\right) \quad (2-1)$$

where R_g is the radius of gyration of the diblock copolymer in solution and can be extracted from the slopes ($-R_g^{2/3}$) of the fitted lines in Figure 2-7b. The values of R_g for the PS-*b*-P4VP_{Sph}, PS-*b*-P4VP_{Sph}/AuSC₂Ph, and PS-*b*-P4VP_{Sph}/AuPy systems were 148±5, 152±3, and 173±5 \AA , respectively. Thus, when the Au NPs were incorporated within the P4VP domains, the global size of the composite increased to 173 from 148 \AA for the pure PS-*b*-P4VP_{Sph}. This result can be understood by considering the fact that the P4VP chains are tangled with Au NPs and, therefore, are stretched to accommodate neighboring Au NPs. In contrast, when the Au NPs were bound at the interface between the PS and P4VP blocks, the global size was virtually identical to that of the pure block copolymer. Presumably, the Au NPs at the interface of the PS and P4VP blocks reside in the corona-like chains of PS, which remained in an extended state in toluene, a favorable solvent for PS. Therefore, the PS-*b*-P4VP_{Sph}/AuSC₂Ph system formed a core/shell/corona (P4VP/Au/PS) micellar structure.

Figure 2-8 displays TEM images of a PS-*b*-P4VP_{Sph}/AuSC₂Ph thin film that had been cast from the solution of two-step annealed PS-*b*-P4VP_{Sph}/AuSC₂Ph mixture in toluene. In Figure 2-8a, it is notable that the NP-filled shell nanopatterns remained

despite the fact that they have undergone the recasting. Moreover, the TEM image of a single P4VP/AuSC₂Ph core/shell structure in Figure 2-8b indicates less deformed P4VP spheres than that in the case of the bulk sample (Figure 2-5b); this result is probably due to the fact that the shear strain of the bulk from microtoming was released in the solution. On the basis of the volume fractions and diameters of the Au NP and P4VP spheres, we calculate that there were ca. 66 Au NPs locating at the interface of PS/P4VP domains (see Appendix 1 for the calculating details), which amounts to a covered surface area of 24.7% for each P4VP sphere of the Au particle-filled nanoshell assembly; this result agrees quite well with the TEM observations in Figure 2-8b (ca. 60-80 Au NPs surrounding each P4VP sphere).

Overall, the irreversible structure after annealing and the stable nanoshell arrangement of Au NPs in bulk state and the redissolved micellar solution state imply that an additional chemical affinity may be generated between the 2-phenylethanethiol-coated Au NPs and the P4VP block in the thermal annealing process.

Figure 2-9 presents scanning XPS spectra of the pure P4VP, the annealed P4VP/AuSC₂Ph composites, the annealed lamellar PS-*b*-P4VP/AuSC₂Ph composites, and the as-prepared AuSC₂Ph NPs. We attribute the peaks at 400, 286, 164, 153, 103, 88, and 84 eV to the N 1s (P4VP), C 1s, S 2p_{3/2} (2-phenylethanethiol), Si 2s, Si 2p_{3/2} (ITO), Au 4f_{7/2}, and Au 4f_{5/2} (Au NPs) energy levels, respectively. Figure 2-10 displays the N 1s high-resolution XPS spectra of the pure P4VP, the annealed P4VP/AuSC₂Ph composite, and the annealed lamellar PS-*b*-P4VP/AuSC₂Ph composite. The N 1s signal of the pure P4VP presented a peak at 399.3 eV; the annealed P4VP/AuSC₂Ph and lamellar PS-*b*-P4VP/AuSC₂Ph composites exhibited higher binding energies, with their peaks at 400.1 and 399.8 eV, respectively. This slight increase is indicative of the interaction between the pyridine groups and the

metallic Au NP surfaces. In fact, in the similar case of a poly(2-vinylpyridine)/Au NP system,^[135,144] Shull et al. reported evidence for a strong Au-pyridine interaction by measuring a low contact angle (9°) between the Au and poly(2-vinylpyridine) surfaces. As a result, we surmise that the thermal annealing process caused the loss of the 2-phenylethanethiol ligands on the Au NP surfaces, resulting in enthalpic adsorption between the Au surfaces and the pyridine groups.

In addition to the entropic effect, the extra strong favorable interaction between P4VP or PS and Au NP surfaces determines the Au NPs location. Here, we only show the latter term quantitatively. The presence of stable NP-filled assemblies both in the bulk and in micellar solution can be partly explained by the interfacial adsorption energy of the NPs when they are located at the interface of the two phases. The adsorption energy (E_a) of an Au NP at the interface of PS-*b*-P4VP_{Sph} in our experiments can be described using the following Eq. 2-2:^[134,143]

$$E_a = \pi r^2 \gamma_{PS/P4VP} \times [1 - |\cos \theta|]^2 \quad (2-2)$$

where $\cos \theta$ can be written as Eq. 2-3:

$$\cos \theta = \frac{\gamma_{Au/PS} - \gamma_{Au/P4VP}}{\gamma_{PS/P4VP}} \quad (2-3)$$

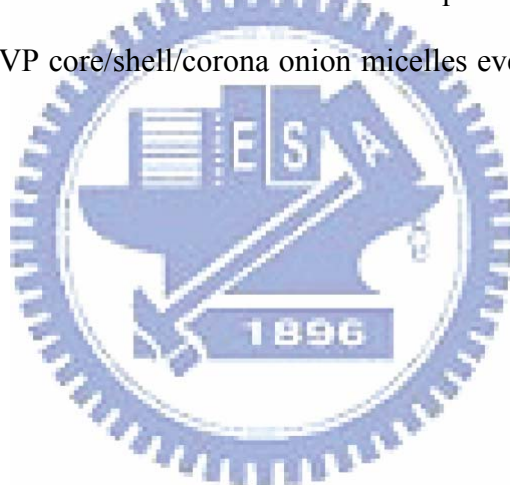
where r is the radius of AuSC₂Ph and $\gamma_{PS/P4VP}$, $\gamma_{Au/P4VP}$, and $\gamma_{Au/PS}$ are the interfacial energies of the PS-P4VP diblock, the AuSC₂Ph-PS, and AuSC₂Ph-P4VP systems, respectively. In the annealed samples, the loss of phenylethanethiolate ligands (PS affinity surfaces) generated bare Au surfaces (P4VP affinity surfaces), leading to amphiphilic surfaces on the Au NPs. This situation will result in a slight difference between $\gamma_{Au/P4VP}$ and $\gamma_{Au/PS}$, approximated as zero for $\cos \theta$, giving a value of E_a of ca. $\pi r^2 \gamma_{PS/P4VP}$ for an Au NP. Consequently, the adsorption energy contributed by the favorable interaction between P4VP and Au NPs may yield a driving interfacial assembly of NPs, not accounting for entropic considerations. Additionally, in the

liquid phase, a recent report described the formation of macroscale NP-filled hollow spherical shells at liquid-liquid (toluene-water) interfaces.^[145] In the case of our micellar solution, the P4VP-Au-PS core/shell/corona micellar solution in toluene would be stabilized as a result of the strong interactions ($Ea = ca. \pi r^2 \gamma_{PS/P4VP}$) between Au and vinylpyridine, despite the fact that $\gamma_{Au/PS}$ replaces $\gamma_{Au/toluene}$. Therefore, the interfacial adsorption energy plays an important role on stabilizing the Au NP-filled assemblies in the micellar solution status.

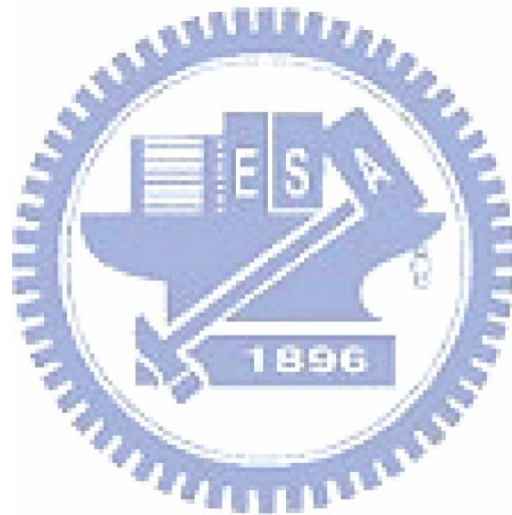
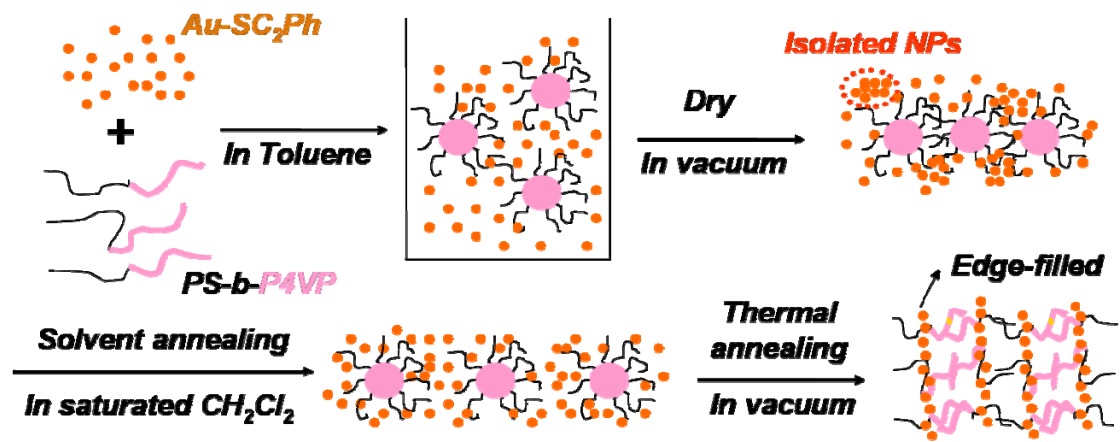
We have shown that the location of the Au NPs can be altered by the evaporation of 2-phenylethanethiol ligands, which has a similar but short chemical structure to PS oligomer, during the thermal annealing process. In a related study, Kim et al. also demonstrated a similar mechanism to control the location of thiol-terminated PS or P2VP-coated Au NPs in a lamellar phase of P2-*b*-P2VP by directly synthesizing different grafting densities of thiol-terminated homopolymer on Au NPs.^[135] For example, high area chain density (>1.6 chains/nm²) of PS-coated Au NPs can locate in the PS domain, whereas low area chain density ones (<1.3 chains/nm²) can be incorporated into the PS/P2VP interface. In our case, we chose 2-phenylethanethiol as the ligand to fully cover the Au NPs, and we can obtain AuSC₂Ph NPs with a narrow size distribution of 15% and a good dispersion of the NPs in toluene solution. Owing to the small molecular ligands, the ligand cover density (or the location) of the Au NPs we used could be changed by the thermal annealing process, and the partial grafting Au NPs could stably embedded into the copolymer. Both systems are very similar in that the location of NPs can be influenced greatly by the chemical structure and the grafting density of the ligands on the NP surfaces via simple synthesis or annealing methods.

2-4 Conclusions

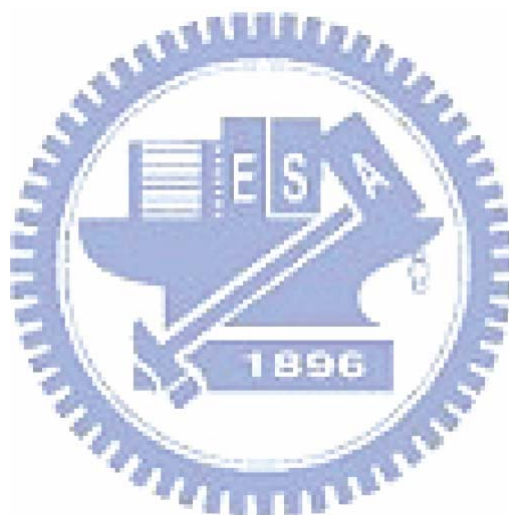
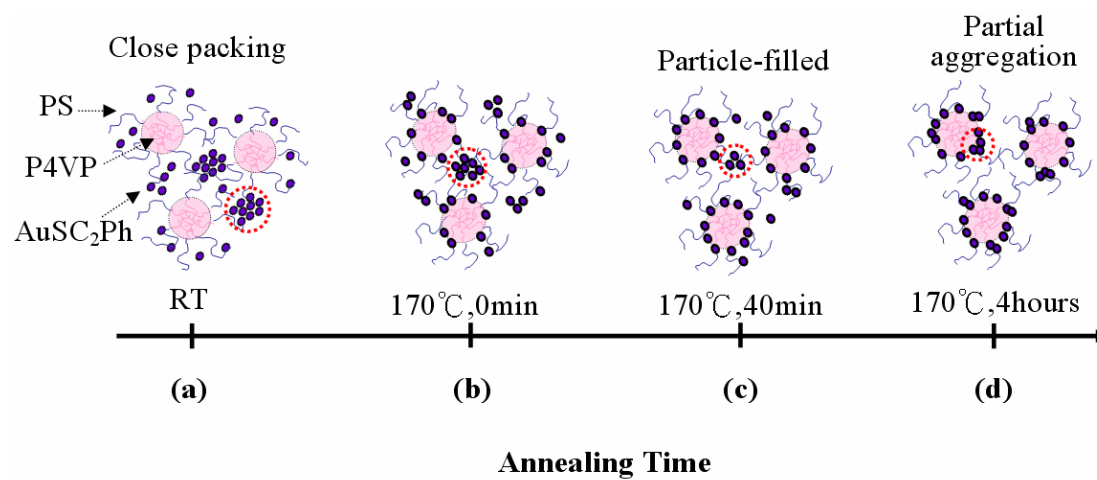
We have monitored the structural evolution of spherical PS-*b*-P4VP/AuSC₂Ph NP mixtures in the solid state during thermal annealing. We found that the Au NPs that existed in a random state with some cluster packing in the PS domain diffused to the interface of the amphiphilic PS-*b*-P4VP diblock copolymer within 4 h at 170 °C under vacuum to form NP-filled shell-like assemblies. We speculate that this interfacial activity of AuSC₂Ph results most from the fact that the initially hydrophobic Au NP surfaces became more hydrophilic after ~70% of the 2-phenylethanethiol ligands had evaporated off. The Au NP-filled assemblies located at the interface between the PS and P4VP blocks were quite stable; they remained in the form of PS-Au-P4VP core/shell/corona onion micelles even after redissolving the samples in toluene.



Scheme 2-1. Fabrication of the Self-Assembled PS-*b*-P4VP/AuSC₂Ph Bulk Film.



Scheme 2-2. Schematic Representation of the Structural Evolution of the PS-*b*-P4VP_{Sph}/ AuSC₂Ph Mixture at Various Annealing Times.



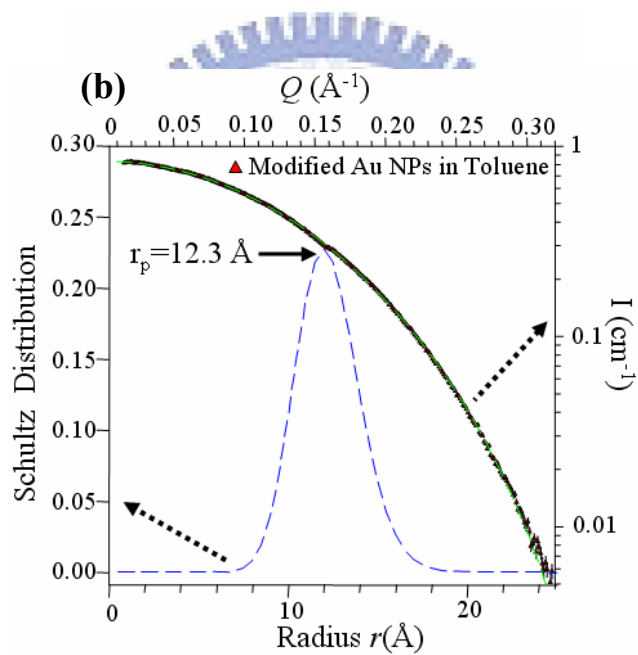
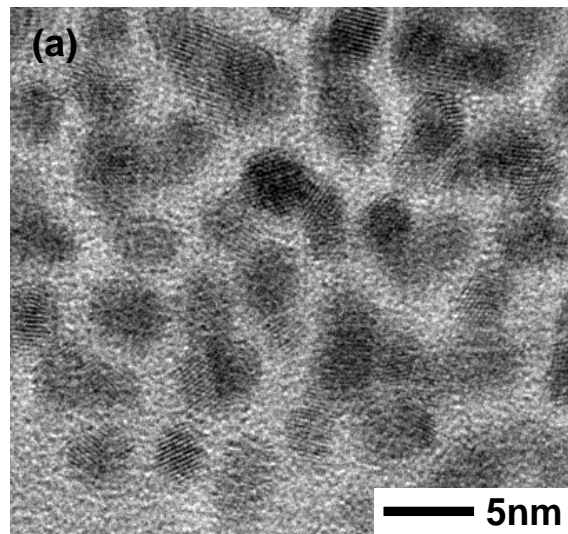


Figure 2-1. (a) HR-TEM image of AuSC₂Ph cast from a toluene solution. (b) The SAXS profile measured for the 0.5 wt % AuSC₂Ph NPs in toluene is fitted (dashed curve) using polydisperse spheres of the Schultz distribution (in radius r) shown.

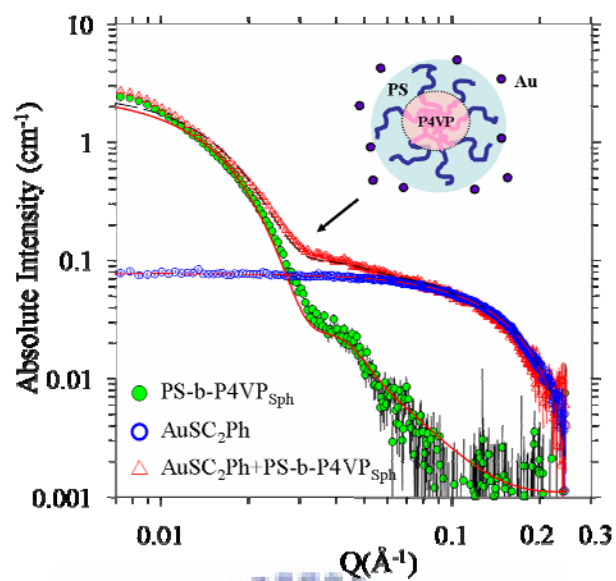
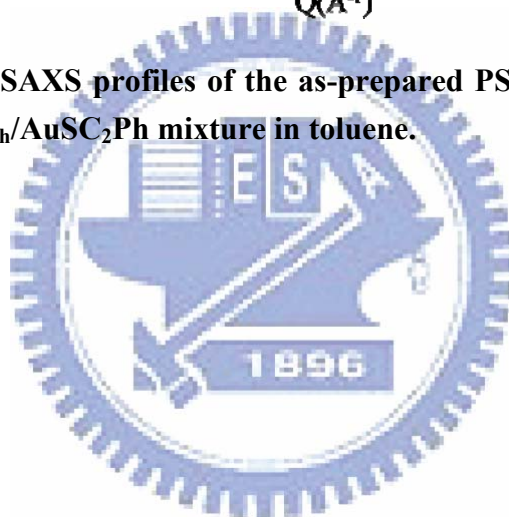


Figure 2-2. Solution SAXS profiles of the as-prepared PS-*b*-P4VP_{Sph}, AuSC₂Ph, and the PS-*b*-P4VP_{Sph}/AuSC₂Ph mixture in toluene.



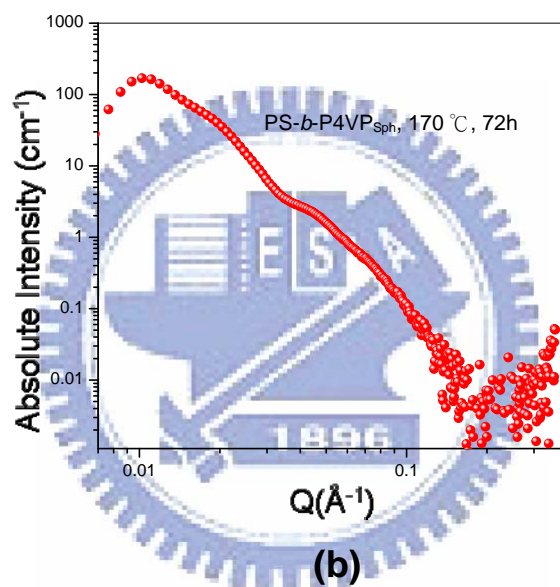
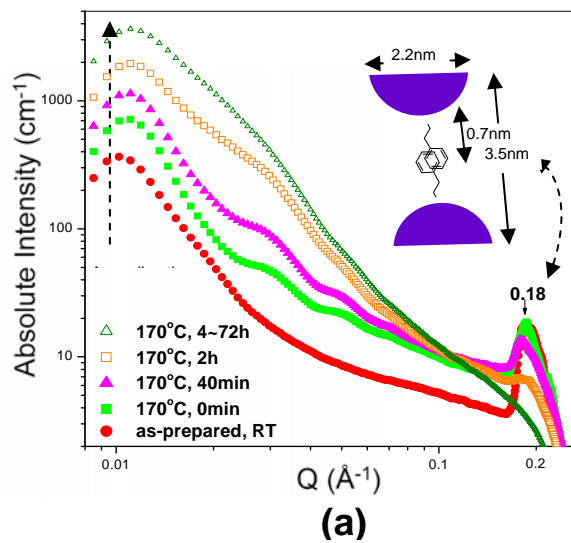


Figure 2-3. (a) In situ thermal annealing SAXS profiles of the as-prepared PS-*b*-P4VP_{Sph}/AuSC₂Ph mixture. (b) The SAXS profile of the annealed PS-*b*-P4VP_{Sph}.

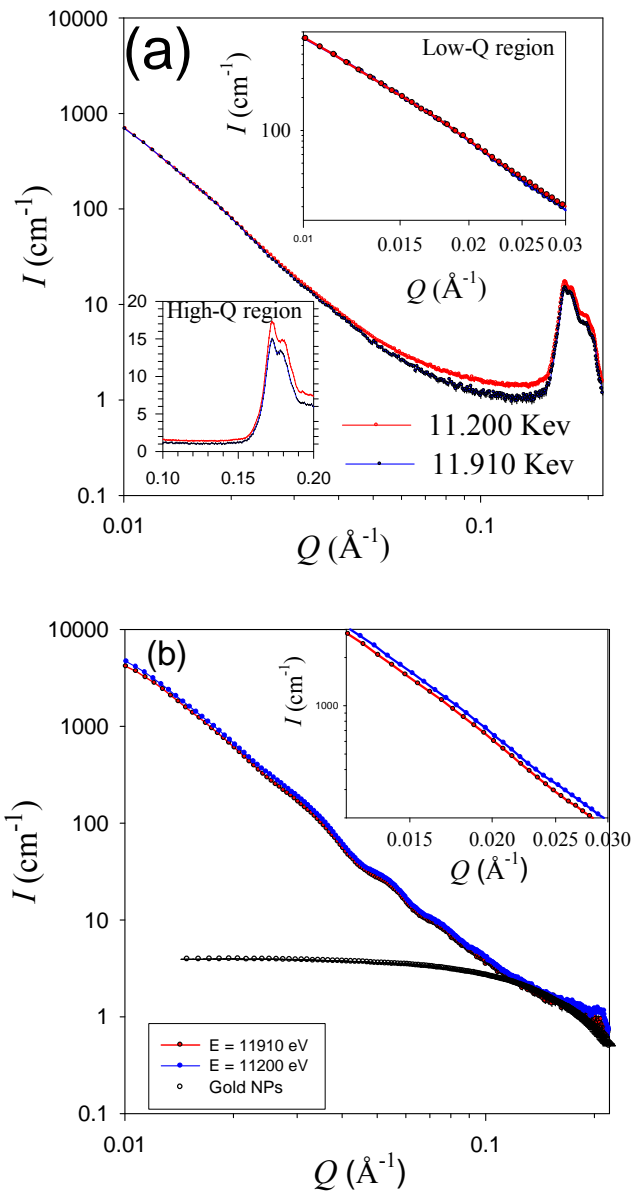


Figure 2-4 (a) Anomalous SAXS data for the PS-*b*-P4VP_{Sph}/AuSC₂Ph film before the thermal annealing, and (b) Anomalous SAXS data for the thermal annealed PS-*b*-P4VP_{Sph}/AuSC₂Ph film at two beam energies of 11.910 and 11.200 keV (near L₃-edge absorption of Au).

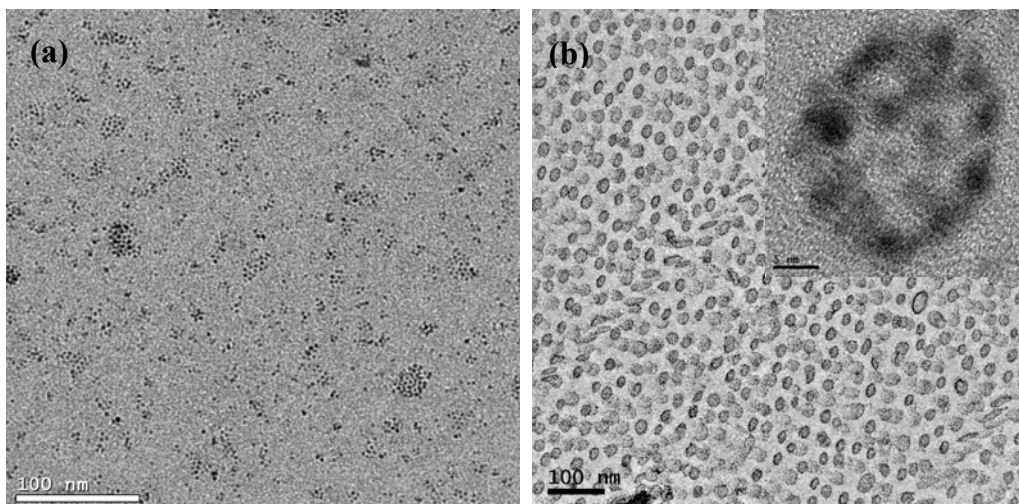
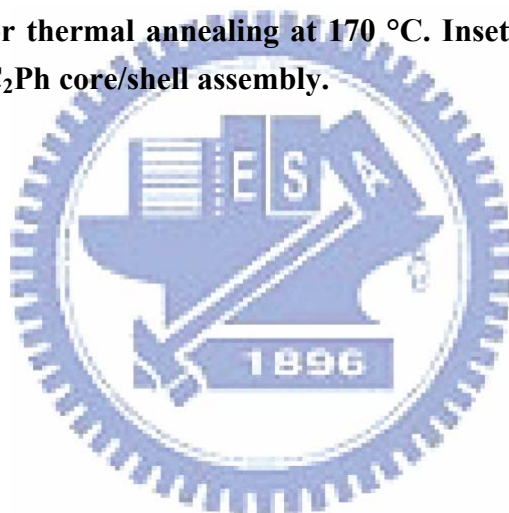
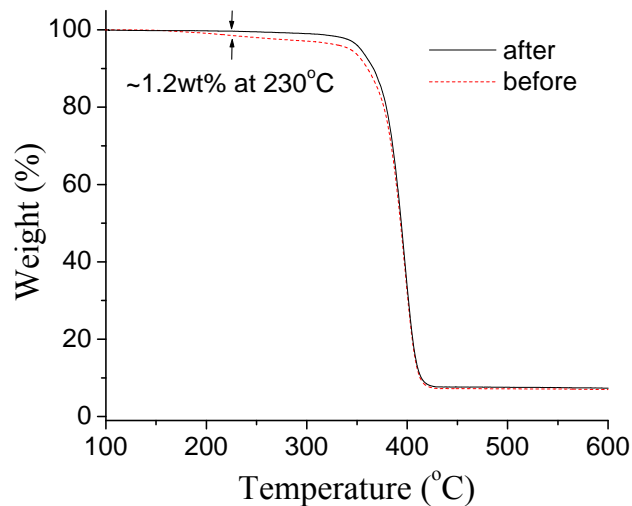
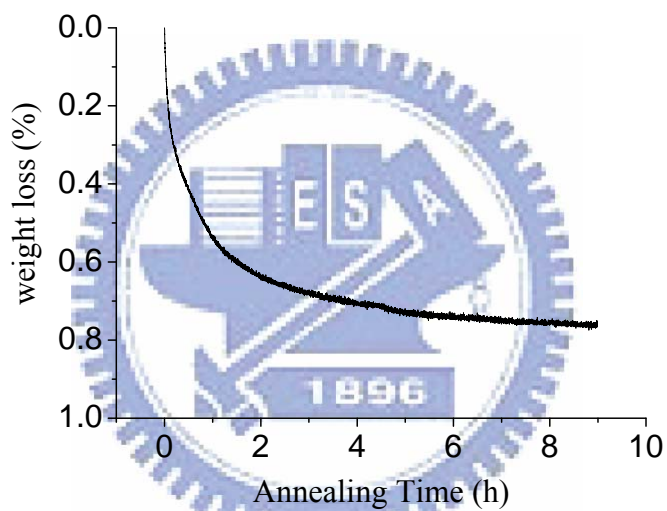


Figure 2-5. (a) TEM image for the as-prepared PS-*b*-P4VP_{Sph}/AuSC₂Ph mixture, with abundant NP clusters. (b) TEM micrograph of the PS-*b*-P4VP_{Sph}/AuSC₂Ph mixture that had been subjected to two-step annealing, 48 h of solvent annealing at 30 °C and 72 h for thermal annealing at 170 °C. Inset: HR-TEM image of a single P4VP_{Sph}/AuSC₂Ph core/shell assembly.





(a)



(b)

Figure 2-6. (a) The TGA result of the PS-*b*-P4VP_{Sph}/AuSC₂Ph mixture before and after 72 h thermal annealing at 170 °C under vacuum. (b) The weight loss (%) vs. the annealing time of the PS-*b*-P4VP_{Sph}/AuSC₂Ph mixture during the 170 °C isothermal annealing under a N₂ atmosphere.

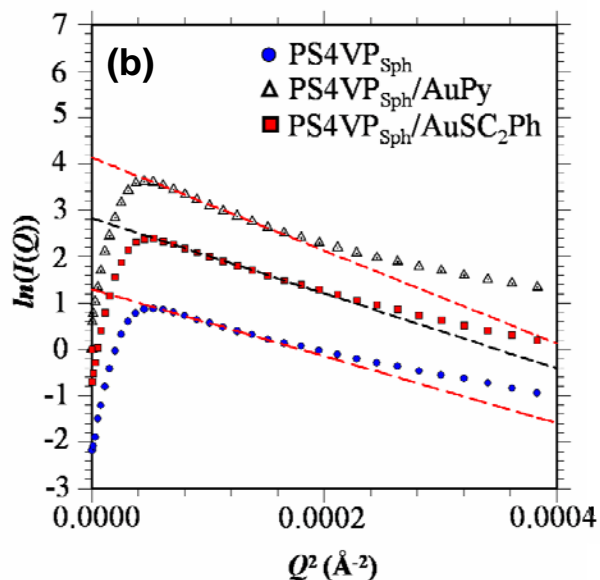
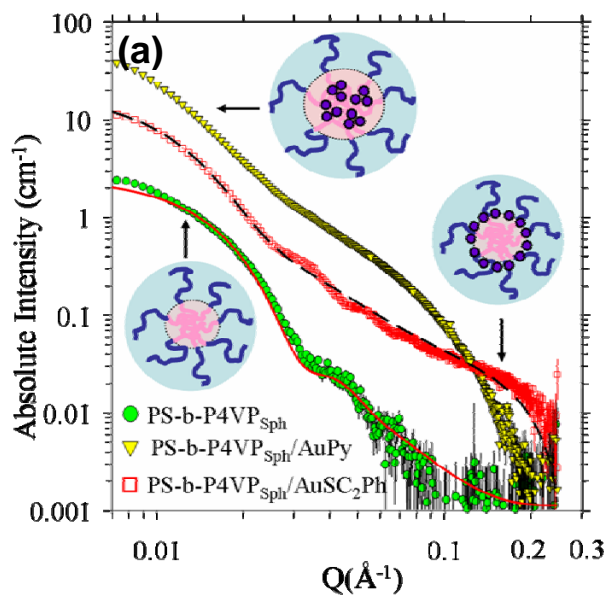


Figure 2-7. (a) Solution state SAXS profiles of the PS-*b*-P4VP_{Sph}, PS-*b*-P4VP_{Sph}/AuPy, and PS-*b*-P4VP_{Sph}/AuSC₂Ph systems after they had been subjected to annealing and redissolving in toluene. All schematic micellar structures of PS-*b*-P4VP_{Sph}-Au NP mixtures appear near the corresponding curves. (b) Three corresponding profiles fitted using the Guinier approximation.

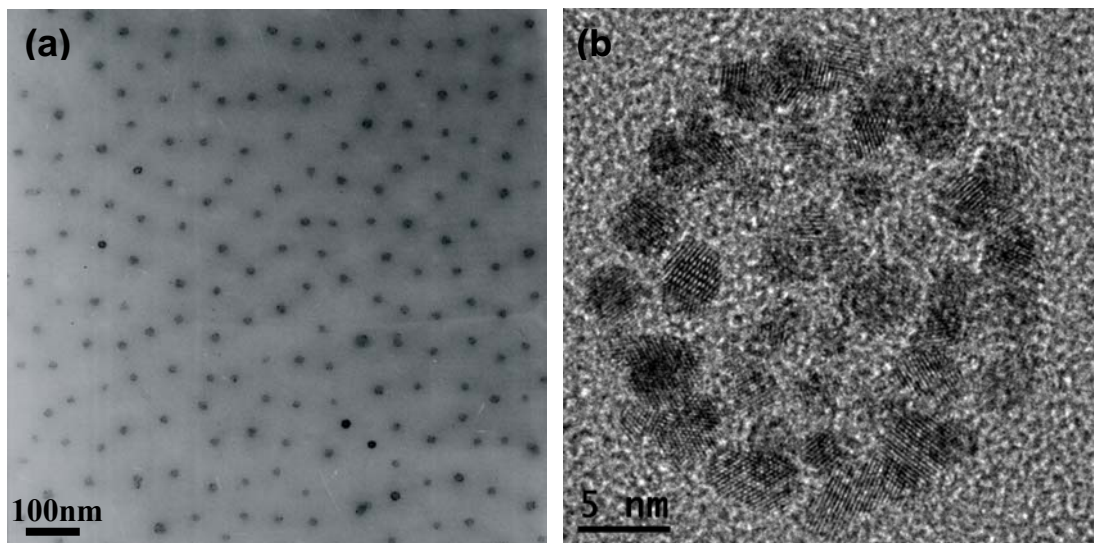
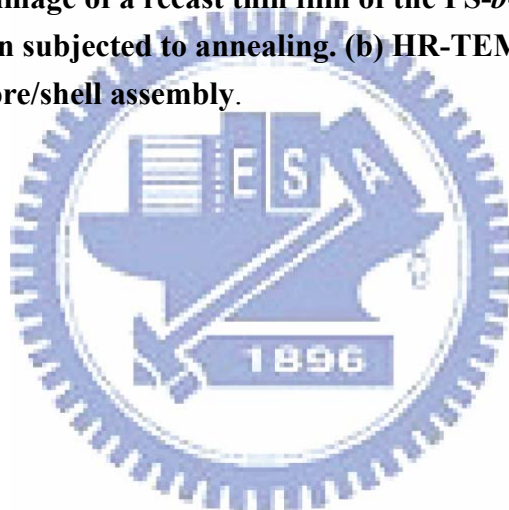


Figure 2-8. (a) TEM image of a recast thin film of the PS-*b*-P4VP_{Sph}/AuSC₂Ph mixture that had been subjected to annealing. (b) HR-TEM image of a single P4VP_{Sph}/AuSC₂Ph core/shell assembly.



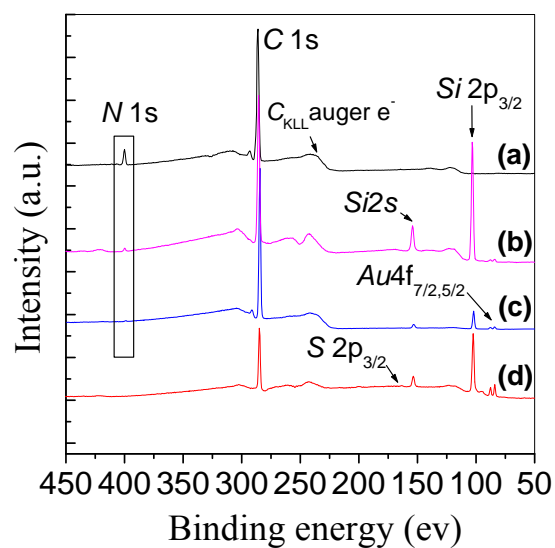
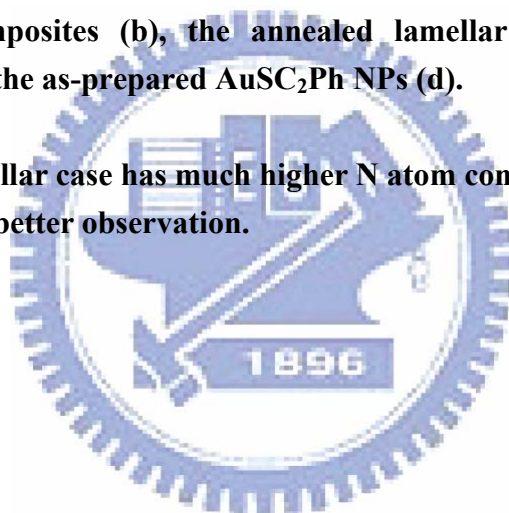


Figure 2-9. Survey scanning XPS spectra of the pure P4VP (a), the annealed P4VP/AuSC₂Ph composites (b), the annealed lamellar PS-*b*-P4VP/AuSC₂Ph composites (c),^a and the as-prepared AuSC₂Ph NPs (d).

^aThe edge-filled lamellar case has much higher N atom concentration (5 times for spherical case) for a better observation.



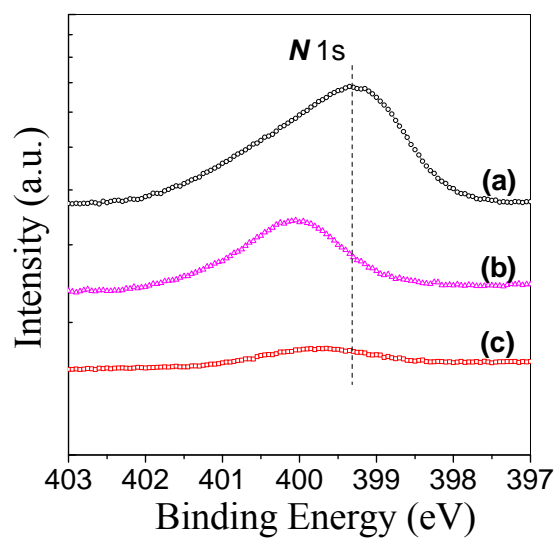
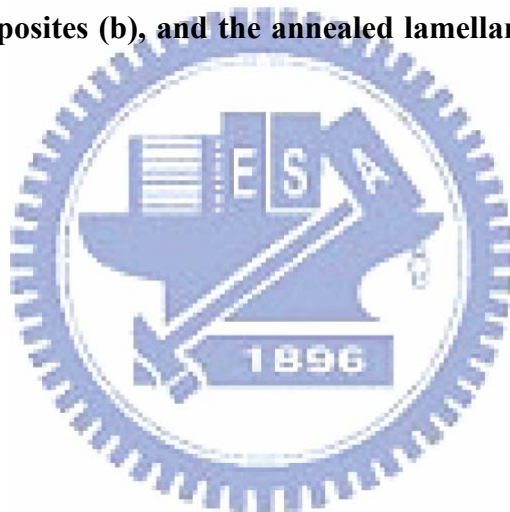


Figure 2-10. N 1s XPS spectra of the pure P4VP (a), the annealed P4VP/AuSC₂Ph composites (b), and the annealed lamellar PS-*b*-P4VP/AuSC₂Ph composites (c).



Chapter 3

Pseudo-Single-Crystalline Self-Assembled Structure Formed from Hydrophilic CdSe and Hydrophobic Au Nanoparticles in the Poly(4-vinylpyridine) and Polystyrene Blocks, Respectively, of a Poly(styrene-*b*-4-vinylpyridine) Diblock Copolymer

3-1 Introduction

The composites formed from diblock copolymers and NPs have attracted much attention recently because their dimensions are comparable and their applications are versatile.^[45, 66, 68, 122] For instance, diblock copolymers can have ordered structures with periodic thicknesses ranging between 10 and 100 nm,^[147, 148] while NPs having sizes between 1 and 10 nm have the most interesting optical, electrical, and magnetic properties.^[58] Hence, using diblock copolymers as templates to control the spatial locations of NPs is a natural approach to producing hierarchically ordered structures for various applications.^[123-125, 149, 150] In block copolymers, the location of NPs, which critically affects their resulting properties, has been the focus of a number of theoretical and experimental studies.^[90-92, 127, 130-134, 151, 152] For example, using self-consistent field and density functional theories, NPs have been predicted to decorate the interface of two blocks or be positioned in the center of one particular block, depending on the ratio between the size of the NPs and the periodic thickness of the diblock copolymer.^[71] Experimentally, controlling the spatial distributions of NPs in specific domains of block copolymers can be achieved *in situ*^[127] or *ex situ*,^[43, 44] using external fields,^[31] or directed chemical-binding methods.^[88b]

The embedding of NPs into a copolymer matrix, however, often occurs with NP-induced morphological transformations in diblock copolymers.^[38, 90, 91, 151] For instance, simple cubic structures of PS-*b*-PEO)/CdS NPs composites were obtained when using an originally hexagonally packed cylindrical structure of PS-*b*-PEO.^[38]

Similarly, the morphological change of the PS-*b*-P4VP/CdS composite from the hexagonally packed P4VP cylinders into a lamellar structure was induced by the formation of hydrogen bonds between CdS NPs and the P4VP domains.^[90] Moreover, NP-induced phase transformation resulting from the choice of solvent or the depth of the bulk film are also critical factors affecting the particle–concentration gradient along the film depth.^[91] Most studies into the ordered morphologies formed from diblock copolymer/NP composites involve only one type of NP; indeed, we are aware of only two reports concerning the formation of ordered structures from two different kinds of NPs and a diblock copolymer: the self-assembly of ex situ-synthesized Au NPs and in situ-synthesized iron oxide NPs on a monolayer film of PS-*b*-P4VP micelles^[80] and the self-assembly of small Au NPs and large Si NPs, both coated with alkyl ligands, along the interface and within the poly(ethylene propylene) core, respectively, of a poly(styrene-*b*-ethylene propylene).^[92] Note, however, that long-range order in the ternary composites consisting of a diblock copolymer and two kinds of NPs has *not* been reported previously.

In this chapter, we demonstrate, for the first time, that long-range ordered tetragonal single-crystal structures can be formed by loading optimal amounts of hydrophobic Au NPs and hydrophilic CdSe NPs into the respective blocks of a PS-*b*-P4VP. We used high-resolution synchrotron small-angle X-ray scattering (SAXS) and transmission electron microscopy (TEM) to characterize the structures of the PS-*b*-P4VP/CdSe/Au ternary composites.

3-2 Methods and Analysis

3-2-1 Materials. A lamellar PS-*b*-P4VP diblock copolymer [molecular weight (M_n): 20,000 PS/19,000 P4VP; polydispersity index (M_w/M_n): 1.09; Polymer Source, Inc.]

was used in all of the experiments. Hydrophobic dodecanethiol-coated Au NPs, having a core size of 2.5 nm, were synthesized using a two-phase method described by Brust et al.^[139] For the dodecanethiol-coated Au NP synthesis, hydrogen tetrachloroaurate(III) trihydrate ($\text{HAuCl}_4 \cdot 3\text{H}_2\text{O}$), tri-*n*-octylammonium bromide (TOAB, 99%), and sodium borohydride (NaBH_4 , 99%) were obtained from Acros. 1-Dodecanethiol (H-SC_{12} , 98%) was purchased from Aldrich. Hydrophilic pyridine-coated CdSe (CdSe-Py) NPs having a core size of 3.5 nm were synthesized using a modified procedure.^[125] For CdSe NPs synthesis, cadmium oxide (CdO , 99.9%), selenium (Se, 99.9%, 100 mesh), and trioctylphosphine (TOP, 90%) were obtained from Aldrich. Trioctylphosphine oxide (TOPO, 98%) and *n*-hexadecylamine (HAD, 95%) were purchased from Lancaster. Stearic acid (99%) and pyridine (99%) were obtained from Avocado and Showa, respectively. The general solvents toluene (99%), tetrahydrofuran (THF, 99%), acetone (99%), dichloromethane (99%), and ethanol (99%) were obtained from commercial sources. Ultrapure deionized water was produced using a DirectQ3 system equipped with a pump from Millipore, Inc.

3-2-2 Preparation of CdSe-Pyridine (CdSe-Py) NPs and Au-Dodecanethiol NPs.

CdSe-TOPO NPs (core size: 3.5 nm) were synthesized using a procedure reported previously.^[125] The CdSe-TOPO NPs were collected as a powder through size-selective precipitation from methanol and then they were redispersed in toluene. The CdSe-TOPO powder (50 mg) was dissolved in pyridine (5 mL) and stirred at 30 °C overnight. Hexane (30 mL) was added to reprecipitate the CdSe-Py NPs and remove TOPO. The orange/red suspension was centrifuged to collect the powder, which was redissolved in pyridine. Au NPs (core diameter: 2.5 nm) were synthesized using the two-phase method described by Brust et al.^[139] TGA revealed that the dodecanethiol-coated Au NPs were composed of 25 wt% dodecanethiol coronas and 75 wt% Au NP cores.

3-2-3 Preparation of Bulk PS-*b*-P4VP/NP Composites. Scheme 3-1 depicts the procedures employed for sample preparation.

PS-*b*-P4VP/ CdSe Binary Composites: CdSe-Py NPs (0.2, 0.8, 0.17, 2.4, or 3.3 vol% with respect to the volume of PS-*b*-P4VP) were added into a PS-*b*-P4VP/pyridine solution (10 mg/mL). The composite was dried slowly under vacuum at 30 °C and then annealed at 150 °C for 48 h; the bulk PS-*b*-P4VP/CdSe nanocomposites were then solvent-annealed in CH₂Cl₂ for 1 week.

PS-*b*-P4VP/Au Binary Composites: Au NPs (1.3, 2.6, or 5.3 vol% with respect to the volume of PS-*b*-P4VP) were mixed in a PS-*b*-P4VP/THF solution (10 mg/mL) and then dried slowly under vacuum at 30 °C; subsequently, the residue was subjected to the same CH₂Cl₂ solvent annealing process described above.

PS-*b*-P4VP/CdSe/Au Ternary Composites: The annealed PS-*b*-P4VP/CdSe composites were dissolved in THF to form micellar solutions of several composite concentrations. The Au NPs (1.3, 2.6, or 5.3 vol%) were then added to the micellar solutions. Evaporating the THF and subjecting the residue to solvent-annealing in CH₂Cl₂ provided the ternary composites PS-*b*-P4VP/CdSe/Au. The thermal annealing process used to prepare the PS-*b*-P4VP/CdSe intermediates was a critical factor when preparing the highly ordered PS-*b*-P4VP/CdSe/Au ternary composites.

The pyridine ligands on the CdSe NPs were removed during the thermal annealing process, allowing the P4VP chains to interact with greater affinity with the CdSe NPs. For this reason, the CdSe NPs were added into the PS-*b*-P4VP prior to adding the Au NPs. When the process was reversed, some of the Au NPs precipitated because the weak interactions between the PS block and the Au NPs could not sequester the Au NPs stably in the PS block when the CdSe NPs were added in pyridine. The volumes of both the Au NP core and the dodecanethiol corona (φ_{Au}) were taken into account in the calculation of the volume fraction of Au NPs in the

PS-*b*-P4VP, whereas the volume fraction of the CdSe NPs (ϕ_{CdSe}) was calculated based on the sizes of the neat CdSe NPs in the absence of surfactant. The following equations were used:

$$\phi_{\text{CdSe}} = V_{\text{CdSe}} / (V_{\text{PS}} + V_{\text{P4VP}} + V_{\text{CdSe}})$$

$$\phi_{\text{Au}} = (V_{\text{Au}} + V_{\text{HSC12}}) / (V_{\text{PS}} + V_{\text{P4VP}} + V_{\text{Au}} + V_{\text{HSC12}})$$

$$V = W/\rho$$

where ϕ is the volume fraction, V is the volume, W is the weight, and ρ is the density; $\rho_{\text{CdSe}} = 5.8 \text{ g/cm}^3$; $\rho_{\text{Au}} = 19.3 \text{ g/cm}^3$; $\rho_{\text{HSC12}} = 0.844 \text{ g/cm}^3$; $\rho_{\text{P4VP}} = 1.05 \text{ g/cm}^3$; $\rho_{\text{PS}} = 1.04 \text{ g/cm}^3$.

3-2-4 Characterization. Transmission electron microscopy (TEM) was performed using a Hitachi H-600 instrument operated at 100 kV (for higher-contrast images). For TEM samples, ultra-thin slices of the bulk films of the PS-*b*-P4VP/NP composites were microtomed (using a Leica Ultracut Uct apparatus equipped with a diamond knife) and then deposited onto copper grids. Small-angle X-ray scattering (SAXS) measurements were performed at the SWAXS endstation of the BL17B3 beamline of the National Synchrotron Radiation Research Center (NSRRC). The flexible instrument was reported in detail previously.^[149] With a 0.5-mm-diameter beam having a wavelength λ of 1.24 Å (10 keV) and a sample-to-detector distance of 2.4 m, SAXS data were collected in the Q range from 0.007 to 0.3 Å⁻¹, which covered the scattering characteristics of the NPs and the large copolymer-NP complex. Here the wavevector transfer Q was determined using the expression $4\pi\sin(\theta)/\lambda$ in terms of the scattering angle (2θ) and the wavelength of the X-rays (λ). The typical sample size for SAXS was ca. $3 \times 3 \times 0.2 \text{ mm}^3$. All of the SAXS data collected with an area detector were corrected for sample transmission, background, and the detector sensitivity; the value of Q was calibrated using silver behenate. Anomalous small-angle X-ray scattering (ASAXS) was used for characterization the contribution of NPs to

scattering from PS-*b*-P4VP/NPs composites. The incident energies of X-ray are 11.2 keV, 11.9 keV, and 12.65 keV which are lower or near Au L₃-edge (11.919 keV) and Se K-edge (11.658 keV). The measured areas of samples are fixed during changing energies, and the scattering data measured at different energies were normalized as described before.

3-3 Results and Discussions

Figure 3-1 displays the SAXS profiles of neat PS-*b*-P4VP, PS-*b*-P4VP containing 3.3 vol% CdSe NPs, and PS-*b*-P4VP incorporating 5.3 vol% Au NPs. The SAXS profile of the PS-*b*-P4VP block copolymer reveals periodic scattering peaks located at values of Q of 0.0143, 0.0286, 0.0432, 0.0575, and 0.0712 Å⁻¹, representing a lamellar structure. The lamellar spacing (43.9 nm) was extracted from the primary peak of the SAXS profile using Bragg law ($2\pi/Q$). For PS-*b*-P4VP incorporating 3.3 vol% CdSe NPs, the SAXS profile exhibits a similar lamellar ordering with the primary peak at a value of Q of 0.0172 Å⁻¹, indicating a lamellar spacing of 36.5 nm. The reduction in the lamellar spacing of 7.4 nm (i.e., from 43.9 to 36.5 nm) relative to that of the neat state (Figure 3-1b) may have been caused by compression of the P4VP chains (Figure 3-1c). After the nitrogen atoms of the P4VP blocks bonded to the CdSe NPs, the P4VP chains possessed constrained conformations. For PS-*b*-P4VP incorporating 5.3 vol% Au NPs, the SAXS profile after deconvolution reveals a lamellar spacing of 44.9 nm (calculated from scattering peaks at values of Q of 0.0140, 0.0281, and 0.0423 Å⁻¹), slightly larger than that of pure PS-*b*-P4VP. This increase arose presumably because of the weak interactions between the Au NPs and the PS chains, resulting in the Au NPs being located selectively within the PS lamellae (Figure 3-1d). TEM images of the binary composites reveal clearly that the polar

CdSe-Py QDs resided in the P4VP blocks (Figure 3-2a), whereas the hydrophobic Au NPs were dispersed in the PS phase (Figure 3-2b).

Figure 3-3 displays a series of 2-D SAXS images of the copolymer/NP composites incorporated with various amounts of CdSe and Au NPs. The lamellar rings observed for the composite of a low CdSe NPs concentration of 0.2 vol%, indicate that the P4VP/CdSe domains are still dominated by P4VP chains, and prefer to phase-separate from the PS phase for the regular lamellar structure of the neat copolymer, regardless the Au NP concentration (1.3-5.3%). As the loadings of NPs increased to 0.3%-0.8% for CdSe NPs and 2.6%-5.3% for Au NPs, reflections other than that of the lamellar structure start to appear, indicating the formation of a new ordered phase; the lamellar structure still contributes to the SAXS patterns. As the CdSe NP concentration reaches 1.7 vol%, the point-like reflections of the new phase of a single-crystal-like structure replace nearly fully the lamellar powder rings, and the reflection spots are sharpened and intensified upon the increase of the Au-NP concentration from 1.3 to 5.3%. As the CdSe NP concentration is up to 2.4 or 3.3 vol%, the isotropic ring patterns present the lamellar structure, regardless of the Au-NP concentration. The phenomena can be explained in the following. The actual formation of the final morphology of PS-*b*-P4VP/CdSe/Au composites involves a two-stage process and depends on both the volume fraction of CdSe and Au NPs.

The first stage involves the formation of binary PS-*b*-P4VP/CdSe composites, in which regardless of the CdSe NP concentrations from 0.2 vol% to 3.3 vol%, the PS-*b*-P4VP/CdSe binary composites formed with a lamellar structure after thermal annealing. However, the density of the P4VP-CdSe NP binding increases with the loading of CdSe NPs and the edge-to-edge interparticle distance between CdSe NPs decreases from 14.1 nm at 0.2 vol% CdSe NPs to 3.5 nm at 3.3 vol% CdSe NPs as listed in Table 3-1 (see Appendix 2 for the calculating details). Then, the second stage

consists of using THF to dissolve both PS-*b*-P4VP/CdSe composites and dodecanethiol-coated Au NPs and subsequent CH₂Cl₂ solvent annealing. For a low loading with CdSe NPs, such as 0.2 and 0.8 vol%, the degree of P4VP–CdSe binding was not high enough (i.e. P4VP chains are mobile.) to prevent P4VP/CdSe lamellae from being dissolved in THF to form a micellar structure that consists of a P4VP/CdSe core and a PS corona. Consequently, the PS-*b*-P4VP/CdSe/Au solution with a low density of P4VP–CdSe NP binding could coalesce into P4VP/CdSe lamellae and PS/Au lamellae during CH₂Cl₂ solvent annealing. As the loading of CdSe NPs increases to 1.7 vol%, the density of P4VP–CdSe NP binding may reach a state that P4VP/CdSe domains have the proper density of P4VP–CdSe binding that is not too high to prevent them from being dissolved in THF. Subsequently, during CH₂Cl₂ solvent annealing process, owing to the presence of dodecanethiol-coated Au NPs in the PS domains, the P4VP/CdSe domains can not coalesce into lamellar. However, at a higher loading of CdSe NPs, such as 2.4 and 3.3 vol%, the P4VP/CdSe lamellae that experienced thermal annealing, containing a higher density of P4VP–CdSe binding (a high cross-linking density), could not be redissolved in THF completely, so no further phase transition was found in the second stage. In other words, the lamellar morphology of the composites in the first stage has been retained. Consequently, The interesting phase transition from the lamellar structure to the a single-crystal-like structure induced by the CdSe NPs and Au NPs must be crucial, as we cannot find a single-crystal-like structure in the PS-*b*-P4VP/Au or PS-*b*-P4VP/CdSe composite, nor by adding dodecanethiol molecules into the PS-*b*-P4VP/CdSe composite.

Figure 3-4 displays the SAXS patterns and the corresponding TEM image of the ternary PS-*b*-P4VP/CdSe/Au composite incorporated with 1.7 vol% CdSe NPs and 5.3 vol% Au NPs. Figures 3-4a and 3-4b reveal the single-crystal-like reflections

obtained from different sample areas of the ternary composite. Both of the reflections in Figures 3-4a and 3-4b can be grouped into three orientations of the tetragonal cell in Figure 3-4d, including reflections from the $a \times b$ plane (white indices) and reflections from the twin $a \times c$ (orange indices) and $b \times c$ (red indices) planes at a tilted angle of ca. 30° . Moreover, we have extracted the large cell dimensions to be values of a and b of 48.7 nm and a value of c of 68.9 nm. Lack of diffraction patterns from other orthogonal incident directions, the tetragonal structure cannot be fully confirmed; an alternative support for the tetragonal-like cell, however, is obtained from the TEM image shown below.

Figure 3-4c displays the corresponding TEM image; the inset presents an enlarged TEM image indicating isolated P4VP/CdSe nanodomains surrounded by a continuous PS/Au phase. The sample volume ($1 \times 1 \times 0.07 \mu\text{m}^3$) under the TEM electron beam was not sufficiently large to produce an electron diffraction pattern comparable to that of SAXS ($500 \times 500 \times 200 \mu\text{m}^3$). A fast Fourier transform (FFT) image (Figure 3-5a) of the TEM image in Figure 3-4c revealed two pairs of diffraction patterns with a four-fold symmetry axis. Furthermore, inverse FFT images in Figure 3-5 displayed clear fourfold gridlike patterns. The EDX spectra in Figure 3-6 confirmed that the CdSe and Au NPs were located in the P4VP nanodomains and PS blocks, respectively. As a result, we observed a periodic structure for the P4VP/CdSe domains along the in-plane direction of the pristine P4VP lamellae; such in-plane ordering crossed by the neighboring PS/Au layers develops an additional ordering direction perpendicular to the in-plane direction. The two striations visible in the TEM image of the P4VP/CdSe packing (Figure 3-4c) are the [110] and [001] cell directions of the tetragonal cell, corresponding to the plane (red parallelogram) revealed in Figure 3-4d, with the characteristic spacing (34 nm) matching well with

the d-spacing of the (110) (34.4 nm) and (002) (34.4 nm) facets of the tetragonal cell suggested by SAXS.

Figure 3-7a displays an azimuthal scan of the single-crystal-like pattern in Figure 3-4b and the relative peaks of each reflection plane. The azimuthal scan also reveals relative sharp reflections having a full width at half maximum (FWHM) of ca. 2°, which corresponds to the mosaicity of the single-crystal-like structure. Moreover, Figure 3-7b displays the $I(Q)$ profile taken along a symmetrical scattering direction (10-1) from the image in Figure 3-4b. We extracted the crystal size to be ca. 0.8 μm using the Debye–Scherrer^[153] equation: $D = k\lambda/[\beta \cos(\theta)]$, where D is the thickness of the crystal grain, k is the shape correction constant (normally equal to 0.95 for a spherical particle), λ is the incident X-ray wavelength, β is the FWHM of the Bragg peak, and θ is the Bragg angle. In our case, λ was 1.24 Å and β was 0.0085° (from $Q_{\text{FWHM}} = 0.0015 \text{ \AA}^{-1}$).

Based on the SAXS and TEM results, we propose a possible route for the formation of the tetragonal cell (Scheme 3-2). During the first stage, the PS-*b*-P4VP/CdSe composite displays a lamellar structure of a smaller spacing than that of pure PS-*b*-P4VP, with CdSe-free voids at the PS/P4VP interface (corresponding to those in Figure 3-2a). The formation of these CdSe-free voids in P4VP/CdSe lamellae arose from the PS-*b*-P4VP/CdSe micelles combining to form a roughened PS/P4VP interface during the evaporation of pyridine and the thermal annealing. Subsequently, the PS-*b*-P4VP/CdSe composite and Au NPs were mixed in THF; micelles possessing a P4VP/CdSe core and a PS corona formed, but there should be no interactions between the PS-*b*-P4VP/CdSe micelles and the Au NPs, as evidenced from the related solution-state SAXS results which indicated no additional scattering intensity in the case of the coexistence of CdSe and Au NPs (Figure 3-8). Finally, after removing THF and a subsequent solvent-annealing with CH₂Cl₂, the

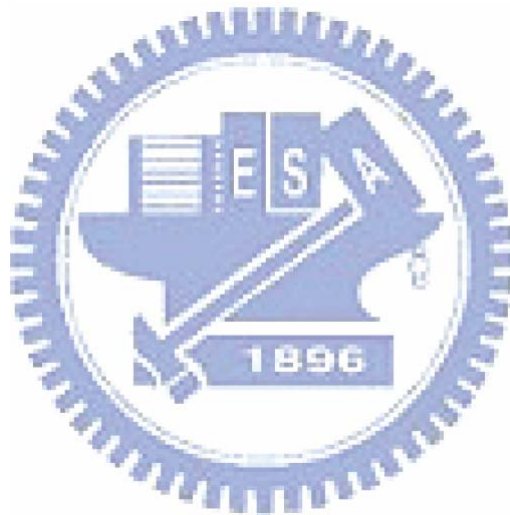
PS-*b*-P4VP/CdSe/Au composite formed a tetragonal-like structure with P4VP/CdSe nanodomains taking the lattice sites in the PS/Au network matrix.

In general, diblock copolymers form body-centred cubic, face-centred cubic, and simple cubic ordered spherical morphologies. In contrast, the ternary PS-*b*-P4VP/CdSe/Au composite incorporating with appropriate CdSe NPs (~1.7 vol%) and Au NPs (1.3-5.3 vol%) can form a tetragonal-like structure, which, for a diblock copolymer, is unusual, especially in diblock copolymer/NP composites; they have been observed previously only under influences of special interactions.^[154] Recent studies indicated that modification of interfacial curvature of diblock copolymers through the incorporation of liquid crystalline molecules could also lead to various novel microdomain structures, and a tetragonal packing structure could be obtained with symmetrical PS-*b*-P4VP upon the incorporation with dodecylbenzenesulfonic acid (DBSA).^[155] In our case, a non-spherical distribution of the CdSe NPs (inset of Figure 3-2a) inside the P4VP domains might perturb the originally spherical neat P4VP domains, leading to an anisotropic curvature of the P4VP/CdSe microdomains in the composite, thus, a tetragonal micelle packing rather than the conventional BCC packing. The interactions between Au NPs and CdSe NPs might further enhance the anisotropic curvature effect for the long-ranged tetragonal-like structure.

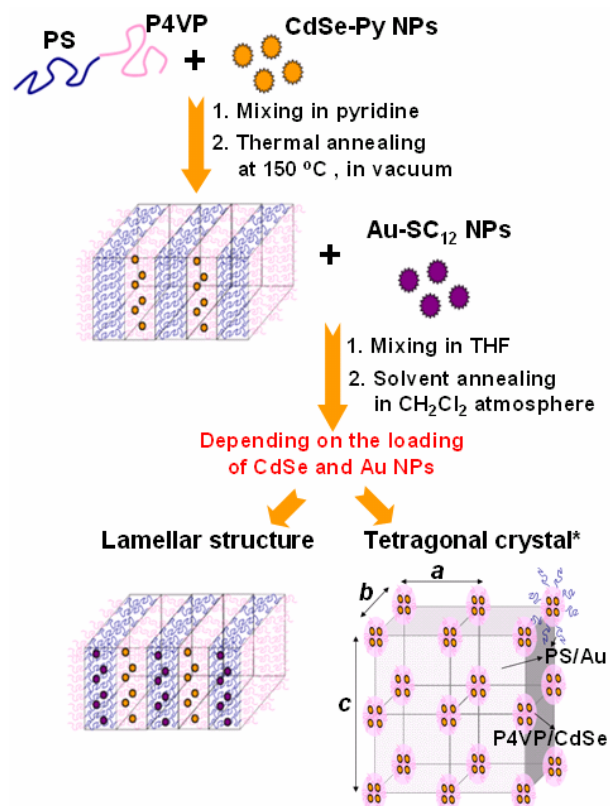
3-4 Conclusions

We have demonstrated that pre-synthesized hydrophilic CdSe NPs and hydrophobic Au NPs can collectively self-organize in the two distinct blocks of a PS-*b*-P4VP diblock copolymer to form a highly ordered structure. At optimal concentrations of the CdSe NPs and Au NPs, the binding between the P4VP blocks and the CdSe NPs and the weak interactions between the PS blocks and the Au NPs led to dispersion of the two types of NPs in their respective P4VP and PS blocks and

subsequent formation of a single-crystalline-like structure comprising P4VP/CdSe nanodomains situated at the apexes of the tetragonal cell and a matrix filled with the PS/Au NP network.



Scheme 3-1. Schematic Representation of the Method of Preparation of the PS-*b*-P4VP/CdSe/Au Ternary Composites.



*The Au NPs dispersed throughout the continuous PS phase are not presented in the depiction of the tetragonal crystal.

Scheme 3-2. Formation of Tetragonal Crystals from PS-*b*-P4VP/CdSe/Au Ternary Composites.

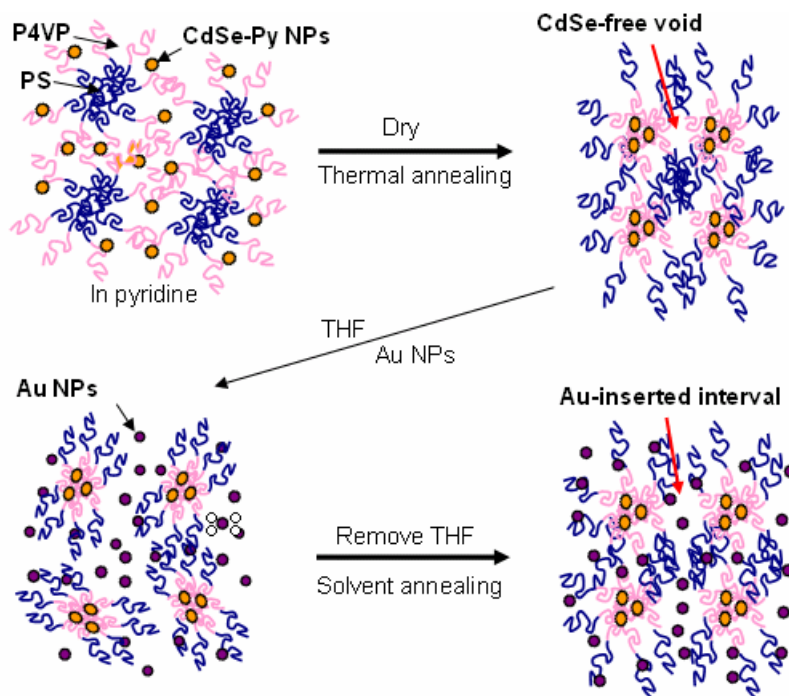
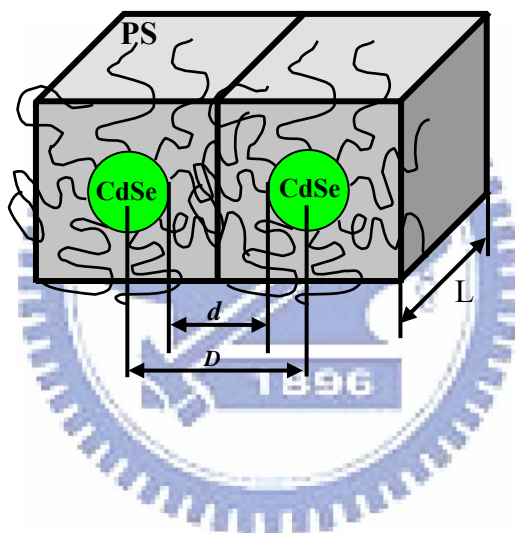


Table 3-1. Average center-to-center (D) and edge-to-edge (d) interparticle distances. The schematic representation of the cubic lattice model for the free volume per CdSe dot in a single P4VP domain.

volume fraction (%)	D (nm)	d (nm)
0.2	17.6	14.1
0.8	11.1	7.6
1.3	8.7	5.2
2.4	7.8	4.3
3.3	7.7	3.5



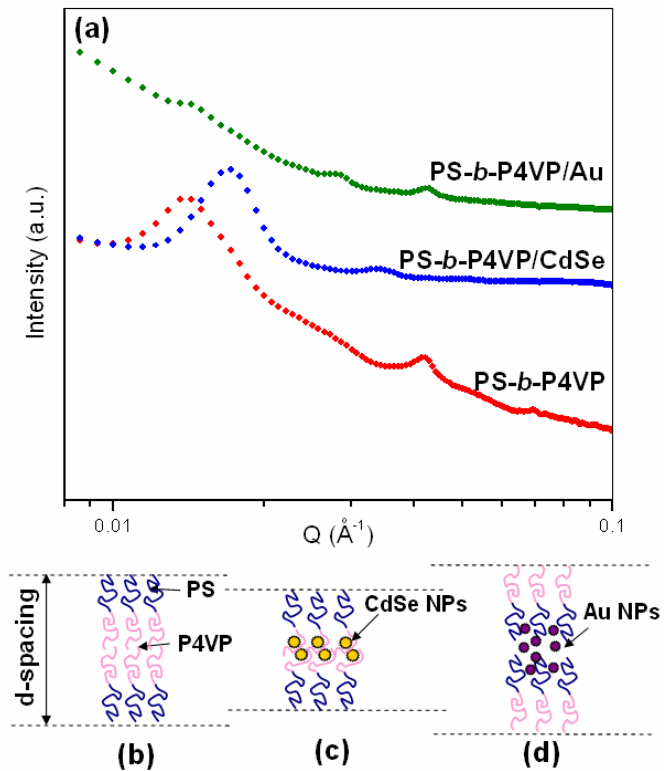


Figure 3-1. (a) SAXS profiles of PS-*b*-P4VP, PS-*b*-P4VP/CdSe NPs (3.3 vol%), and PS-*b*-P4VP/Au NPs (5.3 vol%). (b-d) Cartoon representations of the structures of the PS-*b*-P4VP/NP binary composites representing the SAXS profiles in (a).

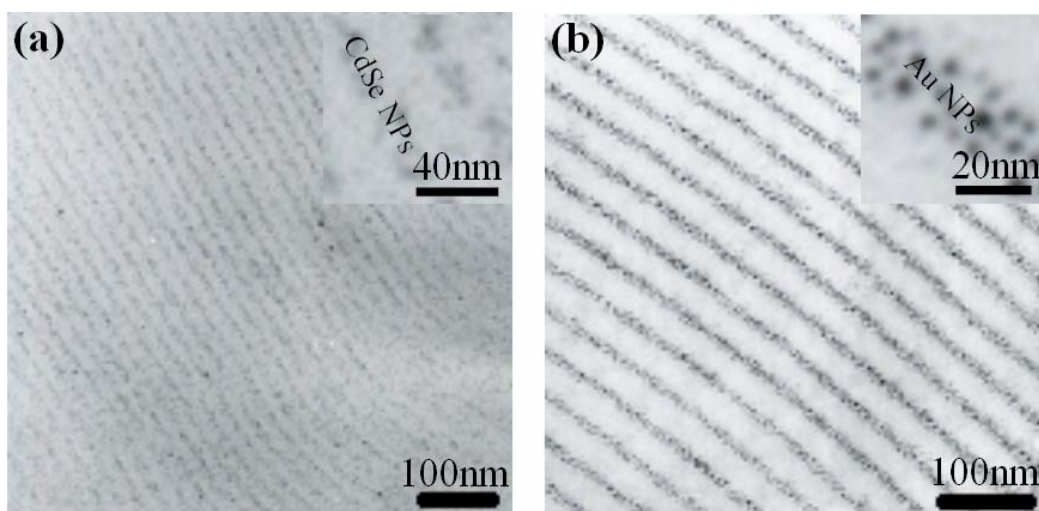
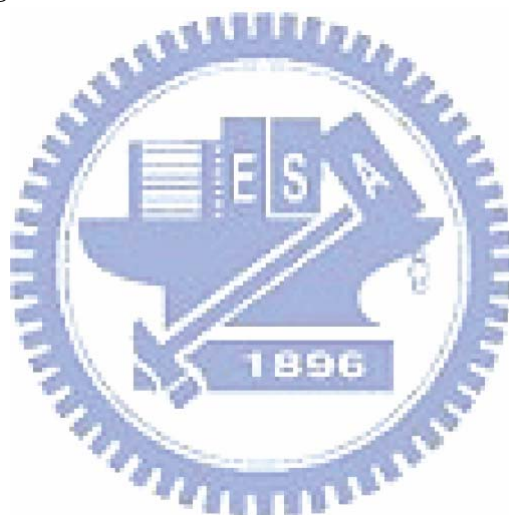


Figure 3-2. TEM images of the (a) PS-*b*-P4VP/3.3 vol% CdSe NPs and (b) PS-*b*-P4VP/5.3 vol% Au NPs binary composites. The insets to (a) and (b) display enlarged partial images.



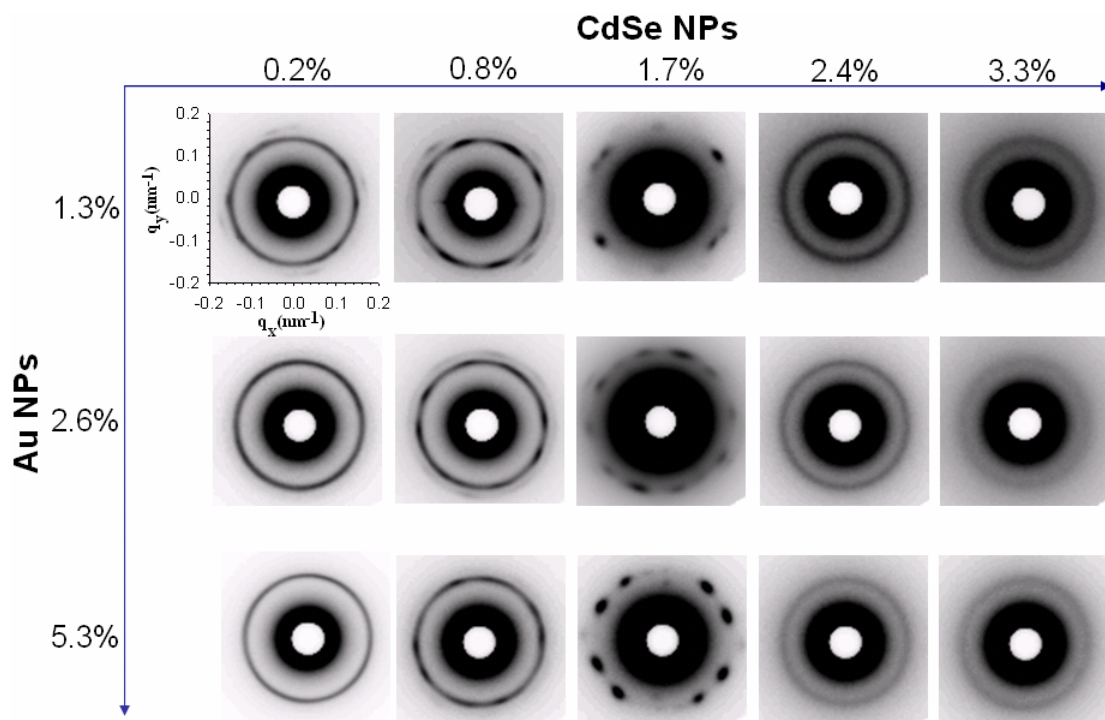


Figure 3-3. 2D SAXS patterns in the low- Q range ($q = 0.06 - 0.2 \text{ nm}^{-1}$) for PS-*b*-P4VP/CdSe/Au ternary composites possessing various NP loadings. The contrast for each pattern is independent.



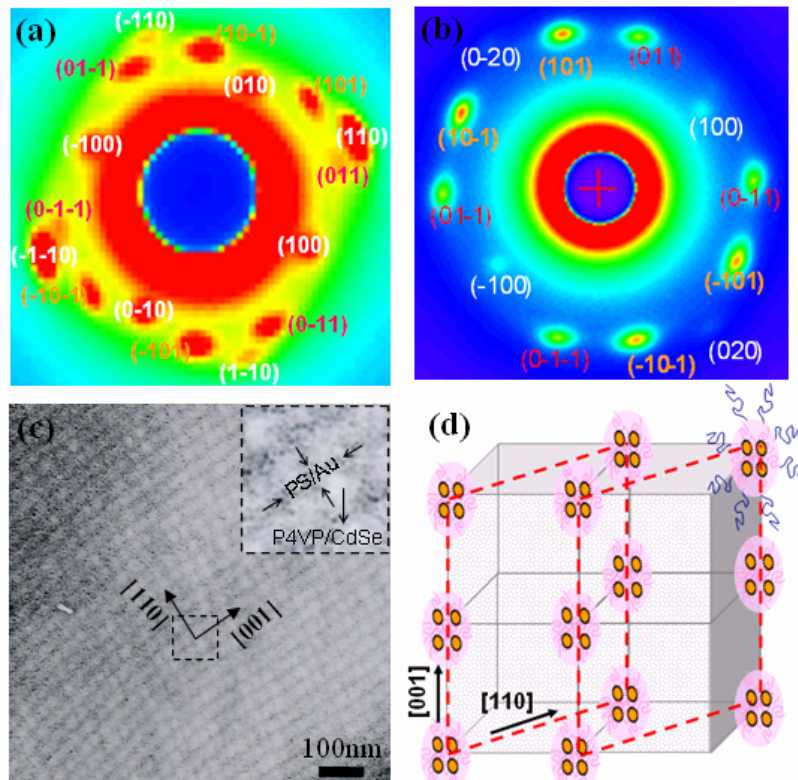


Figure 3-4. 2D SAXS patterns in low- Q range ($q = 0.06 - 0.2 \text{ nm}^{-1}$) for the PS-*b*-P4VP/CdSe/Au composite containing 1.7 vol% CdSe NPs and 5.3 vol% Au NPs. (a, b) The Miller indices are marked according to a tetragonal cell, used to index the diffraction patterns of the ab plane (white), superimposed over the tilted ac (orange) and bc (red) planes. (c) TEM images of PS-*b*-P4VP/1.7 vol% CdSe NPs/5.3 vol% Au NPs ternary composites revealing the [110] and [001] cell directions of the tetragonal cell. The upper-right-hand inset displays an enlarged image. (d) Corresponding orientation for the TEM images.

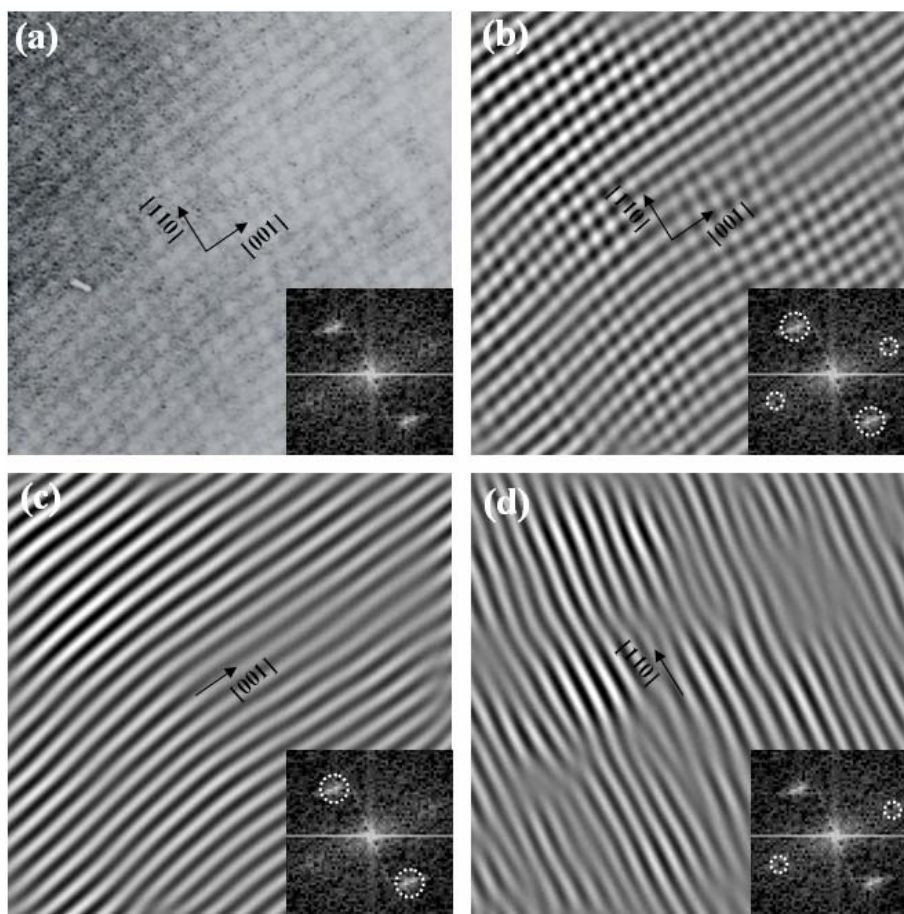


Figure 3-5. (a) TEM image of the PS-*b*-P4VP/1.7 vol% CdSe NP/5.3 vol% Au NP composite. The inset displays the FFT of (a). (b) Reconstructed image (inverse FFT image) from the FFT image taken by the two pairs of FFT spots highlighted in the inset. (c, d) Reconstructed images taken by the single pairs of FFT spots highlighted in the respective insets.

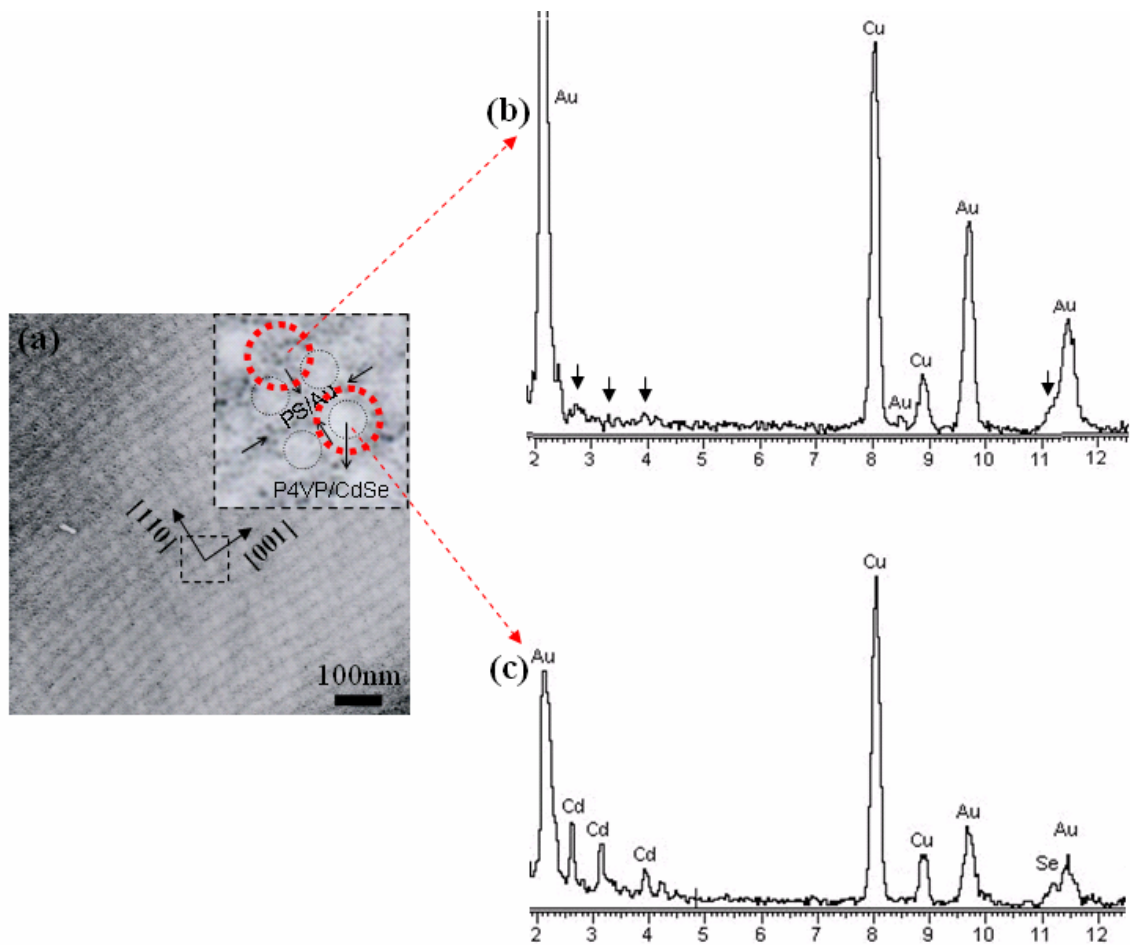


Figure 3-6. (a) TEM image of the PS-*b*-P4VP/1.7 vol% CdSe NP/5.3 vol% Au NP composite. EDX spectra recorded from the (b) PS/Au and (c) P4VP/CdSe phases marked by red dashed circles in the enlarged TEM image.

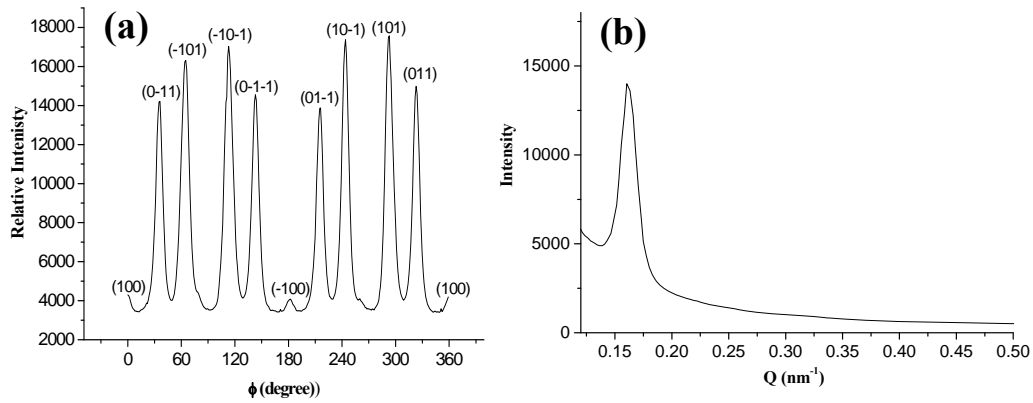
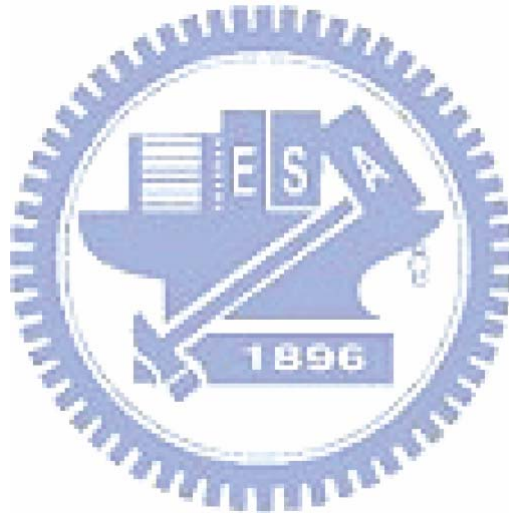


Figure 3-7. (a) Azimuthal scanning profile of the image in Figure 3-4b ($Q = 0.161 \text{ nm}^{-1}$); the (100), (0-1-1), (-101), (-10-1), (0-1-1), (-100), (01-1), (01-1), (10-1), (101), and (011) reflections are found at values of ϕ of 0° , 36° , 65° , 113° , 143° , 180° , 216° , 244° , 293° , and 323° , respectively. **(b)** SAXS profile obtained along the (101) spot in Figure 3-4b.



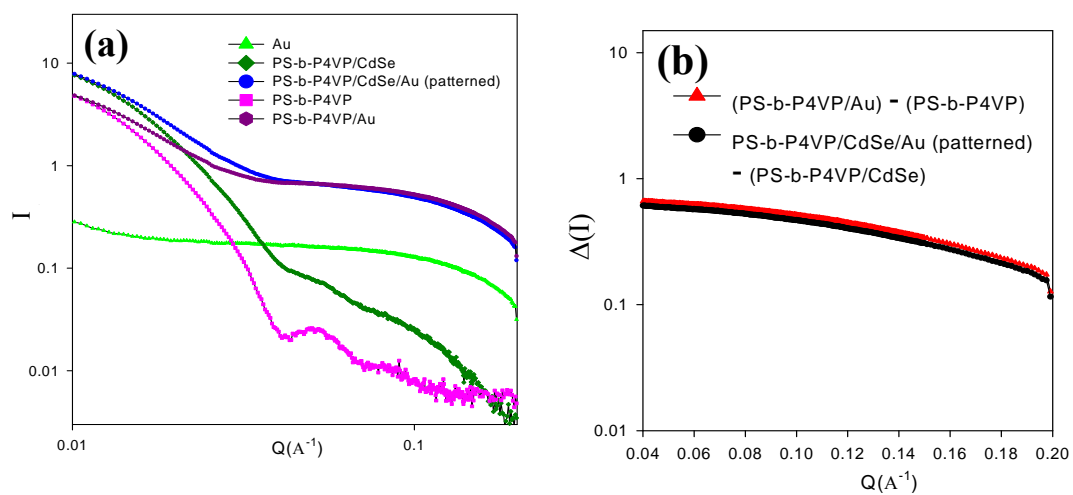
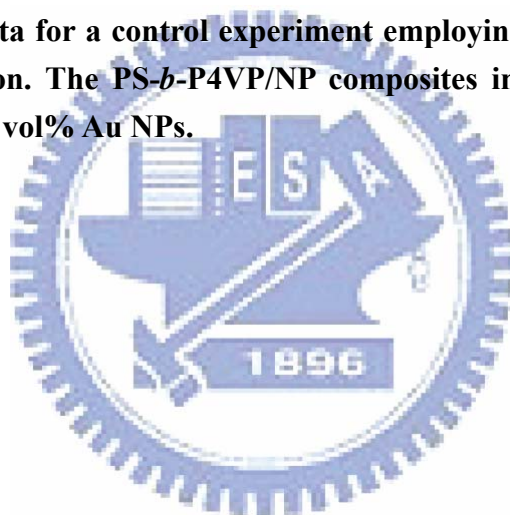


Figure 3-8. SAXS data for a control experiment employing PS-*b*-P4VP/CdSe/Au composites in solution. The PS-*b*-P4VP/NP composites incorporating 1.7 vol% CdSe NPs and/or 5.3 vol% Au NPs.



Chapter 4

Electrical Bistable Memory Device Based on a Poly(styrene-*b*-4-vinylpyridine) Nanostructured Diblock Copolymer Thin Film

4-1 Introduction

Diblock copolymers are self-assembled soft materials that can possess a variety of ordered structures—e.g., classical lamellae, hexagonal cylinders, and spheres—having periodic thicknesses ranging between 10 and 100 nm. Hence, the use of block copolymers as templates is a simple approach toward producing hierarchically ordered structures for electrical applications.^[100, 125, 156] Electrically bistable nonvolatile memory devices incorporating organic materials are attracting considerable attention because of their many advantageous properties, including flexibility, material variety, and low cost. Bistable organic memory devices exhibit two different conductive states that can be manipulated by controlling the voltage or current; the resulting change resistance can occur through several mechanisms, such as the trapping/detrapping of charges by nanoclusters in the insulator,^[116,117] the rupture and formation of conductive filaments,^[118,119] reduction/oxidation processes,^[120] and intramolecular conformational changes.^[121] The use of self-assembled block copolymers thin films as dielectrics or active layers in organic memory devices has been studied only rarely. In this paper, we report an electrically bistable organic device based on a self-assembled poly(styrene-*b*-4-vinylpyridine) (PS-*b*-P4VP) diblock copolymer thin film possessing a hexagonal nanostructure, which exhibits novel resistive switching characteristics relative to those of homopolymeric PS and P4VP thin films. The resistive switching behavior of the device can be modeled by considering that it functions through a metallic filament mechanism.

4-2 Methods and Analysis

4-2-1 Materials. A PS-*b*-P4VP diblock copolymer employed (Polymer Source, Inc.) had molecular weights (M_n) of its PS and P4VP components of 46,900 and 20,600, respectively, with a polydispersity index ($PDI=M_w/M_n$) of 1.14. PS homopolymer having a weight-averaged molecular weight (M_w) of 13,500 with a PDI of 1.06 was purchased from Pressure Chemical. P4VP having a weight-averaged molecular weight (M_w) of 96,200 with a PDI of 1.18 was purchased from Polymer Science Inc. Chlorobezene (C_6H_5Cl , 99.97%) and Pyridine Anhydrous (C_5H_5N , 99.9%) was purchased from TEDIA. Indium Tin Oxide (ITO) glass with a ITO thickness of 140 nm had a resistance of $15 \Omega/\square$ was purchased from UID Co..

4-2-2 The Fabrication of Al/Polymer/ITO devices. Figure 4-1 displays the process we adopted to prepare a nonvolatile memory device comprising a monolayer PS-*b*-P4VP thin film, an ITO bottom electrode, and an Al top electrode. This PS-*b*-P4VP copolymer possessed a hexagonal cylinder structure in the bulk state (Figure 4-1a), but forms a micellar structure that consists of a PS corona and a P4VP core when dissolved at 0.5 wt% in chlorobenzene (Figure 4-1b). This micellar PS-*b*-P4VP solution was spin-coated at 3000 rpm onto an ozone-treated ITO electrode to form a monolayer PS-*b*-P4VP thin film. To obtain an ordered hexagonal P4VP assembly (Figure 4-1c), this monolayer PS-*b*-P4VP thin film was thermally annealed at 150 °C under vacuum for 3 h. A 50-nm-thick film of Al was thermally evaporated through a shadow mask (deposition rate: $4 \text{ \AA}/s$; pressure: 10^{-6} torr) onto the PS-*b*-P4VP film to form a top electrode. The SEM image of a cross-section of the Al/PS-*b*-P4VP/ITO device (Figure 4-1d) reveals the high quality of the interfaces between the layers. The control cases of PS and P4VP thin film were obtained by the same process to PS-*b*-P4VP.

4-3 Results and Discussions

We measured the electrical characteristic of Al/PS-*b*-P4VP/ITO, Al/PS/ITO, and Al/P4VP/ITO devices by semiconductor parameter analyzer (HP4156C, Agilent) performed on probe station (VFTTP4, Lakeshore) under 10^{-5} torr at room temperature, semi-logarithmic current–voltage (I – V) plots from them as displays in Figure 4-2. For the Al/PS/ITO device featuring a homogenous PS surface, the I – V characteristics display a low current that increased slowly upon increasing the applied voltage, indicating that PS is a good insulator that has no memory effect. In contrast, the Al/PS-*b*-P4VP/ITO and Al/P4VP/ITO devices displayed electrical bistability with a sufficiently large sensing margin between the ON and OFF states.

The I – V characteristics of the Al/P4VP/ITO device initially exhibited a high-resistance state (OFF state); after performing a negative-voltage sweep to ca. -0.5 V, the device was switched to a low-resistance state (ON state). When a positive-voltage sweep was applied to ca. $+1.2$ V, the device switched back to its initial OFF state. The maximum ON/OFF current ratio for the P4VP device was 2×10^3 at -0.1 V. For the Al/PS-*b*-P4VP/ITO device, the turn-on and turn-off threshold voltages were -0.5 and $+0.75$ V, respectively; the maximum ON/OFF current ratio was 2×10^5 at -0.1 V. The AFM topographic image of the PS-*b*-P4VP thin film (inset to Figure 4-2) reveals the micro phase separation of quasi-hexagonal structures that resulted from the micellization of PS-*b*-P4VP; the light regions (size: ca. 30 nm) represent the P4VP domains and the dark areas represent the PS matrix.

For both the Al/PS-*b*-P4VP/ITO and Al/P4VP/ITO devices, after removing the compliance current limit, the magnitudes of the turn-off currents were larger than their turn-on compliance currents.^[115] In addition, the ON state of each device could be converted into the OFF state by applying the sweeping voltage in the same direction. This behavior can be explained by considering a metallic filament theory.^[157]

To prove that the metallic filamentary mechanism operated, we used a cryostat system operated under 10^{-5} torr to measure the temperature dependence of the resistance of the ON state of the Al/PS-*b*-P4VP/ITO memory devices. Figure 4-3 reveals that the conduction mechanism of the ON state is dominated by ohmic conduction ($I \propto V$). The resistance of the ON state increased linearly upon increasing the temperature—typical of metallic behavior. The equation $R = R_0[1 + \alpha(T - T_0)]$ represents the variation of the resistance with respect to the temperature, where α is the temperature coefficient and R_0 is the resistance measured at a reference temperature T_0 , usually 293 K.^[158] The temperature coefficient of 0.0031 that we obtained after fitting the results in the inset to Figure 4-3 is slightly smaller than the acknowledged value of 0.0043.^[159] This discrepancy may be due to thermal losses occurring at the contact between the Al/PS-*b*-P4VP/ITO device and the cryoprobe.^[160]

P4VP, which contains pyridyl groups, interacts strongly with Al clusters or atoms. The diffusion of these Al clusters or atoms is, however, negligible because PS has a low affinity toward this metal.^[161] We suspect that Al atoms migrated into the P4VP zones to form metallic filaments and that these Al filaments grew during the writing progress. The dimensions of the P4VP nanodomains in the PS-*b*-P4VP thin film would limit the growth and size of these Al filaments, whereas a homopolymeric P4VP thin film might have no limitation to the extent of growth of similar Al filaments. In general, filaments having larger size would be more difficult to break. Thus, scaling down the size of the organic memory materials to the nanometer scale resulting from the self-assembled diblock copolymer provides the organic memory device with a higher ON/OFF ratio and lower erasing and writing voltages.

Figure 4-4a displays the time-resolved I - V characteristics of the Al/PS-*b*-P4VP/ITO organic memory device. The write/read/erase/read cycle was recorded using an oscilloscope (Keithley, 4200-SCP2HR) equipped with an arbitrary waveform

generator (Keithley, 4205-PG2) and a programming current amplifier (Keithley, 428). In general, the switching speed depends on the amplitude of the write/erase signal. Our read/write/erase cycle sequence consisted of a 5 μ s write pulse at -1.5 V, a 10 μ s erase pulse at 5 V, and a 0.1 V read voltage. Applying the write and erase pulses switched the device to its ON and OFF states, respectively. Although the switching speed of this Al/PS-*b*-P4VP/ITO memory device was acceptable for its use in most consumer products, there is much room for improvement.

Our Al/PS-*b*-P4VP/ITO organic memory device was nonvolatile: it was stable and could be read many times as long as the probing voltage remained below the threshold voltage. Figure 4-4b displays the retention characteristics of our Al/PS-*b*-P4VP/ITO organic memory device, measured by monitoring the current at -0.1 V after programming and erasing at -1.5 and 5 V, respectively, with a 100 μ s pulse bias. The currents in the ON and OFF states differed by five orders of magnitude, with no significant changes after 10^4 s. We extrapolated a 10-year memory window for our Al/PS-*b*-P4VP/ITO organic memory device; the memory window of ca. 10^5 is sufficient for its use in practical nonvolatile memory devices.

4-4 Conclusions

We have demonstrated that a device incorporating a micellar thin film of a diblock copolymer, consisting of metal-coordinated cores and insulating shells, operates through the formation of metallic filaments. This Al/PS-*b*-P4VP/ITO organic nonvolatile memory device is switchable with a long retention time and an acceptable programming speed; notably, it exhibits a lower erase threshold voltage and a higher ON/OFF ratio than those of the corresponding Al/P4VP/ITO device. This fabrication approach opens up new possibilities for improving the memory performance of polymeric materials prepared at low cost using simple processes.

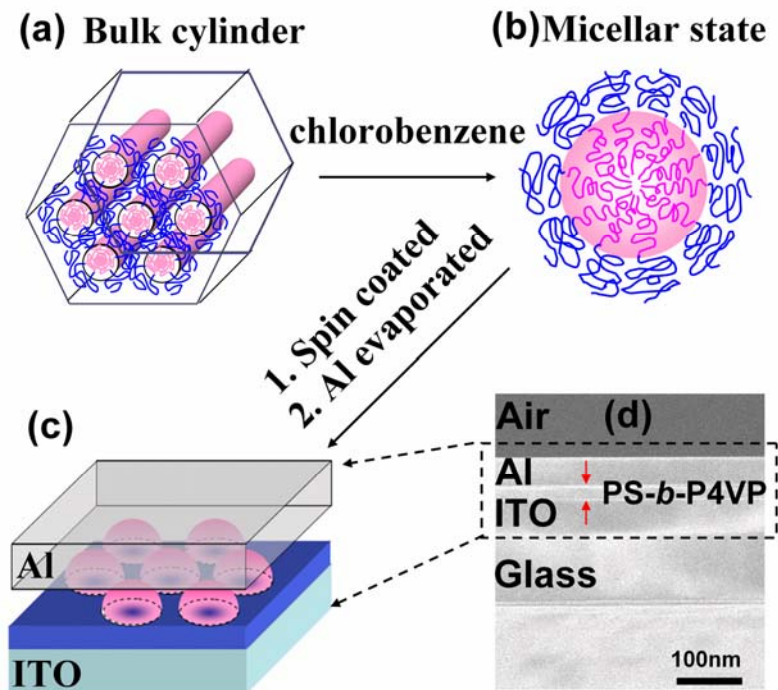


Figure 4-1. (a) Morphology of a cylindrical PS-*b*-P4VP diblock copolymer in the bulk state. (b) Micellar structure of a cylindrical PS-*b*-P4VP diblock copolymer in a selective solvent. (c) Nonvolatile memory device comprising an active PS-*b*-P4VP diblock copolymer film and Al and ITO electrodes. (d) SEM image of the cross-section of the memory device in (c).

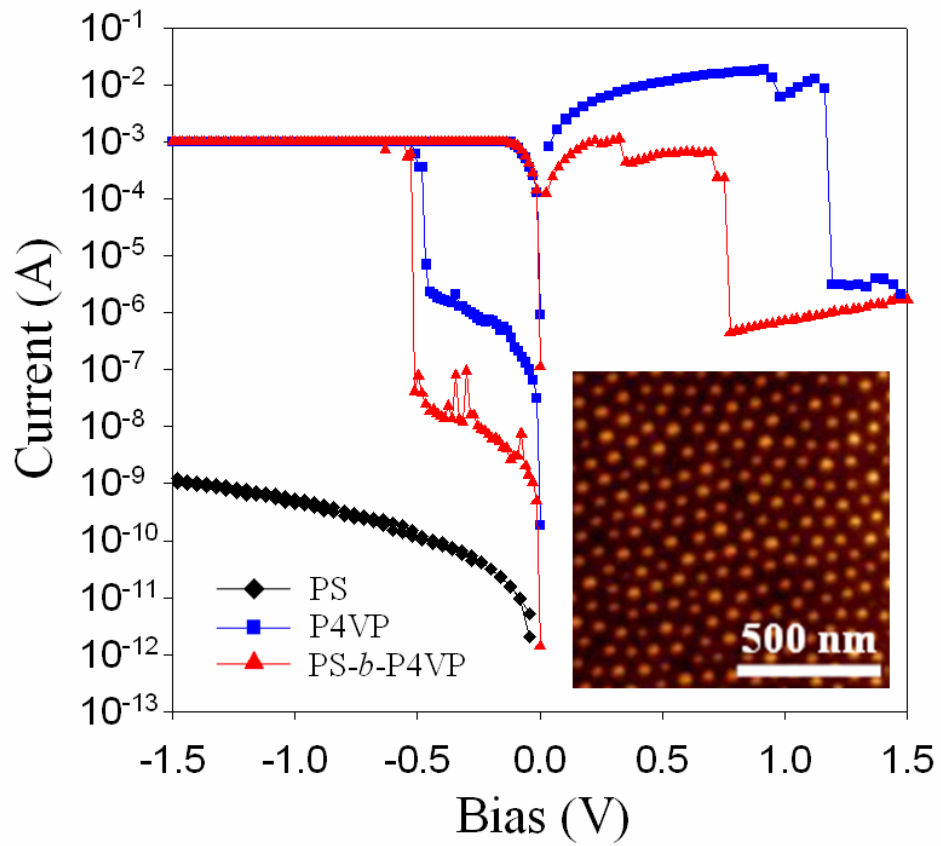


Figure 4-2. I - V characteristics of PS (\blacklozenge), P4VP (\blacksquare), and PS- b -P4VP (\blacktriangle). The turn-on compliance current was restricted to 10^{-3} A. The inset displays an AFM topographic image of the PS- b -P4VP thin film prior to evaporating the Al electrode.

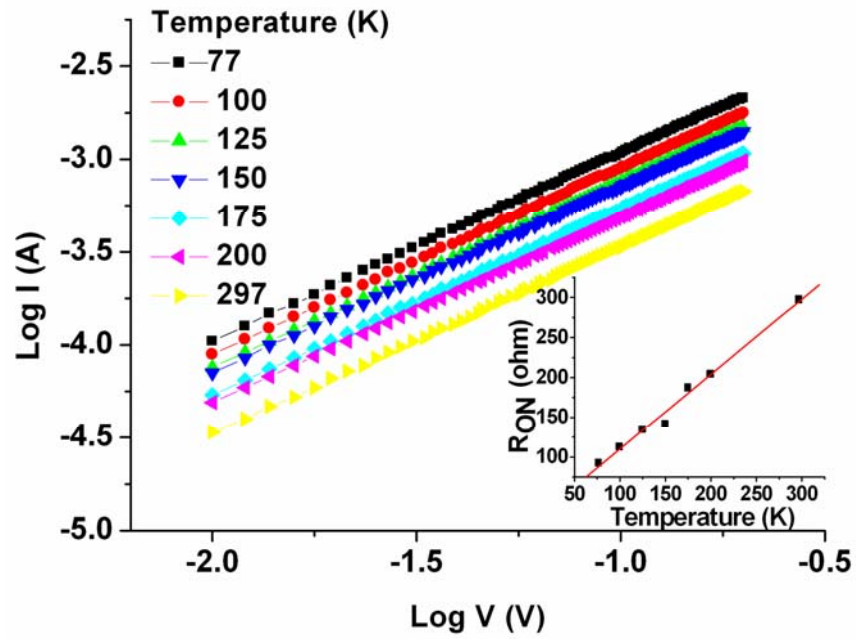
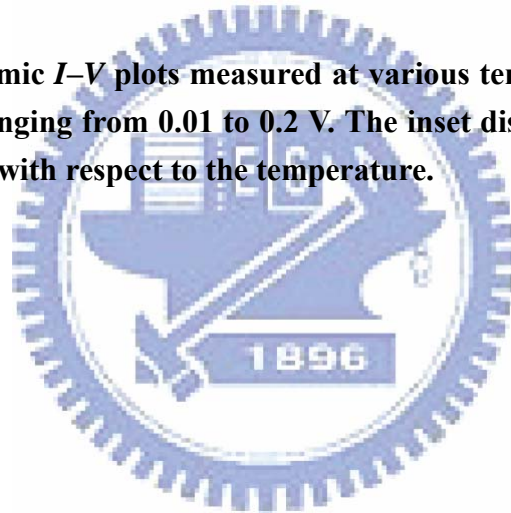


Figure 4-3. Logarithmic I - V plots measured at various temperatures for the ON state at potentials ranging from 0.01 to 0.2 V. The inset displays the resistance of the ON state plotted with respect to the temperature.



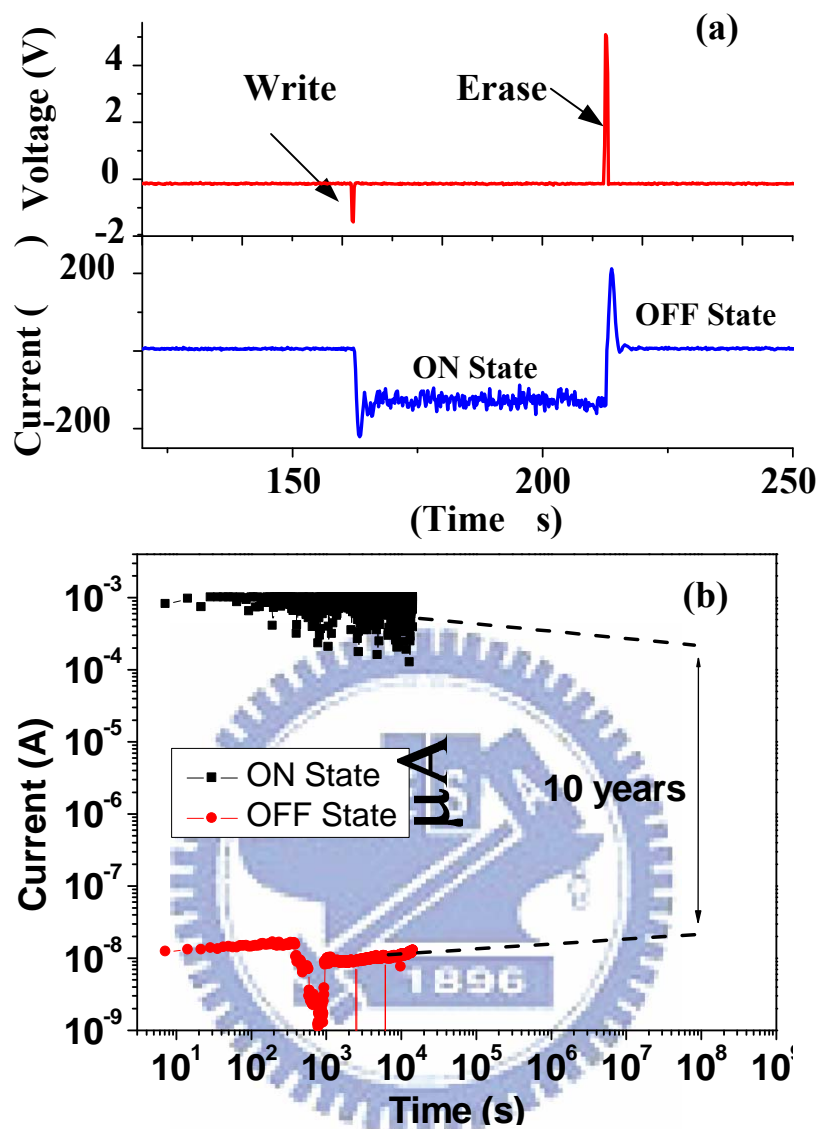


Figure 4-4. (a) Write/read/erase test of the ITO/PS-*b*-P4VP/Al organic memory device. The bottom and top curves represent the applied voltage pulse and the corresponding current response, respectively. (b) Retention times of the ON and OFF states of the ITO/PS-*b*-P4VP/Al organic memory device probed in terms of the device current after stressing.

Chapter 5

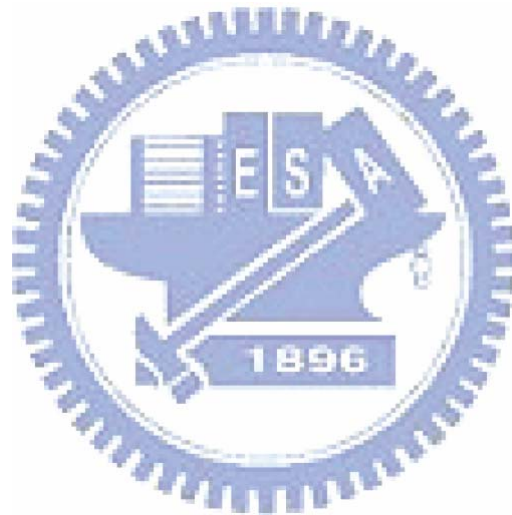
Conclusions

In the case of PS-*b*-P4VP/AuSC₂Ph NP binary mixtures, we have monitored the structural evolution of spherical PS-*b*-P4VP/AuSC₂Ph NP mixtures in the solid state during thermal annealing by in-situ SAXS. We found that the Au NPs that existed in a random state with some cluster packing in the PS domain diffused to the interface of the amphiphilic PS-*b*-P4VP diblock copolymer within 4 h at 170 °C under vacuum to form NP-filled shell-like assemblies. We speculate that this interfacial activity of AuSC₂Ph results most from the fact that the initially hydrophobic Au NP surfaces became more hydrophilic after ~70% of the 2-phenylethanethiol ligands had evaporated off. The Au NP-filled assemblies located at the interface between the PS and P4VP blocks were quite stable; they remained in the form of PS-Au-P4VP core/shell/corona onion micelles even after redissolving the samples in toluene.

In the case of PS-*b*-P4VP/CdSe-Py/AuSC₁₂ ternary mixtures, we have demonstrated that pre-synthesized hydrophilic CdSe NPs and hydrophobic Au NPs can collectively self-organize in the two distinct blocks of a PS-*b*-P4VP diblock copolymer to form a highly ordered structure. At optimal concentrations of the CdSe NPs and Au NPs, the binding between the P4VP blocks and the CdSe NPs and the weak interactions between the PS blocks and the Au NPs led to dispersion of the two types of NPs in their respective P4VP and PS blocks and subsequent formation of a single-crystalline-like structure comprising P4VP/CdSe nanodomains situated at the apexes of the tetragonal cell and a matrix filled with the PS/Au NP network.

In the case of PS-*b*-P4VP thin film, we have demonstrated that a device incorporating a micellar thin film of a cylindrical PS-*b*-P4VP diblock copolymer, consisting of metal-coordinated cores and insulating shells, operates through the formation of metallic filaments. This Al/PS-*b*-P4VP/ITO organic nonvolatile memory

device is switchable with a long retention time and an acceptable programming speed; notably, it exhibits a lower erase threshold voltage and a higher ON/OFF ratio than those of the corresponding Al/P4VP/ITO device. This fabrication approach opens up new possibilities for improving the memory performance of polymeric materials prepared at low cost using simple processes.



Chapter 6

Future Work

Following the investigations in this thesis, a number of potential projects could be taken up.

For the investigation on incorporating Au NPs into a PS-*b*-P4VP:

- Further study on the electrical and optical properties of the PS/Au/P4VP corona-shell-core micellar structure, for example, proximity effect.
- Further study on tuning the chemistry and density of the tails on the surfaces of NPs in order to realize the formation of the interfacial interaction of NPs.

For the investigation on the single-crystalline tetragonal structure formation by incorporating CdSe and Au NPs into PS-*b*-P4VP:

- Further analysis could be carried out by *3-D tomography of TEM* to directly determine the PS-*b*-P4VP/CdSe/Au single-crystalline tetragonal structure.
- Further study on tuning the molecular weight of PS-*b*-P4VP to alter the shell and core sizes of PS-*b*-P4VP/CdSe micelles. In this way, we could tune the lattice constants of the PS-*b*-P4VP/CdSe/Au single-crystalline structure which could be applied in photonic crystal.

For the investigation on a memory device based on the nanostructured PS-*b*-P4VP thin film:

- Further analysis of the Al filament formation could be carried out by *a cross-section TEM image, a depth profile of SIMS, and a depth profile of XPS*.
- Further study on altering the electrode material to tune the memory behaviors of PS-*b*-P4VP. For example, using Cu instead of Al electrodes, the memory device might perform a lower writing voltage, a lower erasing voltage, a higher programming speed, and a high on-state current because of the higher diffusion rate and higher conductivity of Cu.

References

- [1] Bates, F. S.; Fredrickson, G. H. *Annu. Rev. Phys. Chem.* **1990**, *41*, 525.
- [2] Hamley, I. W. *The Physics of Block Copolymers* (Oxford: Oxford University Press) **1998**.
- [3] Hadjichristidis, N.; Pispas, S.; Floudas, G. *Block Copolymers. Synthetic Strategies, Physical Properties and Applications* (New York: Wiley), **2003**.
- [4] Fredrickson, G. H.; Bates, F. S. *Annu. Rev. Mater. Sci.* **1996**, *26*, 501.
- [5] Matsen, M. W. *J. Phys.: Condens. Matter* **2001**, *14*, R21.
- [6] Hamley, I. W. *J. Phys.: Condens. Matter* **2001**, *13*, R643.
- [7] Bates, F. S.; Fredrickson, G. H. *Phys. Today* **1999**, *52*, 32.
- [8] Drolet, F.; Fredrickson, G. H. *Phys. Rev. Lett.* **1999**, *83*, 4317.
- [9] Lazzari, M.; Lopez-Quintela, M. A. *Adv. Mater.* **2003**, *15*, 1583.
- [10] Matsen, M. W.; Schick, M. *Phys. Rev. Lett.* **1994**, *72*, 2660.
- [11] Matsen, M. W.; Bates, F. S. *Macromolecules* **1996**, *29*, 1091.
- [12] Hanley, K. J.; Lodge, T. P.; Huang, C. I. *Macromolecules* **2000**, *33*, 5918.
- [13] Russell, T. P. *Curr. Opin. Colloid Interface Sci.* **1996**, *1*, 107.
- [14] Helfand, E. *J. Chem. Phys.* **1975**, *62*, 999.
- [15] Shull, K. R. *Macromolecules* **1992**, *25*, 2122.
- [16] Matsen, M. W. *J. Chem. Phys.* **1997**, *106*, 7781.
- [17] Liu, K.; Baker, S. M.; Tuominen, M.; Russell, T. P.; Schuller, I. K. *Phys. Rev. B* **2001**, *63*, 060403(R).
- [18] Naito, K.; Hieda, H.; Sakurai, M.; Kamata, Y.; Asakawa, K. *IEEE Trans. Magn.* **2002**, *38*, 1949.
- [19] Park, M.; Harrison, C.; Chaikin, P. M.; Register, R. A.; Adamson, D. H. *Science* **1997**, *276*, 1401.
- [20] Harrison, C.; Park, M. P.; Chaikin, M.; Register, R. A.; Adamson, D. H. *J. Vac.*

Sci. Technol. B **1998**, *16*, 544.

- [21] Widawski, G.; Rawiso, M.; Francois, B. *Nature* **1994**, *369*, 387.
- [22] Matsen, M. W. *Curr. Opin. Colloid Interface Sci.* **1998**, *3*, 40.
- [23] Strawhecker, K. E.; Kumar, S. K.; Douglas, J. F.; Karim, A. *Macromolecules* **2001**, *34*, 4669.
- [24] Boker, A.; Mueller, A. H. E.; Krausch, G. *Macromolecules* **2001**, *34*, 7477.
- [25] Hamley, I. W.; Hiscutt, E. L., Yang, Y. W. Booth, C. J. *Colloid Interface Sci.* **1999**, *209*, 255.
- [26] Limary, R.; Green, P. F. *Langmuir* **1999**, *15*, 5617.
- [27] Muller-Buschbaum, P.; Gutmann, J. S.; Stamm, M. *Phys. Chem., Chem. Phys.* **1999**, *1*, 3857.
- [28] Ausserré, D.; Chatenay, D.; Coulon, G.; Collin, R. *J. Phys. France* **1990**, *51*, 2571.
- [29] Anastasiadis, S. H.; Russell, T. P.; Satija, S. K.; Majkrzak, C. F. *Phys. Rev. Lett.* **1989**, *62*, 1852.
- [30] Rehse, N.; Knoll, A.; Konrad, M.; Magerle, R.; Krausch, G. *Phys. Rev. Lett.* **2001**, *87*, 035505.
- [31] Thurn-Albrecht, T.; Schotter, J.; Kastle, G. A.; Emley, N.; Shibauchi, T.; Krusin-Elbaum, L.; Guarini, K.; Black, C. T.; Tuominen, M. T.; Russell, T. P. *Science* **2000**, *290*, 2126.
- [32] Park, C.; Yoon, J.; Thomas, E. L. *Polymer* **2003**, *44*, 6725.
- [33] Park, M.; Harrison, C.; Chaikin, P. M.; Register, R. A.; Adamson, D. H. *Science* **1997**, *276*, 1401.
- [34] Harrison, C.; Park, M.; Register, R. A.; Adamson, D.; Mansky, P.; Chaikin, P. M. *US Patent Specification* **1999**, 5948470.
- [35] Park, M.; Chaikin, P. M.; Register, R. A.; Adamson, D. H. *Appl. Phys. Lett.* **2001**,

79, 257.

- [36] Cheng, J. Y.; Ross, C. A.; Chan, V. Z. H.; Thomas, E. L.; Lammertink, R. G. H.; Vancso, G. J. *Adv. Mater.* **2001**, *13*, 1174.
- [37] Weng, C. C.; Wei, K. H. *Chem. Mater.* **2003**, *15*, 2936.
- [38] Yeh, S. W.; Wei, K. H.; Sun, Y. S.; Jeng, U. S.; Liang, K. S. *Macromolecules* **2003**, *36*, 7903.
- [39] Jeng, U. S.; Sun, Y. S.; Lee, H. Y.; Hsu, C. H.; Liang, K. S.; Yeh, S. W.; Wei, K. H. *Macromolecules* **2004**, *37*, 4617.
- [40] Yeh, S. W.; Chang, Y. T.; Chou, C. H.; Wei, K. H.; *Macromol. Rapid Commun.* **2004**, *25*, 1679.
- [41] Yeh, S. W.; Wu, T. L.; Wei, K. H.; Sun, Y. S.; Liang, K. S. *J. Polym. Sci. B Polym. Phys.* **2005**, *43*, 1220.
- [42] Yeh, S. W.; Wu, T. L.; Wei, K. H. *Nanotechnology* **2005**, *16*, 683.
- [43] Lin, Y.; Boker, A.; He, J.; Sill, K.; Xiang, H.; Abetz, C.; Li, X.; Wang, J.; Emrick, T.; Long, S.; Wang, Q.; Balazs, A.; Russell, T. P. *Nature* **2005**, *434*, 55.
- [44] Chiu, J. J.; Kim, B. J.; Kramer, E. J.; Pine, D. J. *J. Am. Chem. Soc.* **2005**, *127*, 5036.
- [45] Forster, S.; Antonietti, M. *Adv. Mater.* **1998**, *10*, 195.
- [46] Cohen, R. E. *Curr. Opin. Solid State Mater. Sci.* **1999**, *4*, 587.
- [47] Seregina, M. V.; Bronstein, L. M.; Platonova, O. A.; Chernyshov, D. M.; Valetsky, P. M.; Hartmann, J.; Wenz, E.; Antonietti, M. *Chem. Mater.* **1997**, *9*, 923.
- [48] Bronstein, L. M.; Sidorov, S. N.; Valetsky, P. M.; Hartmann, J.; Colfen, H.; Antonietti, M. *Langmuir* **1999**, *15*, 6256.
- [49] Antonietti, M.; Wenz, E.; Bronstein L.; Seregina, M. *Adv. Mater.* **1995**, *7*, 1000.
- [50] Platonova, O. A.; Bronstein, L. M.; Solodovnikov, S. P.; Yanovskaya, I. M.;

- Obolonkova, E. S.; Valetsky, P. M.; Wenz, E.; Antonietti, M. *Colloid Polym. Sci.* **1997**, *275*, 426.
- [51] Weng, C. C.; Hsu, K. F.; Wei, K. H. *Chem. Mater.* **2004**, *16*, 4080.
- [52] Maldovan, M.; Urbas, A. M.; Yufa, N.; Carter, W. C.; Thomas, E. L. *Phys. Rev. B* **2002**, *65*, 165123.
- [53] Alivisatos, A. P. *Endeavour* **1997**, *21*, 56.
- [54] El-Sayed, M. A. *Acc. Chem. Res.* **2004**, *37*, 326.
- [55] Naiwa, H. S. In *Hitachi Research Laboratory Handbook of Nanostructure Materials and Nanotechnology*, Vol. 4, Chapter 5, **2000**.
- [56] Wang, Y.; Herron, N. *J. Phys. Chem.* **1991**, *95*, 525.
- [57] Murray, C. B.; Norris, D. J.; Bawendi, M. G. *J. Am. Chem. Soc.* **1993**, *115*, 8706.
- [58] Alivisatos, A. P. *Science* **1996**, *271*, 933.
- [59] Brust, M. C.; Kiely, J. *Colloids Surf. A: Physicochem. Eng. Asp.* **2002**, *202*, 175.
- [60] Ouyang, J.; Chu, C. W.; Sieves, D.; Yang Y.; *Appl. Phys. Lett.* **2005**, *86*, 123507.
- [61] Simon, U. *Adv. Mater.* **1998**, *10*, 1487.
- [62] Sato, T.; Ahmed, H.; Brown, D.; Johnson, B. F. H. *J. Appl. Phys.* **1997**, *82*, 696.
- [63] Alivisatos, A. P.; Johnsson, K. P.; Peng, X.; Wilson, T. E.; Loweth, C. J.; Bruchez, M. P.; Schultz, P. G. *Nature* **1996**, *382*, 609.
- [64] Ueda, A.; Oshima, T.; Haruta, M. *Appl. Catal. B* **1997**, *12*, 81.
- [65] Bhat, R. R.; Genzer, J.; Chaney, B. N.; Sugg, H. W.; Liebmann-Vinson, A.; *Nanotechnology* **2003**, *14*, 1145.
- [66] Bockstaller, M. R.; Mickiewicz, R. A.; Thomas, E. L. *Adv. Mater.* **2005**, *17*, 1331.
- [67] Shenhar, R.; Norsten, T. B.; Rotello, V. M. *Adv. Mater.* **2005**, *17*, 657.
- [68] Haryono, A.; Binder, W. H. *Small* **2006**, *2*, 600.
- [69] (a) Alivisatos, A. P. *Nat. Biotechnol.* **2004**, *22*, 47. (b) Rosi, N. L.; Mirkin, C. A.; *Chem. Rev.* **2005**, *105*, 1547.

- [70] Huh, J.; Ginzburg, V. V.; Balazs, A. C. *Macromolecules* **2000**, *33*, 8085.
- [71] Thompson, R. B.; Ginzburg, V. V.; Matsen, M. W.; Balasz, A. C. *Science* **2001**, *292*, 2469.
- [72] Thompson, R. B.; Rasmussen, K. O.; Lookman, T. *Nano Lett.* **2004**, *4*, 2455.
- [73] Lee, J. Y.; Shou, Z.; Balasz, A. C. *Macromolecules* **2003**, *36*, 7730.
- [74] Schultz, A. J.; Hall, C. K.; Genzer, J. *Macromolecules* **2005**, *38*, 3007.
- [75] Mayer, A. B. R. *Polym. Adv. Technol.* **2001**, *12*, 96.
- [76] (a) Sohn, B. H.; Seo, B. H.; *Chem. Mater.* **2001**, *13*, 1752. (b) Sohn, B. H.; Seo, B. W.; Yoo, S. I. *J. Mater. Chem.* **2002**, *12*, 1730.
- [77] (a) Spatz, J. P.; Roescher, A.; Sheiko, S.; Krausch, G.; Moller, M. *Adv. Mater.* **1995**, *7*, 731. (b) Spatz, J. P.; Roescher, A.; Moller, M. *Adv. Mater.* **1996**, *8*, 337. (c) Mayer, A. B. R.; Mark, J. E. *Colloid Polym. Sci.* **1997**, *275*, 333.
- [78] Shen, H.; Zhang, L.; Eisenberg, A. *J. Am. Chem. Soc.* **1999**, *121*, 2728.
- [79] Hamdoun, B.; Ausserre, D.; Joly, S.; Gallot, Y.; Cabuil, V.; Clinard, C. *J. Phys. IV France* **1996**, *6*, 493.
- [80] Sohn, B. H.; Choi, J. M.; Yoo, S. I.; Yun, S. H.; Zin, W. C.; Jung, J. C.; Kanehara, M.; Hirata, T.; Teranishi, T. *J. Am. Chem. Soc.* **2003**, *125*, 6368.
- [81] Thurn-Albrecht, T.; Steiner, R.; DeRouchey, J.; Stafford, C. M.; Huang, E.; Bal, M.; Tuominen, M.; Hawker, C. J.; Russell, T. P. *Adv. Mater.* **2000**, *12*, 787.
- [82] Misner, M. J.; Skaff, H.; Emrick, T.; Russell, T. P. *Adv. Mater.* **2003**, *15*, 221.
- [83] Murray, C. B.; Kagan, C. R.; Bawendi, M. G. *Annu. Rev. Mater. Sci.* **2000**, *30*, 545.
- [84] Binder, W. H. *Angew. Chem.* **2005**, *117*, 5300; *Angew. Chem., Int. Ed.* **2005**, *44*, 5172.
- [85] (a) Colvin, V. L.; Goldstein, A. N.; Alivisatos, A. P. *J. Am. Chem. Soc.* **1992**, *114*, 5221. (b) Westenhoff, S.; Kotov, N. A. *J. Am. Chem. Soc.* **2002**, *124*, 2884.

- [86] (a) Maury, P.; Peter, M.; Mahalingam, V.; Reinhoudt, D. N.; Huskens, J. *Adv. Funct. Mater.* **2005**, *15*, 451. (b) Mahalingam, V.; Onclin, S.; Peter, M.; Ravoo, B. J.; Huskens, J. Reinhoudt, D. N. *Langmuir* **2004**, *20*, 11756. (c) Crespo-Biel, O.; Dordi, B.; Reinhoudt, D. N.; Huskens, J. *J. Am. Chem. Soc.* **2005**, *127*, 7594. (d) Auletta, T.; Dordi, B.; Mulder, A.; Sartori, A.; Onclin, S.; Bruinik, C. M.; Peter, M.; Nijhuis, C. A.; Beijleveld, H.; Schneherr, H.; Vansco, G. J.; Casnati, A.; Ungaro, R.; Ravoo, B.; Huskens, J.; Reinhoudt, D. N. *Angew. Chem.* **2004**, *116*, 373; *Angew. Chem., Int. Ed.* **2004**, *43*, 369.
- [87] (a) Boal, A. K.; Frankamp, B. L.; Uzun, O.; Tuominen, M. T.; Rotello, V. M.; *Chem. Mater.* **2004**, *16*, 3252. (b) Boal, A. K.; Ilhan, F.; DeRouchey, J. E.; Thurn-Albrecht, T.; Russell, T. P.; Rotello, V. M. *Nature* **2000**, *404*, 746. (c) Zirbs, R.; Kienberger, F.; Hinterdorfer, P.; Binder, W. H. *Langmuir* **2005**, *21*, 8414. (d) Coman, D.; Russu, I. M. *J. Am. Chem. Soc.* **2003**, *125*, 6626. (e) Peters, M.; Rozas, I.; Alkorta, I.; Elguero, J. *J. Phys. Chem. B* **2003**, *107*, 323. (f) Lin, H. C.; Sheu, H. Y.; Chang, C. L.; Tsai, C. *J. Mater. Chem.* **2001**, *11*, 2958.
- [88] (a) Kotov, N. A.; Dekany, I.; Fendler, J. H. *J. Phys. Chem.* **1995**, *99*, 13065 (b) Ariga, K.; Lvov, Y.; Onda, M.; Ichinose, I.; Kunitake, T. *Chem. Lett.* **1997**, *26*, 125. (c) Tang, Z.; Wang, Y.; Kotov, N. A. *Langmuir* **2002**, *18*, 7035.
- [89] Binder, W. H.; Kluger, C.; Straif, C. J.; Friedbacher, G. *Macromolecules* **2005**, *38*, 9405.
- [90] Yeh, S. W.; Wei, K. H.; Sun, Y. S.; Jeng, U. S.; Liang, K. S. *Macromolecules* **2005**, *38*, 6559.
- [91] Kim, B. J.; Chiu, J. J.; Yi, G. R.; Pine, D. J.; Kramer, E. J. *Adv. Mater.* **2005**, *17*, 2618.
- [92] Bockstaller, M. R.; Lapetnikov, Y.; Margel, S.; Thomas, E. L. *J. Am. Chem. Soc.* **2003**, *125*, 5276.

- [93] Bockstaller, M. R.; Thomas, E. L. *Phys. Rev. Lett.* **2004**, *93*, 166106.
- [94] Li, C. P.; Wu, C. H.; Wei, K. H.; Sheu, J. T.; Huang, J. Y.; Jeng, U. S.; Liang, K. S. *Adv. Funct. Mater.* **2007**, *17*, 2283.
- [95] Parthasarathy, R.; Lin, X. M.; Jaeger H. M. *Phys. Rev. Lett.* **2001**, *87*, 186807.
- [96] Fan, H.; Yang, K.; Boye, D. M.; Sigmon T.; Malloy, K. J.; Xu, H.; López, G. P.; Brinker, C. J. *Science* **2004**, *304*, 567.
- [97] Black, C. T.; Murray, C. B.; Sandstrom, R. L.; Sun, S. *Science* **2000**, *290*, 1131.
- [98] Beecher, P.; Quinn, A. J.; Shevchenko, E. V.; Weller, H.; Redmond, G. J. *Phys. Chem. B* **2004**, *108*, 9564.
- [99] Middleton, A. A.; Wingreen, N. S. *Phys. Rev. Lett.* **1993**, *71*, 3198.
- [100] Leong, W. L.; Lee, P. S.; Lohani, A.; Lam, Y. M.; Chen, T.; Zhang, S.; Dodabalapur, A.; Mhaisalkar, S. G. *Adv. Mater.* **2008**, *20*, 2325.
- [101] Friend, R. H.; Gymer, R. W.; Holmes, A. B.; Burroughes, J. H.; Marks, R. N.; Taliani, C.; Bradley, D. D. C.; Dos Santos, D. A.; Brédas, J. L.; Lögdlund, M.; Salaneck, W. R. *Nature* **1999**, *397*, 121.
- [102] Howard, W. E. *Sci. Am.* **2004**, *290*, 76.
- [103] (a) Sirringhuas, H.; Tessler, N.; Friend, R. H. *Science* **1998**, *280*, 1741.
(b) Dimitrakopoulos, C. D.; Mascaro, D. J. *IBM J. Res. Dev.* **2001**, *45*, 11.
- [104] (a) Yu, G.; Gao, J.; Hummelen, J. C.; Wudl, F.; Heeger, A. J. *Science* **1995**, *270*, 1789. (b) Brabec, C. J.; Sariciftci, N. S.; Hummelen, J. C. *Adv. Funct. Mater.* **2001**, *11*, 15.
- [105] (a) Nakayama, K.; Kojima, K.; Imai, Y.; Kasai, T.; Fukushima, S.; Kitagawa, A.; Kumeda, M.; Kakimoto, Y.; Suzuki, M. *Jpn. J. Appl. Phys., Part 1* **2003**, *42*, 404. (b) Dewald, J. F.; Pearson, A. D.; Northover, W. R.; Peck, J. J. *Electrochem. Soc.* **1962**, *109*, 243c. (c) Hovel, H. J.; Urgell, J. J. *J. Appl. Phys.* **1971**, *42*, 5076.

- [106] (a) Mitkova, M.; Kozicki, M. N. *J. Non-Cryst. Solids* **2002**, 299–302, 1023. (b) Kozicki, M. N.; West, W. C. *US Patent 5 761 115*, **1998**.
- [107] (a) Rueckes, T.; Kim, K.; Joselevich, E.; Tseng, G. Y.; Cheung, C. L.; Lieber, C. M. *Science* **2000**, 289, 94. (b) Badzey, R. L.; Zolfagharkhani, G.; Gaidarzhy, A.; Mohanty, P. *Appl. Phys. Lett.* **2005**, 86, 23 106.
- [108] Terabe, K.; Hasegawa, T.; Nakayama, T.; Aono, M. *Nature* **2005**, 433, 47.
- [109] (a) Kouklin, N.; Bandyopadhyay, S.; Tereshin, S.; Varfolomeev, A.; Zaretsky, D. *Appl. Phys. Lett.* **2000**, 76, 460. (b) Ohab, R.; Sugiyama, N.; Uchida, K.; Koga, J.; Toriumi, A. *IEEE Trans. Electron Devices* **2002**, 49, 1392.
- [110] (a) Guarini, K. W.; Black, C. T.; Zhang, Y.; Babich, I. V.; Sikorski, E. M.; Gignac, L. M. *IEEE Int. Electron Device Meet., Tech. Dig.* **2003**, 541. (b) Ostraat, M. L.; De Blauwe, J. W.; Green, M. L.; Bell, L. D.; Brongerma, M. L.; Casperson, J. R.; Flagan, C.; Atwater, H. A. *Appl. Phys. Lett.* **2001**, 79, 433.
- [111] (a) Scott, J. C. *Science* **2004**, 304, 62. (b) Kwok, K. S.; Ellenbogen, J. C. *Mater. Today* **2002**, 5, 28.
- [112] (a) Okamoto, K.; Araki, Y.; Ito, O.; Fukuzumi, S. *J. Am. Chem. Soc.* **2004**, 126, 56. (b) Ipe, B. I.; Thomas, K. G.; Barazzouk, S.; Hotchandani, S.; Kamat, P. V. *J. Phys. Chem. B* **2002**, 106, 18.
- [113] Peng, H.; Ran, C.; Yu, X.; Zhang, R.; Liu, Z. *Adv. Mater.* **2005**, 17, 459.
- [114] Ma, L. P.; Liu, J.; Pyo, S.; Yang, Y. *Appl. Phys. Lett.* **2002**, 80, 362.
- [115] Lai, Y. S.; Tu, C. H.; Kwong, D. L.; Chen, J. S. *Appl. Phys. Lett.* **2005**, 87, 122101.
- [116] Ma, L. P.; Pro, S. M.; Ouyang, J.; Xu, Q.; Yang, Y. *Appl. Phys. Lett.* **2003**, 82, 1419.
- [117] Chen, C. C.; Chiu, M. Y.; Sheu, J. T.; Wei, K. H. *Appl. Phys. Lett.* **2008**, 92, 143105.

- [118] Pender, L. F.; Fleming, R. J. *J. Appl. Phys.* **1975**, *46*, 3426.
- [119] Ma, L.; Xu, Q.; Yang, Y. *Appl. Phys. Lett.* **2004**, *84*, 4908.
- [120] Ling, Q. D.; Song, Y.; Ding, S. J.; Zhu, C. X.; Chan, D. S. H.; Kwong, D. L.; Kang, E. T.; Neoh, K. G. *Adv. Mater.* **2005**, *17*, 455.
- [121] Bandyopadhyay, A.; Pal, A. J. *Appl. Phys. Lett.* **2003**, *82*, 1215.
- [122] Balazs, A. C.; Emrick, T.; Russell, T. P. *Science* **2006**, *314*, 1107.
- [123] Fink, Y.; Urbas, A. M.; Bawendi, M. G.; Joannopoulos, J. D.; Thomas, E. L. *J. Lightwave Technol.* **1999**, *17*, 1963.
- [124] Lopes, W. A.; Jaeger, H. M. *Nature(London)* **2001**, *414*, 735.
- [125] Li, C. P.; Wei, K. H.; Huang, J. Y. *Angew. Chem., Int. Ed.* **2006**, *45*, 1449.
- [126] Tsutsumi, K.; Funaki, Y.; Funaki, Y.; Hirokawa, Y.; Hashimoto, T. *Langmuir* **1999**, *15*, 5200.
- [127] Sohn, B. H.; Seo, B. H.; Seo, B. W.; Yun, S. H.; Park, S. M. *J. Am. Chem. Soc.* **2001**, *123*, 12734.
- [128] Zhang, Q.; Xu, T.; Butterfield, D.; Misner, M. J.; Ryu, D. Y.; Emrick, T.; Russell, T. P. *Nano Lett.* **2005**, *5*, 357.
- [129] Buxton, G. A.; Lee, J. Y.; Balazs, A. C. *Macromolecules* **2003**, *36*, 9631.
- [130] Lee, J. Y.; Thompson, R. B.; Jasnow, D.; Balazs, A. C. *Macromolecules* **2002**, *35*, 4855.
- [131] Thompson, R. B.; Ginzburg, V. V.; Matsen, M. W.; Balazs, A. C. *Macromolecules* **2002**, *35*, 1060.
- [132] Lee, J. Y.; Thompson, R. B.; Jasnow, D.; Balazs, A. C. *Phys. Rev. Lett.* **2002**, *89*, 155503.
- [133] Kim, J. U.; O'Shaughnessy, B. *Phys. Rev. Lett.* **2002**, *89*, 238301.
- [134] Sides, S. W.; Kim, B. J.; Kramer, E. J.; Fredrickson, G. H. *Phys. Rev. Lett.* **2006**, *96*, 250601.

- [135] Kim, B. J.; Bang, J.; Hawker, C. J.; Kramer, E. J. *Macromolecules* **2006**, *39*, 4108.
- [136] Zubarev, E. R.; Xu, J.; Sayyad, A.; Gibson, J. D. *J. Am. Chem. Soc.* **2006**, *128*, 15098.
- [137] Spontak, R. J.; Shankar, R.; Bowman, M. K.; Krishnan, A. S.; Hamersky, M. W.; Samseth, J.; Bockstaller, M. R.; Rasmussen, K. Ø. *Nano Lett.* **2006**, *6*, 2115.
- [138] Listak, J.; Bockstaller, M. R. *Macromolecules* **2006**, *39*, 5820.
- [139] Brust, M.; Walker, M.; Bethell, D.; Schiffrin, D. J.; Whyman, R. *J. Chem. Soc., Chem. Commun.* **1994**, 801.
- [140] Donkers, R. L.; Lee, D.; Murray, W. R. *Langmuir* **2004**, *20*, 1945.
- [141] Lai, Y. H.; Sun, Y. S.; Jeng, U. S.; Lin, J. M.; Lin, T. L.; Sheu, H. S.; Chuang, W. T.; Huang, Y. S.; Hsu, C. H.; Lee, M. T.; Lee, H. Y.; Liang, K. S.; Gabriel, A.; Koch, M. H. J. *J. Appl. Crystallogr.* **2006**, *39*, 871.
- [142] Sun, Y. S.; Jeng, U. S.; Liang, K. S.; Yeh, S. W.; Wei, K. H. *Polymer* **2006**, *47*, 1101.
- [143] Pieranski, P. *Phys. Rev. Lett.* **1980**, *45*, 569.
- [144] Kunz, M. S.; Shull, K. R.; Kellock, A. J. *J. Colloid Interface Sci.* **1993**, *156*, 240.
- [145] Lin, Y.; Skaff, H.; Emrick, T.; Dinsmore, A. D.; Russell, T. P. *Science* **2003**, *299*, 226.
- [146] Lin, Y.; Skaff, H.; Böker, A.; Dinsmore, A. D.; Emrick, T.; Russell, T. P. *J. Am. Chem. Soc.* **2003**, *125*, 12690.
- [147] Chen, J. T.; Thomas, E. L.; Ober, C. K.; Mao, G. P.; *Science* **1996**, *273*, 343.
- [148] Morkved, T. L.; Lu, M.; Urbas, A. M.; Ehrichs, E. E.; Jaeger, H. M.; Mansky, P.; Russell, T. P. *Science* **1996**, *52*, 931.
- [149] Huang, C. M.; Wei, K. H.; Jeng, U. S.; Liang, K. S. *Macromolecules* **2007**, *40*,

5067.

- [150] Park, S. C.; Kim, B. J.; Hawker, C. J.; Kramer, E. J.; Bang, J.; Ha, J. S. *Macromolecules* **2007**, *40*, 8119.
- [151] Lo, C. T.; Lee, B.; Winans, R. E.; Thiyagarajan, P. *Macromolecules* **2007**, *40*, 641.
- [152] Lee, B.; Lo, C. T.; Seifert, S.; Rago Dietz, N. L.; Winans, R. E.; Thiyagarajan, P. *Macromolecules* **2007**, *40*, 4235.
- [153] Tenneti, K. K.; Chen, X.; Li, C. Y.; Tu, Y.; Wan, X.; Zhou, Q. F.; Sics, I.; Hsiao, B. S. *J. Am. Chem. Soc.* **2005**, *127*, 15481.
- [154] Chen, H. L.; Lu, J. S.; Yu, C. H.; Yeh, C. H.; Jeng, U. S.; Chen, W. C. *Macromolecules* **2007**, *40*, 3271.
- [155] Rietveld, H. M. *J. Appl. Cryst.* **1969**, *2*, 65.
- [156] Black, C. T.; Guarini, K. W.; Milkove, K. R.; Baker, S. M.; Russell, T. P.; Tuominen, M. T. *Appl. Phys. Lett.* **2001**, *79*, 409.
- [157] Tu, C. H., Lai, Y. S. Kwong, D. L. *IEEE Electron Device Lett.* **2006**, *27*, 354.
- [158] Kasap, S. O. *Principles of Electronic Materials and Devices* **2002**, McGraw-Hill, New York.
- [159] West, R. C. *CRC Handbook of Chemistry and Physics, 65th edition.* **1983**, CRC Press, Boca Raton.
- [160] Joo, W. J.; Choi, T. L.; Lee, J.; Lee, S. K.; Jung, M. S.; Kim, N.; Kim, J. M. *J. Phys. Chem. B* **2006**, *110*, 23812.
- [161] Krenek, R.; Stamm, M.; Cimrova, V. *J. Appl. Phys.* **2008**, *103*, 16.

Appendix 1

Quantitative calculations of Au NPs at the surface of a single P4VP domain.

SAXS analysis revealed that the average diameter of the P4VP cores (R_{P4VP}) was 18 nm and that of the AuSC₂Ph NPs (R_{Au}) was 2.2 nm. In general, the densities of P4VP and Au before and after mixing were assumed to remain constant. Because the known volume ratio of P4VP to Au (ranging from 11.7 to 1.4%) in PS-*b*-P4VP_{Sph}/AuSC₂Ph mixture was equal to that of a P4VP core to an unknown quantity of Au NPs [$\frac{4}{3}\pi(\frac{R_{P4VP}}{2})^3$ to $n_{Au} \times \frac{4}{3}\pi(\frac{R_{Au}}{2})^3$] in a single P4VP/Au core/shell structure, the number of Au NPs ($n_{Au} = \text{ca. } 66$) was estimated using equation (A-1):

$$\frac{V_{P4VP}}{V_{Au}} = \frac{R_{P4VP}^3}{n_{Au} \times R_{Au}^3} \quad (\text{A-1-1})$$

Subsequently, to calculate the percentage coverage of the Au NPs, we assumed that a Au NP could contribute a covered area equal to its maximum cross-sectional area (a great-circle area) of $\pi(\frac{R_{Au}}{2})^2$ and that the total P4VP surface area was $4\pi(\frac{R_{P4VP}}{2})^2$.

Thus, we obtained a percentage covered of 24.7% when using equation (A-2):

$$\text{Covered area percentage} = \frac{n_{Au}}{4} \left(\frac{R_{Au}}{R_{P4VP}}\right)^2 \times 100\% \quad (\text{A-1-2})$$

To simplify the calculation, we ignore the fact that the P4VP surface area covered by an Au NP is cambered. In fact, an Au NP can cover more than $\pi(\frac{R_{Au}}{2})^2$, except when $R_{P4VP} \gg R_{Au}$.

Appendix 2

Distance between the CdSe particles in a single P4VP domain.

We determined the average center-to-center and edge-to-edge interparticle distances between the CdSe NPs based on the feed of the CdSe loading (*J. Am. Chem. Soc.* **2000**, *122*, 11465). The free volume per CdSe NP (V_{free}) in the P4VP domain, which is defined by the average volume of an occupied CdSe NP, can be estimated using Eqs. (A-2-1) and (A-2-2):

$$\frac{V_{\text{CdSe/P4VP}} - V_{\text{P4VP}}}{V_{\text{CdSe}}} = n \quad (\text{A-2-1})$$

$$\frac{V_{\text{CdSe/P4VP}}}{n} = V_{\text{free}} \quad (\text{A-2-2})$$

where $V_{\text{CdSe/P4VP}}$ is the volume of a single CdSe NPs/P4VP composite domain, V_{P4VP} is the volume of the P4VP domain, V_{CdSe} (22.45 nm^3) is the volume of a CdSe NP (3.5 nm in diameter), and n is the number of CdSe NPs in the P4VP domain. The center-to-center interparticle distance (D) was calculated using Eq. (A-2-3).

$$D = (V_{\text{free}})^{1/3} \quad (\text{A-2-3})$$

The edge-to-edge interparticle distance (d) was determined by assuming a cubic lattice model for the CdSe NPs. The values of d were calculated using Eq. (A-2-4):

$$d = D - 2r = (V_{\text{free}})^{1/3} - 2r \quad (\text{A-2-4})$$

where r is the radius of the CdSe NPs.

Publication List

Chung-Ping Li, **Ching-Mao Huang**, Meng-Ting Hsieh and Kung-Hwa Wei, “Properties of Covalently Bonded Layered-Silicate/Polystyrene Nanocomposites Synthesized via Atom Transfer Radical Polymerization”, *J. Polym. Sci. Part A: Polym. Chem.* **2005**, *43*, 534. (Impact Factor 3.529)

Ching-Mao Huang, Kung-Hwa Wei, U-Ser Jeng, and Keng-S. Liang, “Structural Evolution of Poly(styrene-*b*-4-vinylpyridine) Diblock Copolymer/Gold Nanoparticle Mixtures from Solution to Solid State”, *Macromolecules* **2007**, *40*, 5067. (Impact Factor 4.411)

Ching-Mao Huang, Kung-Hwa Wei, U-Ser Jeng, and Hwo-Shuenn Sheu, “Pseudo-Single-Crystalline Self-Assembled Structure Formed from Hydrophilic CdSe and Hydrophobic Au Nanoparticles in the Polystyrene and Poly(4-vinylpyridine) Blocks, Respectively, of a Polystyrene-*b*-Poly(4-vinylpyridine) Diblock Copolymer”, *Macromolecules* **2008**, *41*, 6876. (Impact Factor 4.411)

Ching-Mao Huang, Yung-Sheng Liu, Chen-Chia Chen, Kung-Hwa Wei, and Jeng-Tzong Sheu, “Electrical Bistable Memory Device Based on a Poly(styrene-*b*-4-vinylpyridine) Nanostructured Diblock Copolymer Thin Film”, *Appl. Phys. Lett.* **2008**, *93*, 203303. (Impact Factor 3.596)

學經歷資料

- 姓名：黃清茂
- 性別：男
- 生日：68 年 4 月 3 日
- 電子郵件信箱：chingmao.mse92@nctu.edu.tw
- 聯絡電話：(學校) 03-5731771 (手機) 0958-671025
- 通訊地址：新竹市 300 大學路 1001 號
國立交通大學材料與工程研究所
- 永久地址：台北縣金山鄉清泉村清水路 4 鄰 60 巷 18 號



學歷

博士候選人：國立交通大學材料科學與工程研究所	2003. 9 ~ 2008. 12
碩士：國立交通大學材料科學與工程學研究所	2001. 9 ~ 2003. 7
學士：國立交通大學材料科學與工程學學系	1997. 9 ~ 2001. 7

參與計畫

- 非揮發記憶體用之高分子/核殼奈米顆粒奈米複合材料之合成與元件製備 (2007.1~present)
- 高效率光電轉換自身組織功能性奈米結構材料與元件之前瞻研究。(2005. 8 ~ 2006. 6)
- 量子點/自身組織塊式高分子奈米複合材料。(2002. 1 ~ 2005. 12)
- 聚氨基甲酸酯(PU)/黏土(Clay)奈米複合材料之開發研究。(2004. 1~2005. 12)
- 原位合成 PS/黏土奈米複合材料之開發研究(國科會)。(2004. 9~2005. 9)

專長

- 奈米操控技術：
無機奈米結構(nanostructure)之合成、鑑定分析與其界面改質分散技術。藉以達到奈米材料操控與分散的目的。
- 有機/無機奈米複合材料：
 1. 原位聚合聚苯乙烯(PS)/矽酸鹽層奈米複合材料。
 2. 構裝用低介電聚亞醯(PI)/矽酸鹽層奈米複合材料。
 3. PU 發泡用聚酯多元醇(Polyester)/矽酸鹽層奈米複合材料。
 4. 雙塊式共聚高分子/奈米粒子複合材料製備與型態分析。
- 分析儀器操作：
穿透式電子顯微鏡、X 光繞射、小角 X 光散射、超薄切片機、PL、FT-IR、UV-visible 光譜、熱分析(DSC, TGA, TMA)、粒徑分析。
- 專利：
聚酯多元醇/矽酸鹽層奈米複合材料製法，黃清茂、韋光華、石昆吟，2006.